APPLIED COMPUTATIONAL ELECTROMAGNETICS SOCIETY JOURNAL

November 2022
Vol. 37 No. 11
ISSN 1054-4887

The ACES Journal is abstracted in INSPEC, in Engineering Index, DTIC, Science Citation Index Expanded, the Research Alert, and to Current Contents/Engineering, Computing & Technology.

The illustrations on the front cover have been obtained from the ARC research group at the Department of Electrical Engineering, Colorado School of Mines

Published, sold and distributed by: River Publishers, Alsbjergvej 10, 9260 Gistrup, Denmark

NOVEMBER 2022 REVIEWERS

Agarwal
Rezaul Azim
Thomas Bauernfeind
Yogesh Kumar Coukiker
Zaheer Ahmed Dayo
Nasr H. Gad
Zi He
Bernhard J. Hoenders
Guan-Long Huang
Taha Imeci
Ahmed Jamal
Pankaj Jha
Anubhav Kumar
Bai Lei
Matteo Bruno Lodi
Valentin Mateev
Anveshkumar Nella
Mahdi Oliaei
Andrew Peterson
C. J. Reddy
Suganthi Santhanam
Steven Weiss
Gaobiao Xiao
Wentao Yuan
Qiwei Zhan

THE APPLIED COMPUTATIONAL ELECTROMAGNETICS SOCIETY JOURNAL

Vol. 37 No. 11 November 2022

TABLE OF CONTENTS

A Low-Profile Wideband Circularly Polarized Metasurface Antenna Based on Characteristic Mode Theory

Shuangbing Liu[1,2], Lixia Yang[2], and Xianliang Wu[2]

[1]School of Electronic Engineering
Chaohu University, Hefei 238024, China

[2]School of Electronic Information Engineering
Anhui University, Hefei 230601, China
liushb@chu.edu.cn, lixiayang@yeah.net, xlwu@ahu.edu.cn

Abstract **–** A novel low-profile wideband circularly polarized metasurface (MTS) antenna is proposed. The characteristic mode analysis is used to investigate the operating mechanism of the MTS antenna. Then, the desired modes are chosen and excited by the annular ring slot combined with an L-shaped microstrip line. Simulation studies revealed that this type of feeding structure effectively excites the desired modes to accomplish wideband circular polarization and high-gain radiation. Experimental results show that the antenna has both the wide impedance bandwidth (IBW) and axial ratio bandwidth (ARBW), with a maximum radiation gain of 9.3 dBi and a −10 dB relative IBW and 3 dB relative ARBW of 39.8% and 30%, respectively.

Index Terms **–** characteristic mode analysis, circularly polarized slot antenna, metasurface, low-profile, wideband.

I. INTRODUCTION

Due to its advantages of generating and receiving at arbitrary polarization angles and anti-multipath interference, circularly polarized antennas are employed in wireless systems. Printed antennas are receiving considerable attention because of their compact size, low profile, simple design, uncomplicated design and fabrication, and low production cost [1]. However, these types of antennae suffer from narrow impedance bandwidth (IBW) and axial ratio bandwidth (ARBW). For example, Li et al. proposed a microstrip-fed slot antenna that stimulates circularly polarized radiation by loading capacitive or inductive loads in the annular slot, with 3 dB ARBWs of 5.5 percent and 6.7 %, respectively and radiation gain of 3 dBic [2]. The U-slot carved on the metal patch in the annular slot was used to obtain circular polarization in the annular-slot antenna [3]. The ARBW was 5.15% and the peak gain was 7.6 dBic. For L-shaped microstrip, a series feed approach was considered. Row developed a circularly polarized square ring slot antenna that was fed in series by an L-shaped microstrip and has shown a 3 dB ARBW of roughly 6% and a maximum radiation gain of 3.3 dBic [4]. A circularly polarized antenna with an ARBW of 8.9% and a maximum radiation gain of 6.5 dBic has been proposed in [5], which was fed by an annular ring slot with an L-shaped microstrip line.

Recently, metasurface (MTS) has been widely used in high-performance antennas, polarization modulation, and other applications. MTSs act as a reflector [6], polarization converters [7], or radiators [8–12]. The 3dB ARBW of the antenna increased to 23.4%, and the radiation gain of 7.0-7.6 dBic has been reported [8]. Cao et al. have developed a circularly polarized MTS antenna that was fed by an L-shaped slot and showed a 23.6% ARBW and a 7.3-8.1 dBic radiation gain [9]. Liu et al. reported a square array MTS antenna with four crossed slots for feeding [10]. The antenna showed a 14.5% ARBW and a 7 dBic radiation gain. In these antennas the MTS covers the dielectric layer of the feeding slot, resulting in a low profile and wide circularly polarized bandwidth, but insufficient radiation gain. An air layer [13] or a foam substrate [14] has been added between the MTS and the feeding structure of some antennas to improve the radiation gain. But this strategy has increased the antenna's profile as well as structural complexity.

II. STRUCTURE OF THE PROPOSED ANTENNA

The antenna structure and geometrical dimensions are shown in Fig. 1 and Table 1. The designed antenna consists of two layers of dielectric substrates. The relative dielectric constant of the upper layer is 3.5, with a thickness of h_2 = 2 mm. The MTS is formed by printing 5 × 5 square metal patch arrays on its upper surface, as shown in Fig. 1 (a). Each metal patch has dimensions of $p \times p$. The edge-to-edge width of the patches is g. The lower substrate has a relative dielectric constant of 4.4, with a thickness of h_1 = 0.8 mm, whose upper surface is a metal ground contact etched with an annular slot as

Submitted On: June 1, 2022
Accepted On: December 27, 2022

https://doi.org/10.13052/2022.ACES.J.371101

shown in Fig. 1 (b). The inner radius r_1 and outer radius r_2 of the annular ring slot are initially calculated by:

$$f \approx \frac{c}{\pi(r_1+r_2)\sqrt{\varepsilon_{eff}}}, \quad (1)$$

where f is the designed center operating frequency, c is the speed of light in free space and ε_{eff} is the effective relative permittivity considering the presence of different dielectric media on the two sides of the ring slot. A 50 Ω L-shaped microstrip feedline (width w_1) with a quarter-wavelength impedance transformer is designed on the bottom surface of the lower substrate as shown in Fig. 1 (c). The impedance transformer is a microstrip-line section of length l_2 and width w_2, which transforms the impedance seen at the outer slot boundary to the 50 Ω microstrip feedline.

To accomplish the low-profile characteristic, the ground contact is directly made with the two layers of dielectric substrates from the side as shown in Fig. 1 (d). Through the annular slot, the L-shaped microstrip feeder is couple-fed to the MTS in both x and y directions, with a phase difference of 90° between the two positions to produce circularly polarized radiation.

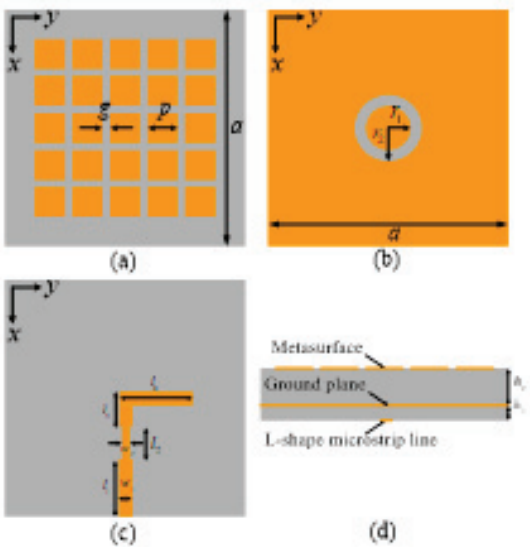

Fig. 1. Schematic diagram of the antenna structure. (a) MTS of 5 × 5 square patch arrays. (b) Ground contact with the annular slot. (c) L-shaped microstrip feed structure. (d) Side view of the antenna.

Table 1: Relevant parameters of wideband circularly polarized MTS antenna

Parameters	a	g	p	r_1	r_2	l_1
Unit (mm)	50	0.5	7.3	3.3	5.3	12.9
Parameters	l_2	l_3	l_4	w_1	w_2	
Unit (mm)	6.8	6.05	9.29	1.5	0.5	

III. WORKING MECHANISM OF CIRCULAR POLARIZATION

A. Characteristic mode analysis of the MTS

In recent years, characteristic mode analysis has been widely used in antenna design [16–19], which provides insight into the physical understanding of the antenna. The resonant frequency and potential contribution to the radiation of a mode are measured by the modal significance:

$$MS = \left| \frac{1}{1+j\lambda_n} \right|, \quad (2)$$

where λ_n are the eigenvalues. The range of MS is 0 to 1. If MS $\geq$ 0.707, the associated modes are significant. Otherwise, the associated modes are non-significant. When MS = 1, the mode resonates and radiates the most efficiently.

The modal properties of the MTS are explored to understand the functioning mechanism of circular polarization. The MTS with an infinite substrate and ground plate is simulated based on characteristic mode analysis. The MS of the four significant characteristic modes of the MTS is shown in Fig. 2. As can be seen, J_1 and J_2 are a pair of modes resonating at the same frequency of 7.2 GHz with the same MS. J_3 and J_4 exhibited the same resonant frequency, as well as a similar trend with frequency.

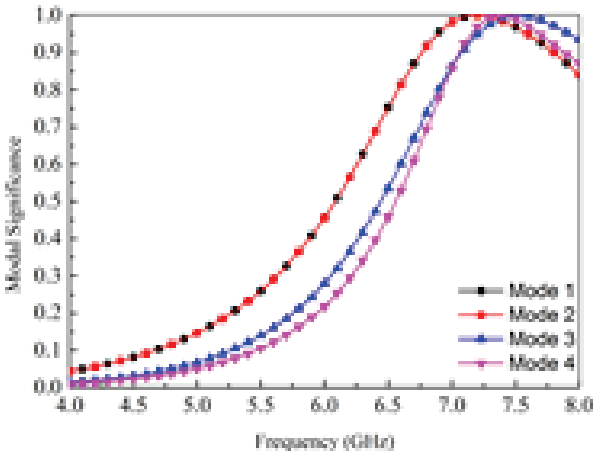

Fig. 2. MS of the four significant modes of the MTS.

Figure 3 shows the mode currents for the four modes at 7.2 GHz, with black arrows indicating the current direction. J_1 is in phase over the entire MTS and polarized in the y-direction. J_2 is identical to J_1, yet the polarization direction was rotated by 90° over the MTS plane. As a result of the symmetry of the MTS, J_1 and J_2 are a pair of orthogonal modes. As all of the currents are in phase, they both generate broadside radiation patterns, as shown in Figs. 4 (a) and (b). J_3 and J_4 were

self-symmetric in both the x and y directions. Due to the out-of-phase of the currents, a radiation null appears in the boresight, as shown in Figs. 4 (c) and (d). The modal radiation patterns are consistent with the results of modal current distributions. It can be concluded that J_1 and J_2 are the ideal unidirectional radiation modes, exciting either of which will form a linearly polarized antenna. Due to the orthogonality of the two modes themselves, the circularly polarized antenna will be formed in the scenario of simultaneous excitation of the two modes with a phase difference of 90°.

To acquire a circularly polarized broadside radiation pattern, the appropriate modes should be excited. Therefore, J_1 and J_2 are selected to generate the desired radiation pattern, while J_3 and J_4 are the unwanted modes.

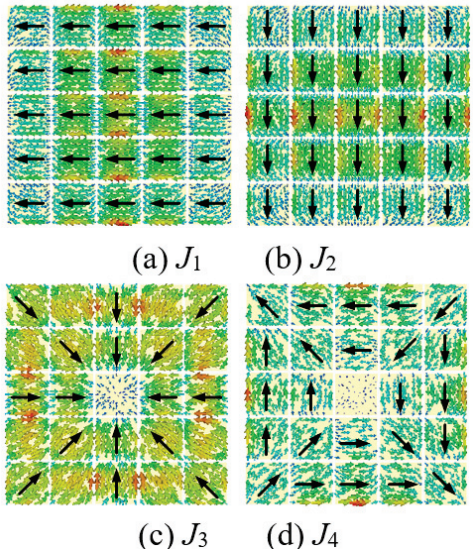

Fig. 3. Current distributions of the four characteristic modes at 7.2 GHz.

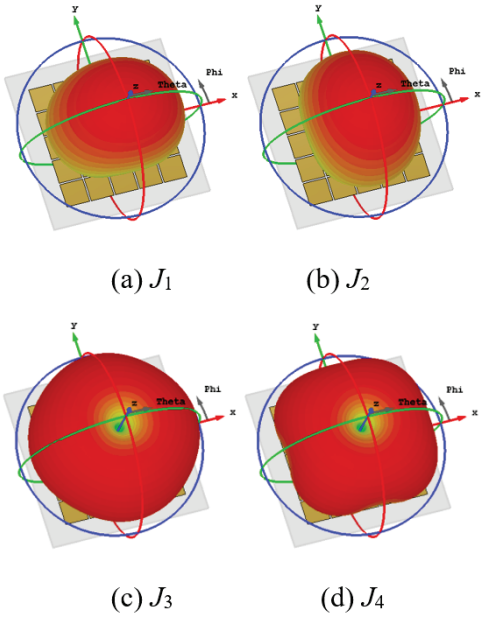

Fig. 4. Radiation patterns of the four characteristic modes at 7.2 GHz.

B. Antenna feed network

The feeding structure is critical to exciting the desired mode. As shown in Fig. 3, it is easy to find that the maximum current distribution of J_1 and J_2 is at the center of the MTS, where the modes can be excited efficiently. But, the minimum current distribution of J_3 and J_4 is at the center of the MTS. The feeding structure should be positioned directly beneath the MTS's center patch. Furthermore, it is clear from Fig. 3 that the current densities of J_1 and J_2 on the middle patch are mostly dispersed near the patch's edge. Hence, the magnetic current coupled by feeding the annular-ring slot should be located where the maximum magnetic field of the desired mode J_1 and J_2 presents for maximum efficient coupling. In this way, the desired modes J_1 and J_2 can be most effectively excited by the feeding slot while the unwanted mode J_3 and J_4 will be suppressed. To obtain circularly polarized radiation, the feeding network has to excite both J_1 and J_2 at the same time and establish a 90° phase difference. Therefore, a single-feed network combining an annular-ring slot and an L-shaped microstrip line is adopted to excite the antenna, as shown in Figs. 1 (b) and (c).

Following this, simulations are performed on surface current distributions on the MTS at various phase excitations to explore the feed network's operating mechanism in greater depth. Figure 5 shows the surface current distributions on the MTS at two minimum frequencies of the antenna axial ratio (5.4 GHz and 6.7 GHz). The surface current is found to flow in the -x direction at 5.4 GHz with a phase angle of 0° and in the +y direction at a phase angle of 90°, as shown in Fig. 5 (a). As shown in Fig. 5 (b), the surface current is found to flow mainly in the +x direction at a frequency of 6.7 GHz and a phase angle of 0°, and in the –y direction at a phase angle of 90°. The results indicate that at each minimum of axial ratio, two orthogonal modes with a phase difference of 90° were excited, resulting in the acquisition of left-hand circularly polarized (LHCP) radiation in the broadside direction. Surprisingly, the distribution of surface currents flowing down the x-axis on the MTS's center patch is almost equal to that of J_2's characteristic mode current or is in an anti-phase state. Similarly, the distribution of surface currents flowing along the y-direction is nearly identical to that of the characteristic mode current or is in its anti-phase state. Maximum currents are predominantly centered on a few

patches at the center of the MTS at 5.4 GHz, but they are essentially spread over all patches over the MTS at 6.7 GHz, which may be found in the comparison of Figs. 5 (a) and (b). In other words, the axial ratio minimum at 5.4 GHz mainly resulted from the annular slot of the L-shaped microstrip feed, while that at 6.7 GHz is mainly attributed to the MTS.

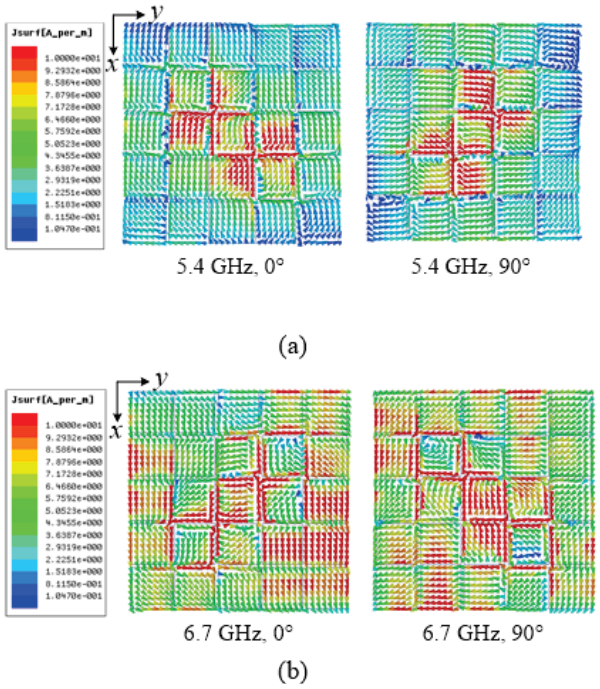

Fig. 5. Surface current distribution on the MTS at different excitation phases.

IV. PARAMETRIC STUDY

The parametric study is conducted to investigate the effects of key MTS parameters on the impedance bandwidth and ARBW of the broadband circularly polarized MTS antenna. The key parameters include the length of the square patch and the number of cells.

A. Effect of the length of the square patch (*p*)

Figure 6 shows the S_{11} and AR values of the circularly polarized MTS antenna for different lengths of the square patch. As shown in Fig. 6 (a), the variation in the length of the square patch has little effect on the reflection coefficient of the antenna. As the length increases, the impedance matching at the high frequencies deteriorates. It may be caused by the decrease of the resonant frequency of the characteristic modes J_1 and J_2 due to the increase of the length p. As shown in Fig. 6 (b), all lengths of the square patch yield two minimum points in their AR profiles. The frequencies of the two AR minimum points decrease with the increase of the length. AR is greater than 3 dB between 5.6–6.1 GHz for p = 8.1 mm. The optimal ARBW is obtained for p = 7.8 mm.

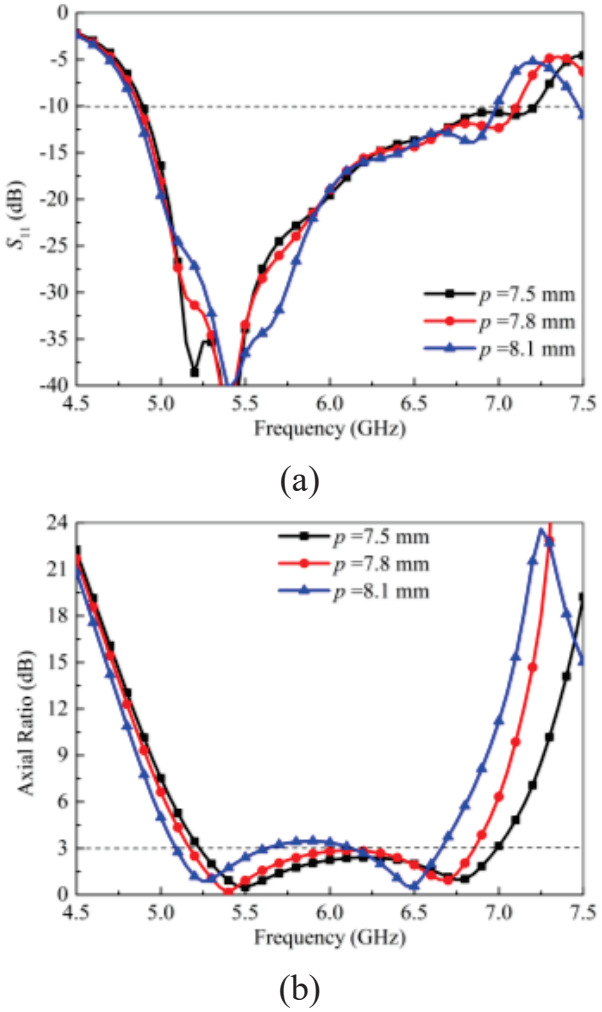

Fig. 6. Simulated (a) S_{11} and (b) AR values for different lengths of square patch.

B. Effect of the number of the cells

The S_{11} and AR values of the proposed MTS antenna are calculated for different cells of the MTS, including 3 × 3, 4 × 4, 5 × 5, and 6 × 6 cells, and are presented in Fig. 7. As shown in Fig. 7 (a), all configurations of the MTS antenna yield more than two resonant frequencies in their S_{11} profiles. Besides that, the number of MTS array elements has little influence on the IBW of the antenna, and the relative IBW of the antenna can be more than 30%. As shown in Fig. 7 (b), all configurations of the proposed antenna yield several minimum points in their AR profiles. One minimum point for 3 × 3 cells, two minimum points for 4 × 4 cells, and three minimum points for 6 × 6 cells. However, the 5 × 5 cell configuration yields an optimized result in terms of broad ARBW.

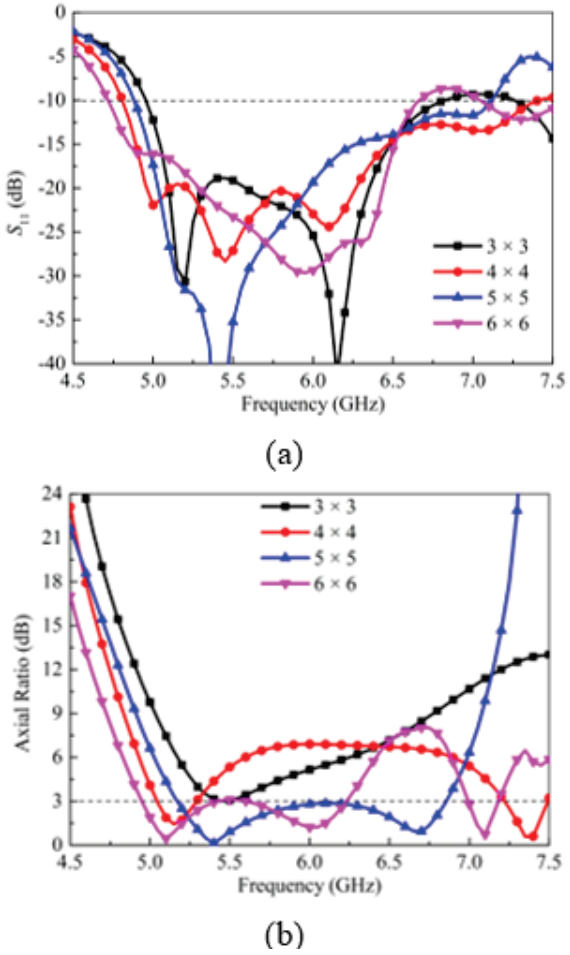

Fig. 7. Simulated (a) S_{11} and (b) AR values for different numbers of unit cells.

V. FABRICATION AND MEASUREMENT

The antenna is fabricated and measurements are performed to show the design effectiveness of the low profile wideband circularly polarized antenna. Figure 8 depicts the antenna's physical maps, with the front view on the left and the back view on the right. Agilent E5071C vector network analyzer is used to test the reflection coefficients of the antenna, and the results show −10 dB relative IBW of the antenna is 39.8% (4.82-7.22 GHz) as shown in Fig. 9. The test findings differ slightly from the simulation results, but they show a similar frequency variation trend. Furthermore, the operational bandwidths are essentially the same.

The antenna attains a 3 dB ARBW of 30% (5.1-6.9 GHz), which is slightly broader than the simulated results, as shown in Fig. 10. At 5.4 GHz and 6.7 GHz, the antenna axial ratios are 0.15 dB and 0.65 dB, respectively, indicating that circular polarization performed well. In the circularly polarized bandwidth, the gain

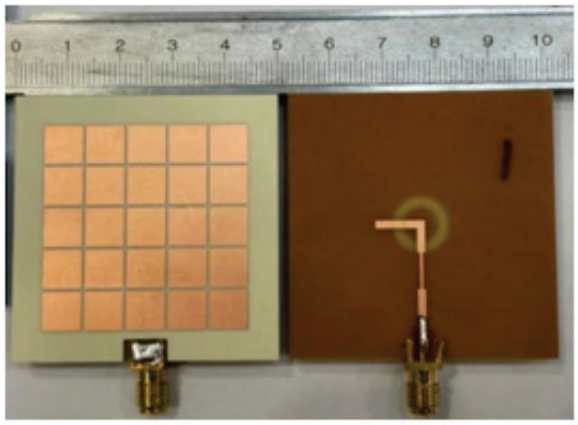

Fig. 8. Antenna physical map.

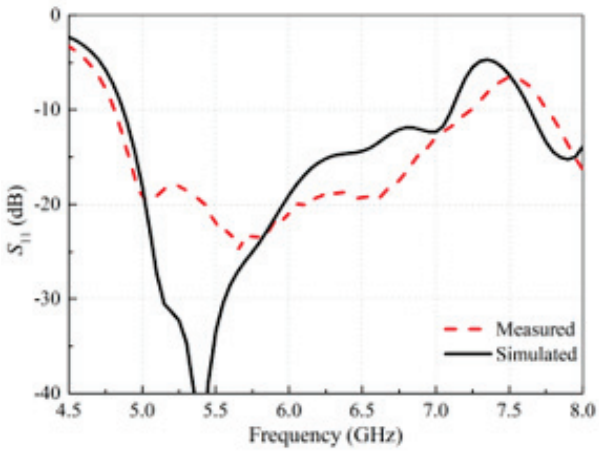

Fig. 9. Reflection coefficient of the antenna.

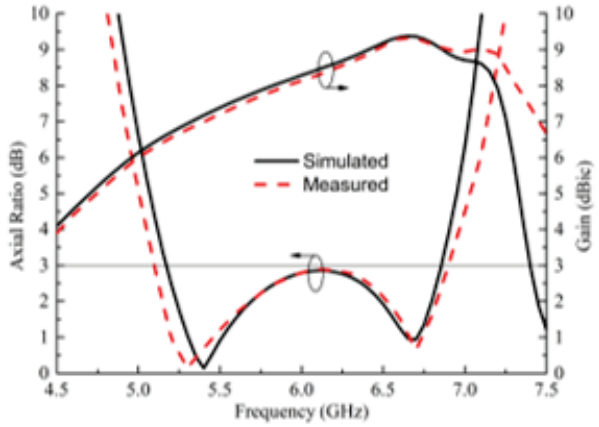

Fig. 10. Axial ratio and gain of the antenna.

in the boresight radiation direction of the antenna is higher than 6.3 dBic, and the peak gain reaches 9.3 dBic at 6.65 GHz, which means that the gain in the circularly polarized bandwidth is fluctuating within the range of 3 dB. As shown in Fig. 11, the simulated and the measured radiation efficiency are both higher than 88% throughout the 3 dB ARBW.

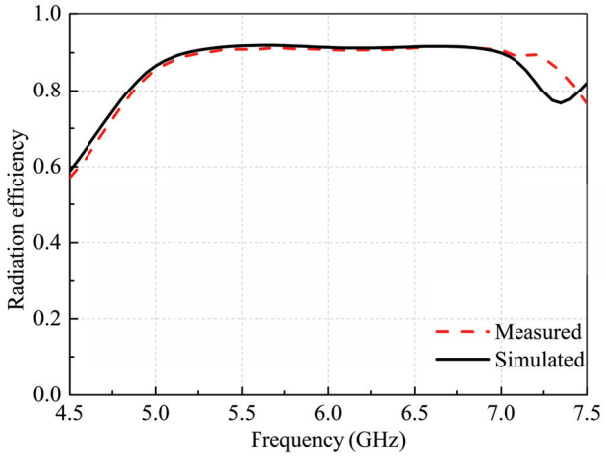

Fig. 11. Simulated and measured radiation efficiency.

Figure 12 shows the designed antenna's normalized far-field radiation pattern diagram, with (a) and (b) representing the radiation directly on the *xoz* and *yoz* planes at 5.4 GHz. Figures 12 (c) and (d) represent the radiation directly on the *xoz* and *yoz* planes at 6.7 GHz. The measured and predicted far-field radiation directional diagrams are almost identical, implying that the antenna produces steady and symmetric unidirectional axial radiation with clear LHCP radiation at both frequencies. The radiation gain is 7.0 dBic at 5.4 GHz, with a front-to-back ratio of 21.2 dB and a half-power beamwidth of 68°. The radiation gain is 9.3 dBic 6.7 GHz, with a front-to-back ratio of 24.8 dB and a half-power beamwidth of 46°. Additionally, the good symmetry in the radiation directional diagram suggests that the designed feed structure can effectively excite the J_1 and J_2 eigenmodes of the MTS in the characteristic mode analysis.

Performance comparisons between the designed antenna and the circularly polarized MTS antenna obtained from the literature are shown in Table 2. The developed antenna is found to have the widest 3 dB ARBW and higher radiation gain while preserving low-profile features. Overall, an antenna has been designed to have a low-profile, high gain, and wide bandwidth performance.

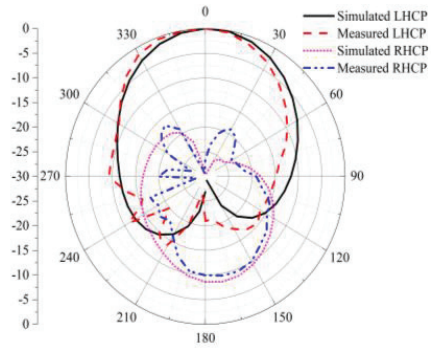

(a) Radiation pattern on *xoz* plane at 5.4 GHz

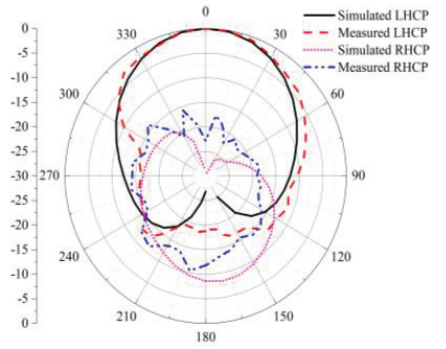

(b) Radiation pattern on *yoz* plane at 5.4 GHz

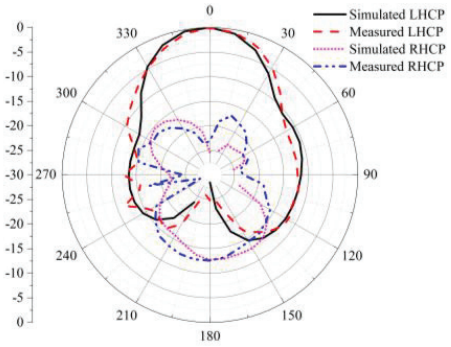

(c) Radiation pattern on *xoz* plane at 6.7 GHz

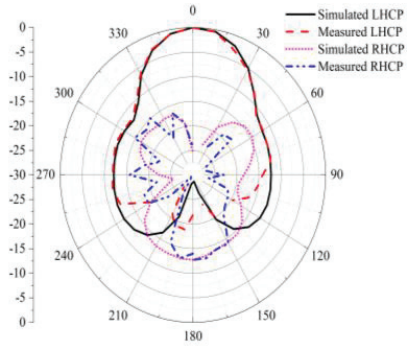

(d) Radiation pattern on *yoz* plane at 6.7 GHz

Fig. 12. Normalized far-field radiation pattern diagram of the designed antenna.

Table 2: Performance comparisons between the designed antenna and the antenna in the literature

Ref	Size (λ^3)	Frequency (GHz)	S_{11}	AR	Pink Gain (dBic)
[8]	0.58*0.58*0.0056	5.5	45.6%	23.4%	7.6
[9]	0.93*0.93*0.054	6.35	55.4%	23.6%	8.1
[10]	0.93*0.93*0.024	1.51	17.0%	14.5%	9.0
[11]	1.4*1.4*0.072	5.6	38.8%	14.3%	9.4
[12]	1.0*1.0*0.07	5.5	28.2%	20.9%	9.7
Proposed	1.0*1.0*0.056	6.0	39.8%	**30.0%**	9.3

VI. CONCLUSION

A wideband circularly polarized MTS antenna is proposed. The characteristic mode analysis is utilized to design the presented antenna. For the creation of circularly polarized radiation, a feed network consisting of an L-shaped microstrip and an annular slot etched on the ground contact is used to simultaneously excite the desired orthogonal modes and produce a phase difference of 90°. The experimental results and simulations show that the antenna has a low profile, high gain, and wide bandwidth, which is promising for modern wireless communication applications, such as satellites and radar, where high gain and wide bandwidth are crucial.

ACKNOWLEDGMENT

This work is supported by the Science Research Project of the Education Department of Anhui Province under Grant KJ2021A1024, the Domestic Visiting Study Program for Outstanding Young Talents in Colleges under Grant gxgnfx2021145.

REFERENCES

[1] A. J. A. Al-Gburi, Z. Zakaria, H. Alsariera, M. F. Akbar, I. M. Ibrahim, K. S. Ahmad, S. Ahmad, and S. S. Al-Bawri, "Broadband circular polarised printed antennas for indoor wireless communication systems: A comprehensive review," *Micromachines*, vol. 13, no. 7, pp. 1048, 2022.

[2] J. Li, C. Wang, A. Zhang, W. T. Joines, and Q. H. Liu, "Microstrip-line-fed reactively loaded circularly polarized annular-ring slot antenna," *J Electromagn Waves Appl.*, vol. 31, no. 1, pp. 101-110, 2017.

[3] N. Rasool, H. Kama, M. A. Basit, and M. Abdullah, "A low profile high gain ultra lightweight circularly polarized annular ring slot antenna for airborne and airship applications," *IEEE Access*, vol. 7, pp. 155048-155056, 2019.

[4] J. S. Row, "The design of a squarer-ring slot antenna for circular polarization," *IEEE Trans Antennas Propag*., vol. 53, no. 6, pp. 1967-1972, 2005.

[5] J. S. Row, "Design of aperture-coupled annular-ring microstrip antennas for circular polarization," *IEEE Trans Antennas Propag*., vol. 53, no. 5, pp. 1779-1784, 2005.

[6] H. Alwareth, I. M. Ibrahim, Z. Zakaria, A. J. A. Al-Gburi, S. Ahmed, and Z. A. Nasser, "A wideband high-gain microstrip array antenna integrated with frequency-selective surface for sub-6 GHz 5G applications," *Micromachines*, vol. 13, no. 8, pp. 1215, 2022.

[7] Z. J. Han, W. Song, and X. Q. Sheng, "Broadband circularly polarized antenna by using polarization conversion metasurface," *Applied Computational Electromagnetics Society (ACES) Journal*, vol. 35, no. 6, pp.656-661, 2020.

[8] S. X. Ta and I. Park, "Low-profile broadband circularly polarized patch antenna using metasurface," *IEEE Trans Antennas Propag*., vol. 63, no. 12, pp. 5929-5934, 2015.

[9] W. Q. Cao, B. N. Zhang B, W. Hong, and J. Jin, "L-shaped slot coupling-fed low-profile broadband circularly polarized patch antenna with metasurface," *J Electromagn Waves Appl.,* vol. 31, no. 1, pp. 111-120, 2017.

[10] S. Liu, D. Yang, and J. Pan, "A low-profile circularly polarized metasurface antenna with wide axial-ratio beamwidth," *IEEE Antennas Wirel Propag Lett*., vol. 18, no. 7, pp. 1438-1442, 2019.

[11] C. Zhao and C. F. Wang, "Characteristic mode design of wide band circularly polarized patch antenna consisting of H-shaped unit cells," *IEEE Access*, vol. 6, pp. 25292-25299, 2018.

[12] X. Gao, G. Tian, Z. Shou Z, and S. Li, "A low-profile broadband circularly polarized patch antenna based on characteristic mode analysis," *IEEE Antennas Wirel Propag Lett*., vol. 20, no. 2, pp. 214-218, 2021.

[13] A. Sharma, D. Gangwar, B. K. Kanaujia, and S. Dwari, "Gain enhancement and broadband RCS reduction of a circularly polarized aperture coupled annular-slot antenna using metasurface," *J Comput Electron*., vol. 17, no. 3, pp. 1037-1046, 2018.

[14] K. E. Kedze, H. Wang, and I. Park, "A metasurface-based wide-bandwidth and high-gain circularly polarized patch antenna," *IEEE Trans Antennas Propag*., vol. 70, no. 1, pp. 732-737, 2022.
[15] F. H. Lin and Z. N. Chen, "Low-profile wideband metasurface antennas using characteristic mode analysis," *IEEE Trans Antennas Propag*., vol. 65, no. 4, pp. 1706-1713, 2017.
[16] Z. Song, J. Zhu, L. Yang, P. Min, and F. H. Lin, "Wideband metasurface absorber (metabsorber) using characteristic mode analysis," *Opt Express*, vol. 29, no. 22, pp. 35387-35399, 2021.
[17] F. H. Lin and Z. N. Chen, "Resonant metasurface antennas with resonant apertures: Characteristic mode analysis and dual-polarized broadband low-profile design," *IEEE Trans Antennas Propag*., vol. 69, no. 6, pp. 3512-3516, 2021.
[18] B. B. Q. Elias, P. J. Soh, A. A. Al-Hadi, P. Akkaraekthalin, and G. A. Vandenbosch, "A review of antenna analysis using characteristic modes," *IEEE Access*, vol. 9, pp. 98833-98862, 2021.
[19] S. Z. Zhao, X. P. Li, Y. X. Chen, W. Y. Zhao, and Z. H. Qi, "A wide-beam metasurface antenna using pattern combination of characteristic modes," *Applied Computational Electromagnetics Society (ACES) Journal*, vol. 37, no. 1, pp. 41-49, 2022.

Shuangbing Liu was born in Anqing City, Anhui Province, China, in 1982. He received a B.S. degree in physics from Anhui Normal University, Wuhu, China, in 2005, and an M.S. degree in Electromagnetic and Microwave Technology from Anhui University, Hefei, China, in 2008.

Since 2017, he has been an Associate Professor at the Electronic Engineering Department, Chaohu University, Hefei, China. Now, he is a Visiting Scholar in Electronic Information Engineering Department, Anhui University, Hefei, China. His current research interest is antenna theory and design in wireless communication systems.

Lixia Yang was born in Enzhou, Hubei, China, in 1975. He received a B.S. degree in Physics from Hubei University, Wuhan, China, in 1997, and a Ph.D. degree in Radio Physics from Xidian University, Xi'an, China, in 2007. Since 2010, he has been an Associate Professor at the Communication Engineering Department, Jiangsu University, Zhenjiang, China. From 2010 to 2011, he was a Postdoctoral Research Fellow with the Electro-Science Laboratory (ESL), The Ohio State University, Columbus, OH, USA. From 2015 to 2016, he was a Visiting Scholar with the Institute of Space Science, The University of Texas at Dallas, Dallas, TX, USA. From 2016 to 2019, he has been a Professor and a Ph.D. supervisor, and the Chairman of the Communication Engineering Department, Jiangsu University. Since 2020, he has been a Distinguished Professor and a Ph.D. supervisor, and the Vice Dean of the School of Electronic and Information Engineering, Anhui University, Hefei, China. His research interests include wireless communication techniques, radio sciences, computational electromagnetics, and antenna theory and design in wireless communication systems. He is a member of the Editor Board of Radio Science Journal in China.

Xianliang Wu was born in Bozhou, Anhui, China, in 1955. He is a second-level Professor, a Ph.D. supervisor, and an Academic and Technological Leader of Anhui Province. He has been engaged in teaching and scientific research in electromagnetic field theory, mobile communications, electromagnetic scattering theory of complex targets, and electromagnetic field numerical calculation. He has presided over one key project and five normal projects of the National Natural Science Foundation of China, two doctoral fund projects of the Ministry of Education, one major national basic research project, one major national scientific and technological research project, and more than 20 provincial and ministerial level, enterprises and institutions commissioned development projects. He has authored or co-authored over 200 articles, including 185 articles indexed by SCI or EI. He has also authored two books. He is a Senior Member of the Chinese Institute of Electronics.

A Noninvasive Method for Measuring the Blood Glucose Level Using a Narrow Band Microstrip Antenna

Ayman R. Megdad, Rabah W. Aldhaheri, and Nebras M. Sobahi

Department of Electrical and Computer Engineering
King Abdulaziz University, Jeddah, 21589, Saudi Arabia
A.mkdad93@gmail.com, Raldhaheri@kau.edu.sa, Nsobahi@kau.edu.sa

***Abstract* –** In this paper, a narrowband and compact antenna resonating at 6.1 GHz with a peak realized gain of 3.3 dBi is proposed to monitor the glucose concentration in the blood without taking invasive blood samples. The proposed antenna is fabricated using a low-cost FR-4 substrate with compact dimensions of 30 mm × 30 mm × 1.6 mm. The impedance bandwidth of this antenna ranges from 5.2 to 7.1 GHz. For measuring blood glucose levels, a human finger phantom model with dimensions of 15 mm × 12 mm × 10 mm is constructed using the EM simulation (HFSS) environment. The finger phantom consists of different layers such as skin, fat, muscle, blood, and bone modeled at 6.1 GHz using various dielectric materials for various glucose concentrations. The finger phantom model is placed at different locations around the antenna to measure the frequency shift for monitoring glucose concentration in blood samples. The proposed finger phantom model is validated by conducting an experimental study by placing a real human finger around the fabricated antenna and measuring the frequency shift. This study shows a very good agreement with the results obtained by the simulated phantom model. The advantages and outperformance of the proposed sensor are highlighted in terms of the sensitivity obtained and compared with other techniques given in the literature.

***Index Terms* –** glucose levels, directional antenna, non-invasive, narrow band antenna.

I. INTRODUCTION

In most cases, diabetes is caused by very high levels of glucose in the blood over a prolonged period, which is the primary feature of diabetes [1–2]. According to the World Health Organization (WHO) and the International Diabetes Federation (IDF), there are 463 million individuals worldwide who have diabetes, with more than 60 percent of the population living in the "risk zone." It is recommended that this identification be performed at frequent intervals to improve the accuracy of the results. The detection of diabetics may be accomplished with the use of finger prick tests and glucose meters [3–4], although this approach is considered intrusive. It is occasionally necessary to sandwich the liquid under investigation between two microstrip resonators. On the other hand, invasive procedures hurt the patient because blood samples must be taken often.

As reported in [5], a band-stop filter with a defective ground structure (DGS) was employed to monitor glucose levels intravenously. Furthermore, the sensitivity to changes in glucose levels in blood samples as well as the depth of penetration is lower than previously reported. However, when it comes to testing blood sugar levels, various options are discussed [6–12]. Furthermore, several innovative microwave sensors were presented by Lukas in [13], and another pressure sensor was proposed by Satish in [14]. A technique for determining glucose levels was developed by Deshmukh, and Ghongade, who used a ring resonator to calculate the dielectric properties and estimate the glucose levels [15]. The authors of [16] addressed the measurement of glucose in the presence of animal tissues by utilizing mm-wave methods in the presence of animal tissues. In addition, in [17–23], numerous innovative approaches for more accurately calculating glucose concentration in blood samples were reported.

Microwave filters or antennas are employed for monitoring glucose levels in the blood [24–25]. This is a non-invasive technology that has been developed. Their great sensitivity to minor fluctuations in glucose levels, as well as their simplicity of deployment, make antenna systems the most common of all non-invasive glucose monitoring technologies. [26–28]. Furthermore, since they do not ionize, they penetrate deeply, are resistant to noise, temperature, and other disturbances, and are widely used in the medical area as well as other fields. The authors of [26] developed an artificial hand with a finger phantom and used it to compute glucose concentrations in blood samples by simulating S-parameters and evaluating the dependence of frequency shift on dielectric parameters. The antenna that has been created functions at frequencies ranging from 1 to 6 GHz. However, because of the omnidirectional radiation pattern produced by this antenna, it is not recommended

Submitted On: August 23, 2022
Accepted On: January 4, 2023
https://doi.org/10.13052/2022.ACES.J.371102

for practical use. Ref [27] describes the construction of a patch antenna that can operate at 2.4 and 5.8 GHz and is filled with deionized water and glucose for use in medical applications. The antenna match was altered in response to changes in glucose levels. Ref. [28] describes the development of phantom-loaded patch components for use in an antenna operating at a frequency of 4.75 GHz. A range of liquid phantoms, including pig blood and physiological solutions, were evaluated, with glucose levels ranging from 150 mg/dL to 550 mg/dL in the samples analyzed. The solution induced a linear change in frequency of 5 MHz, which was observed. Even though the temperature and volume of the test samples varied, there was no link between the readings. Meta-materials can also be utilized to detect glucose, as described in [29]. Recent review papers explain in detail the current state of research on glucose level monitoring sensors and the need to build more sensitive sensors [30–38].

To monitor glucose levels, a microstrip antenna is used as a microwave sensor operating at 6.1 GHz. Furthermore, a human finger phantom is designed with a length of 15 mm, a height of 10 mm, and a width of 12 mm, with layers of skin, fat, muscle, blood, and bone. However, the key innovation of this study is that the proposed antenna produces a significant frequency change when a finger phantom is placed on it to measure glucose levels.

The remainder of the paper's structure is as follows: In Section 2, the microstrip antenna structure, design method, and parametric study are described. Section 3 presents results and discussion, including the modeling of a finger phantom and an associated study on frequency shifts for different positions of the finger phantom and varying glucose levels. In Section 4, the paper is concluded.

II. ANTENNA STRUCTURE

The proposed antenna is designed and optimized using the ANSOFT HFSS electromagnetic simulator. Figure 1 illustrates the evolution of the antenna design until we reach the final proposed antenna (Antenna 3). As is customary in antenna design, Antenna 1 is designed by doing an initial theoretical calculation to determine the dimensions of the initial antenna, as seen in Fig. 1. The first antenna has a half-elliptic shaped and is fed by a 50-ohm feedline with a partial ground plane on the substrate's back side. The current distribution of antenna 1 is depicted in Fig. 2, where the current distribution is minimal in the patch's central half. As a result, this portion can be removed, and then a rectangular and half-elliptic slot is etched in the middle, as shown in Fig. 1 (b) and Fig. 1 (c). This rectangular and half-elliptic slot is responsible for shifting the resonant frequency, as explained below. In the next step, to obtain one resonant frequency, a rectangular cut-out in the upper center of the ground is constructed for all designs, as illustrated in Fig. 1 (d). From the reflection coefficient values plotted for all the three antennas given in Fig. 3, it is observed that antenna 3 gives the desired resonant band from 5.2 to 7.1 GHz with a resonant frequency of 6.1 GHz, which is the required frequency for glucose monitoring in blood samples. Hence, antenna 3 is considered the proposed antenna to meet the target application (glucose monitoring).

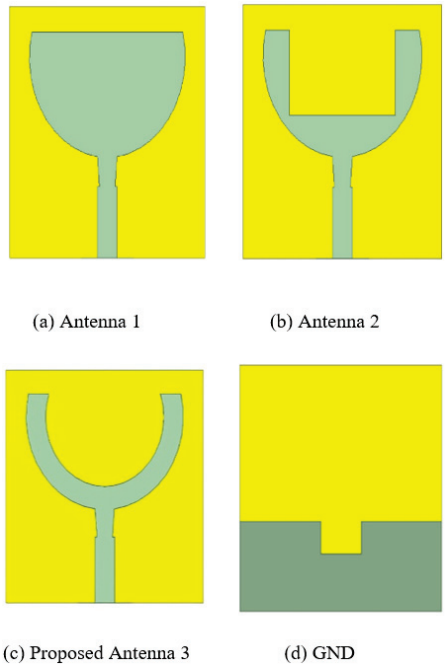

Fig. 1. Evolution of the proposed antenna. (a-c) Top views of Antennas 1, 2, and 3. (d) Bottom view.

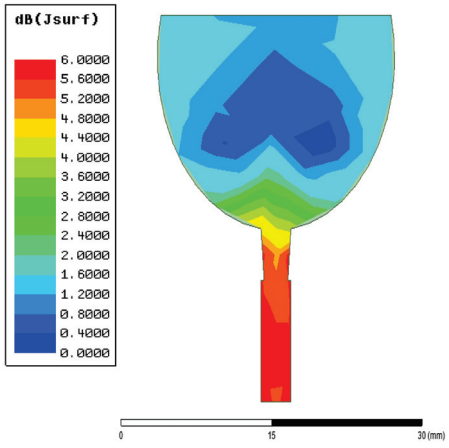

Fig. 2. Current distribution of Antenna 1 at 6 GHz.

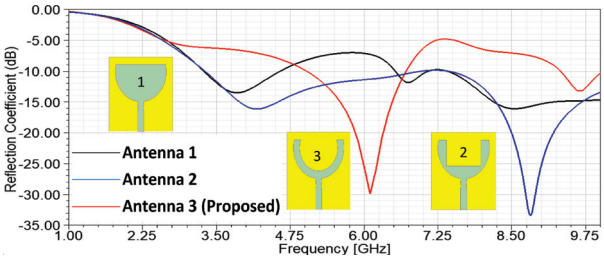

Fig. 3. Simulated reflection coefficient of Antenna 1, Antenna 2, and Antenna 3.

A. Design procedure of the proposed antenna

Figure 4 depicts the schematic view of the proposed antenna. The antenna is made from an FR4 substrate with a relative permittivity of 4.4, a thickness of 1.6 mm, and a loss tangent of 0.02. To achieve a 50-Ohm input impedance match, a rectangular and trapezoidal-shaped feed is employed to feed the antenna. The antenna consists of a rectangular ground plane with a rectangular cut-out in the top center of the ground, as seen in Fig. 4 (b), and a half-ellipse with a major radius W2 and minor radius L1, as shown in Fig. 4 (a).

The antenna is a planar patch antenna with a U-shaped patch. The optimized element dimensions are listed in Table 1, and the antenna is optimized to operate at 6.1 GHz. The U-shaped design has a critical role to play in achieving desired radiation properties with enhanced gain, which is the primary characteristic required for estimating the glucose level. The half-elliptic slot is etched away from the radiating area, and this is used for shifting the band characteristics for monitoring glucose levels.

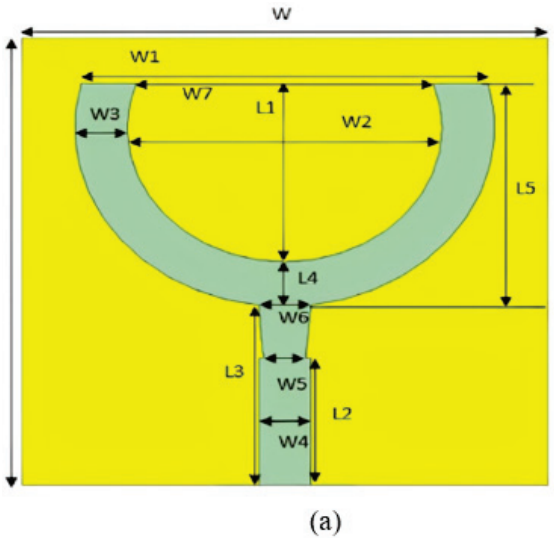

Fig. 4. (*Continued*).

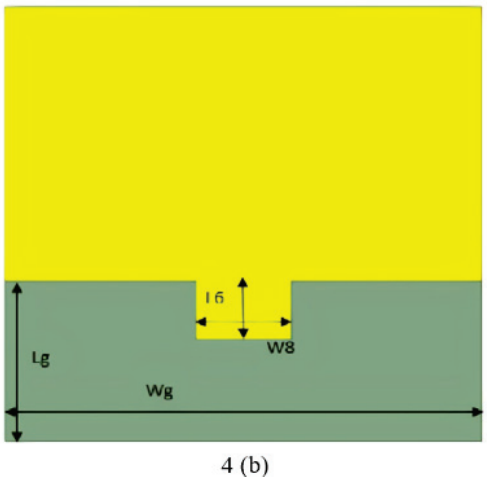

Fig. 4. Geometry of proposed antenna, (a) Top view. (b) Back view.

B. Parametric study

Figure 5 depicts the finalized antenna structure's surface current distributions. At 6.1 GHz, it is seen that a significant number of current flows through the patch, indicating that this antenna is a good radiator at the selected frequency. A parametric study on various dimensions of the antenna is performed to characterize the antenna's radiating behavior.

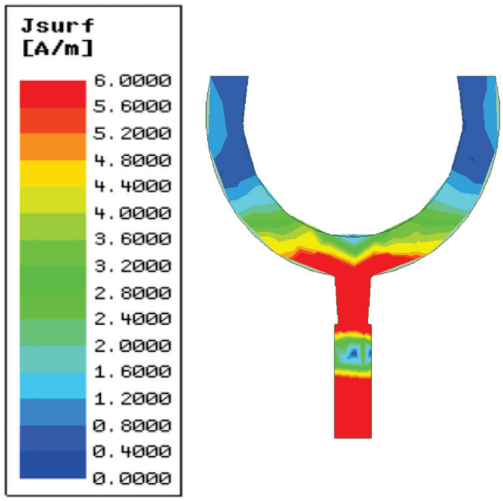

Fig. 5. Current distribution of proposed antenna at 6.1 GHz.

The parametric analysis is performed concerning the parameters W2, W5, and L2 of half-elliptic slots, as shown in Figs. 6, 7 and 8 respectively. From Fig. 6, it is observed that better reflection coefficient values are obtained for W2 = 18 mm. Similarly, from Fig. 7, it is observed that W5 = 2.4 mm yields good reflection coefficient values. Similarly, from Fig. 8, it is observed that

good reflection coefficient values in the desired band are obtained for L2 = 8.5 mm. The final results of the optimal parameters are listed in Table 1.

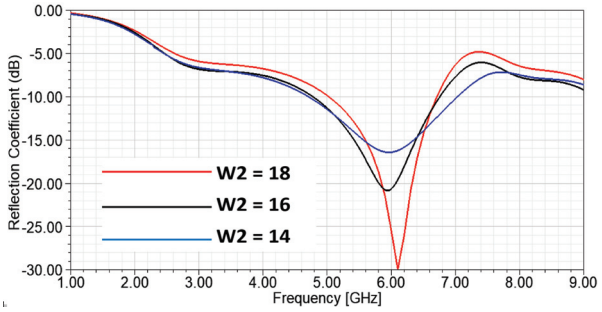

Fig. 6. Parametric analysis w.r.t. W2.

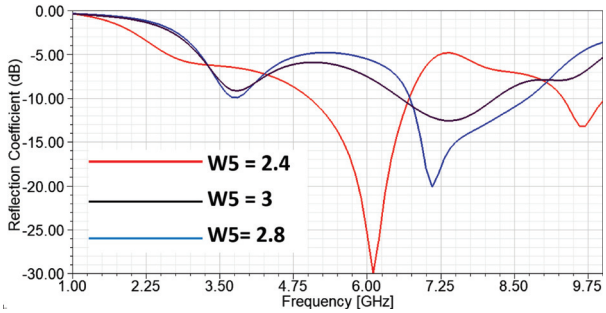

Fig. 7. Parametric analysis w.r.t. W5.

Table 1: Dimensions of the Proposed Antenna

Parameters	Dimension (mm)
L	30
W	30
Lg	11
Wg	30
W1	23.24
W2	18
W3	3.12
W4	3
W5	2.4
W6	3
W7	17
W8	6
L1	11.88
L2	8.5
L3	12
L4	3.12
L5	15
L6	4

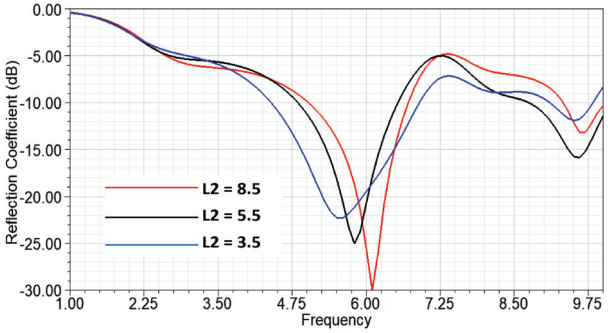

Fig. 8. Parametric analysis w.r.t. L2.

III. RESULTS AND DISCUSSION

The proposed antenna is manufactured and tested to evaluate the performance of the optimized antenna. The prototype of the fabricated antenna is given in Fig. 9. The reflection coefficient and radiation patterns of the proposed antenna are measured using the Vector

(a)

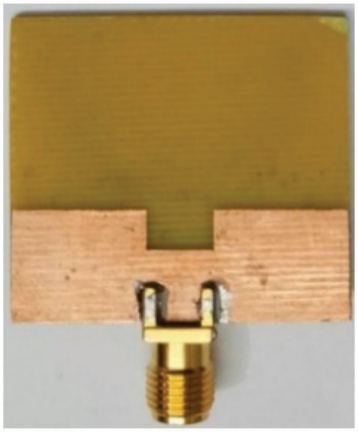

(b)

Fig. 9. Fabricated Prototype of the proposed antenna (a) Top view. (b) Bottom view.

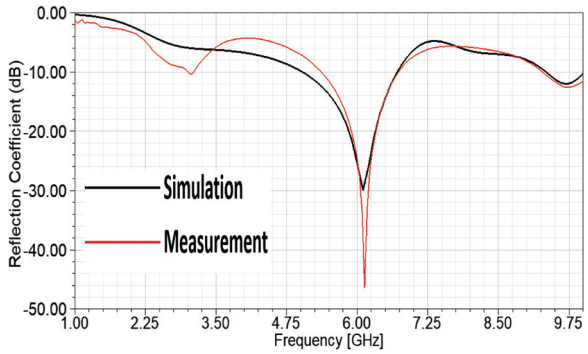

Fig. 10. Simulated and measured S11 parameters of the proposed antenna.

Network Analyzer (VNA) N5225A. Figure 10 shows the simulated and measured S-parameters of the proposed antenna, showing the antenna resonating at 6.1 GHz. The simulated results are found to be in good agreement with the measured results. The slight variation between the results is due to the fabrication tolerances at the feed location.

Figure 11 illustrates the simulated and measured E-plane and H-plane radiation patterns at 6.1 GHz, respectively. From the resulting radiation patterns, it can be observed that the antenna is oriented towards 90 degrees on the E-plane, as shown in Fig. 11 (a), and that the radiation is almost omnidirectional on the H-plane, as shown in Fig. 11 (b). The three-dimensional radiation pattern created by the antenna is seen in Fig. 12. The antenna has strong directional qualities at 6.1 GHz with a realized gain of 3.3 dBi, which is good enough to attribute to employing this antenna for monitoring the concentration of glucose in the finger phantoms.

A. Modeling of finger phantom & evaluation of glucose concentration

In particular, the current research effort is focused on the development of an antenna that is capable of monitoring glucose concentration fluctuations in blood from the fingertips. To do this, a finger phantom model is created in an HFSS environment to mimic the real human finger as given in Fig. 13. For the simulation of various layers of the finger such as skin, fat, muscle, blood, and bone, dielectric materials with variable dielectric constants and conductivities are utilized. The central layer to consider is the finger's bone region, which is seen in white color in Fig. 13. The blood in the finger is shown as a red color next to the bone. The muscle is next to blood and is represented by a yellow color. Following muscle is the fat layer, which is represented by a pink color, and the last layer is the skin, which is represented by a light yellow color. The thicknesses of the different layers of the finger phantom are shown in Fig. 13 as well as their dielectric constants, which are listed in Table 2 [31–38].

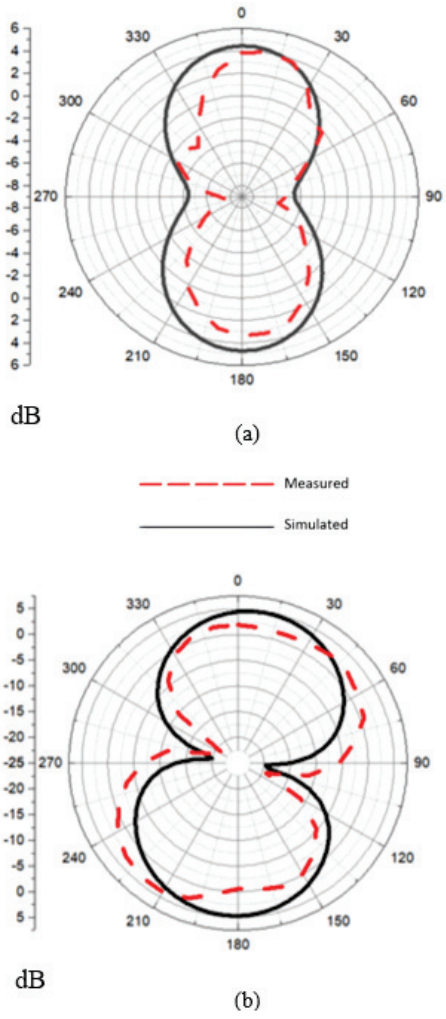

Fig. 11. Simulated and measured radiation patterns on (a) E-plane and (b) H-plane. At 6.1 GHz.

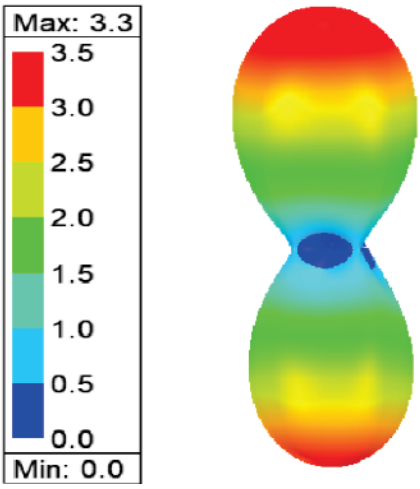

Fig. 12. 3D radiation pattern at 6.1 GHz with maximum realized gain 3.3 dBi.

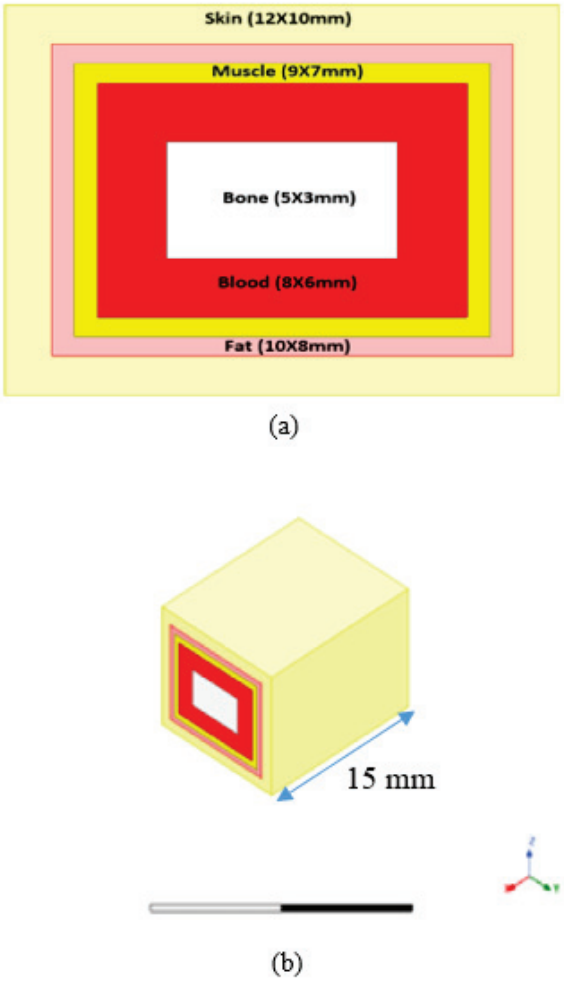

Fig. 13. Finger phantom model. (a) Top view. (b) Isometric view.

Table 2: Dielectric constant, conductivity, loss tangent, and thickness of Finger Phantom at 6.1 GHz

Phantom Parameters	ε_r	σ (S/m)	Loss Tangent
Skin	34.9	3.9	0.3336
Fat	4.9	0.3	0.1871
Muscle	48.1	0.3	0.3263
Blood	52	6.9	0.3933
Bone	9.54	1.2	0.3788

As shown in Fig. 14, the resonant frequencies and reflection coefficients of the phantom placed at the top of the radiation element are simulated for various thicknesses of muscle and fat, and the results are compared with the resonant frequencies and reflection coefficients of a real human finger placed at the top of the radiation element, as seen in Fig. 18 (a), to determine the thickness that is closest to the real thicknesses of muscle and fat for the human finger. The selected thickness is the one reported in [31–38] and given in Fig. 13 (a). Moreover, these selections are validated by placing a real human finger at the top of the antenna. The obtained results with the given dimensions of the phantom showed to a far extent that this phantom resembles the real human finger.

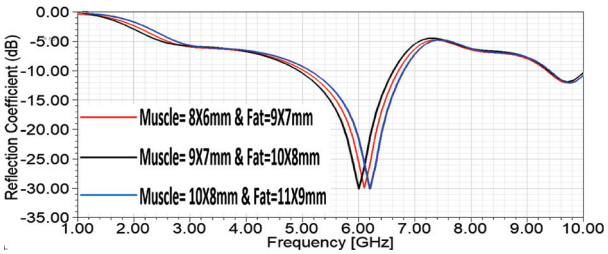

Fig. 14. The resonant frequencies and reflection coefficients for different thicknesses of muscle and fat.

For the most part, a phantom finger is placed at various positions on the antenna, such as the top of the radiating element and the middle of the radiating element, as shown in Figs. 8 and 19, with their reflection coefficients, respectively.

The frequency shifts of the finger phantom, which is placed on top of the radiating element, are used to detect changes in glucose concentration. When the finger phantom is placed on the radiating element, a similar shift in the magnitude of the reflection coefficient is shown to have occurred. Placing the finger phantom at the top of the radiating element is the most effective method of obtaining glucose concentration in this configuration, as this case gives a good amount of frequency shift. Table 3 shows the different frequency shifts obtained for various finger phantom positions on the antenna.

Table 3: The resonant frequencies and reflection coefficients for different places of finger phantoms

Position of the Phantom	Resonant Frequency (GHz)	S11 (dB)
Without phantom	6.1	-30
Phantom at the top of the radiating element.	6.1	-30
Phantom at the center of the radiating element.	6.3	-31

The phantom is placed above the top of the radiating element by adjusting the glucose concentration from 0 to 500 mg/dL throughout a range of time. As the glucose

content in the finger phantom increases, the resonant frequency increases, as seen in Fig. 15. Antenna resonance occurs at 5.71 GHz when the glucose level is 75 mg/dL and the S11 is -29.9 dB. There is a resonance at 5.97 GHz for an amount of 175 mg/dL glucose concentration with a -32.5 dB reflection coefficient value, and there is another resonance at 6.18 GHz for 225 mg/dL glucose concentration with a -34.6 dB reflection coefficient value. The antenna has a distinct frequency shift in response to variations in glucose concentrations, making it an excellent candidate for determining glucose concentrations in the bloodstream. Table 4 describes the relationship between the dielectric constant and glucose levels. Figure 16 shows the relationship between the dielectric constant and glucose levels at 5.5, 6.0, and 6.5 GHz. As seen from this figure, the dielectric constant decreases as the glucose concentration increases. Moreover, as the frequency increases, the dielectric constant decreases.

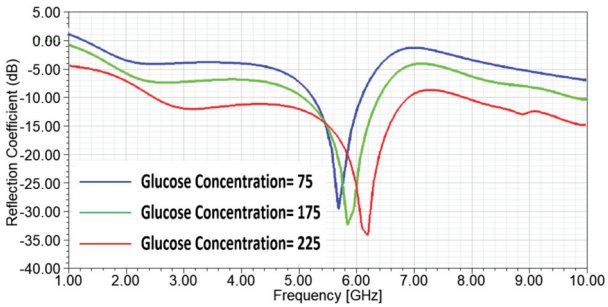

Fig. 15. illustrates the variations of S11-Parameters versus the frequency at different glucose concentrations mg/dl when the finger phantom model is placed on the top of the radiating element.

Table 4: Dielectric Constant values for different Glucose concentrations

Glucose Concentration (mg/dL)	ε_r
0	64.5
125	64.25
250	64
375	63.75
500	63.5
625	63.25
750	63
875	62.75
1000	62.5

At 5.5, 6.0, and 6 GHz, it is evident from Fig. 16 that the dielectric constant drops by a consistent amount while the glucose concentration rises. This demonstrates

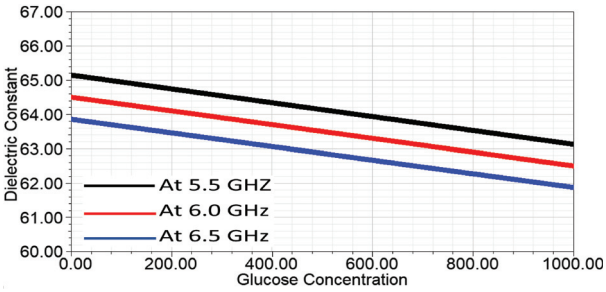

Fig. 16. Dielectric Constant values for different Glucose concentrations at 5.5, 6, and 6.5 GHz.

that the proposed antenna sensor is an excellent option for measuring glucose levels in the blood.

B. Measurement of reflection coefficient for various real finger and phantom model positions

The main idea of the presented work is to design and develop an antenna sensor that can measure the glucose concentration in blood samples from diabetic patients. The sensor works on the principle of frequency shift variations w.r.t the variations of glucose in patients' blood samples. This change in glucose concentration is modeled using various dielectric constants of different finger layers like skin, fat, muscle, blood, and bone as given in Table 2. Also, the variations of the dielectric constant w.r.t glucose concentration are given in Table 4 and Fig. 16. The proposed antenna sensor is unique and can be used for any diabetic patient having different levels of glucose changes. These glucose changes are mapped to the resonant frequency shifts, and the sugar levels in the patient can be easily estimated.

To validate the performance of the proposed antenna for measuring glucose concentration, the finger of a normal, healthy individual is inserted in various positions around the antenna, and frequency changes are measured. It should be mentioned that the purpose of this experiment is to demonstrate the frequency shift and the reflection coefficients when a real finger is placed at different positions of the radiating element of the antenna. Similarly, we put the designed phantom model in the same positions to figure out how this phantom model resembles the real human finger. The reflection coefficient and the resonant frequency for both the real finger and the phantom model are shown in Figs. 18 and 19.

Starting with Fig. 17, where there is no real finger or phantom placed near the antenna, the measured return loss is -46 dB and the resonant frequency is 6.1 GHz. When the finger is placed on top of the radiating element, the resonance frequency is moved to 6.15 GHz and the reflection coefficient is -39.1 dB for the finger (red line) and -30 dB for the designed phantom (black line), as seen in Fig. 18 (a)-(c). Putting the finger at the

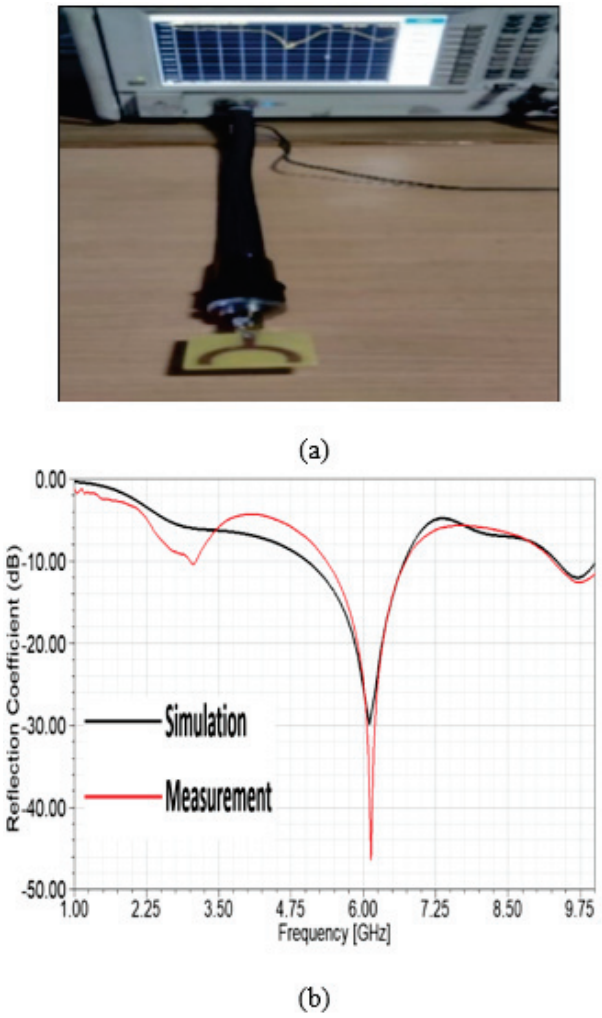

Fig. 17. (a) Measured and simulated reflection coefficient for the fabricated antenna with no finger or phantom around the antenna. (b) Setup and the reflection coefficient.

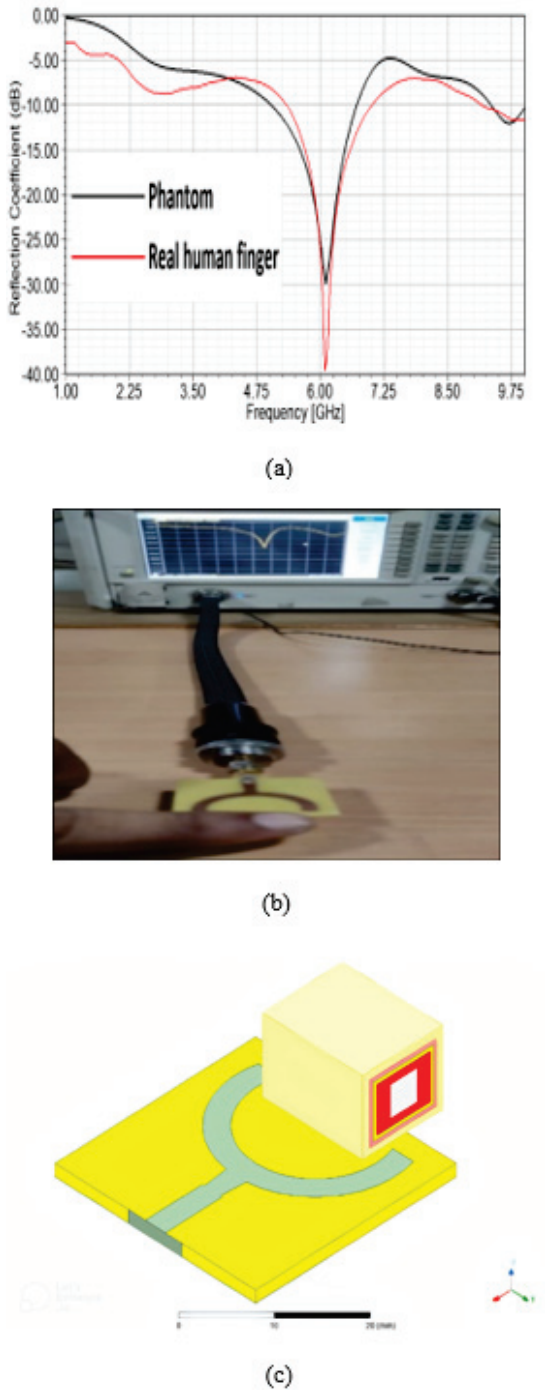

Fig. 18. (a) Measurement and simulation of the reflection coefficient by placing the finger and the phantom on top of radiating element as in (b and c).

center of the radiating element, the resonance frequency is 6.3 GHz and the reflection coefficient is -42 dB for the real finger and -31 dB for the phantom model, as shown in Figs. 19 (a)-(c). These results reflect how close the results obtained by the proposed phantom model are to those obtained by the human real finger. After performing many simulations, it was found that the best place to put the phantom model was at the top of the radiating part of the antenna. With this in mind, we varied the glucose concentration from 0 to 500 mg/dL and measured the frequency shift, and the results are listed in Table 5. From these results, it is observed that the frequency shift can be utilized to detect the glucose level in the blood. As seen from this table, when the glucose concentration is varied from 0 to 75 mg/dL, a frequency shift of 210 MHz is observed. When the concentration is varied from 75 mg/dL to 125 mg/dL, a frequency shift of 130 MHz, is observed. Similarly, the variation of glucose concentration from 125 to 175 mg/dL gives a frequency shift of 130 MHz, and so on. The frequency shift is dropped to 60 and 50 MHz when the concentration is varied

Table 5: Summary of resonant frequencies obtained for different Glucose Concentrations

Glucose Concentration (mg/dL)	Resonant Frequency (GHz)	Bandwidth (GHz)	Frequency Shift (MHz)	Sensitivity (MHz/ (mg/ dL))	S_{11} (dB)
0	5.50	1.6966	—-	–	29.8574
75	5.71	1.6954	210	2.8	29.9353
125	5.84	1.6950	130	1.04	31.9547
175	5.97	1.6949	130	0.74	32.5241
225	6.18	1.6944	210	0.93	34.6241
275	6.28	1.6940	100	0.36	34.9246
325	6.37	16936	90	0.28	35.0783
375	6.45	1.6932	80	0.21	35.5462
425	6.51	1.6931	60	0.14	35.6481
475	6.57	1.6927	60	0.13	35.7201
500	6.62	1.6922	50	0.1	35.9675

from 425 to 475 mg/dL and from 475 to 500 mg/dL, respectively.

A linear curve fitting using the least squares criterion is applied to the glucose concentration from 75 to 425 mg/dL, and the results are plotted in Fig. 20. As noticed, the linear curve best fits the reading data in Table 5 over the glucose range of 75 to 425 mg/dL. The slope of the linear curve in Fig. 20 is equal to the average frequency shift resulting from the glucose concentration variation. This could be used as a measure of how sensitive the proposed sensor is to glucose concentration. The slope we obtained is about 2.4 MHz/(mg/dL), which is better than what is reported in [39], where the slope was 1.34 MHz/(mg/dl). In Table 6, a comparison of the sensitivity of our work with the work published in the literature is presented, as seen in the work of [39]. A CPW planar antenna is designed to work at a resonant frequency of 1.8 GHz and the glucose concentration is varying from 0 to 16000 mg/dL. However, the test is conducted at only 98 to 188 mg/dL to calculate the sensitivity of the given design. The corresponding frequency shift is only 31.2 MHz. Ref. [31] proposed a new dielectric resonator antenna for measuring glucose concentrations at a center frequency of 4.7 GHz, and the measuring sample of the glucose concentration varies from 0 mg/dL up to 16000 mg/dL. The frequency shift is 2.81 kHz, and the sensitivity is only 2 kHz per mg/dL. At a frequency of 5.41 GHz, a microfluidic biosensor is described in [40] to monitor glucose levels from 0 to 8000 mg/dL. The sensitivity obtained in this study is only 0.1 MHz per mg/dL. Ref. [41] describes a unique split ring resonator for monitoring glucose concentration. In this work, the frequency shift is 5 kHz, and the sensitivity is 3.287 kHz per mmol/L over the tested sample in the range of 4.4–7.6 mmol/L. The sensitivity is only 3.287 kHz per mmol/L. In [42] a novel split ring resonator for measuring glucose concentration is presented. The tested range

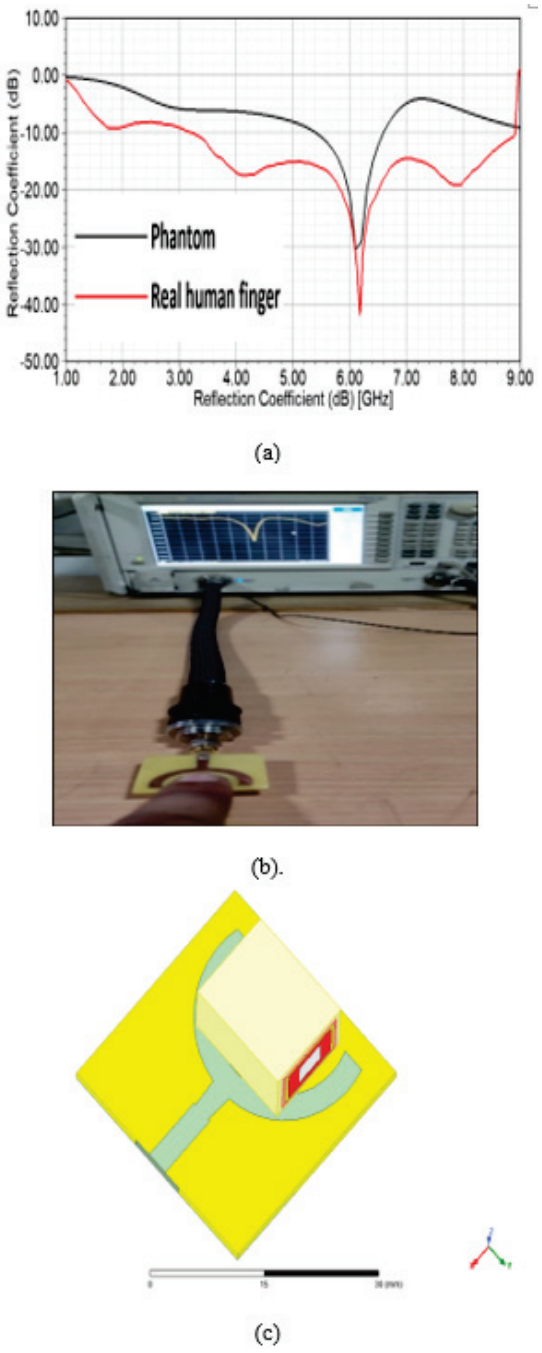

Fig. 19. (a) Measurement and simulation of the reflection coefficient by placing the real human finger and the phantom on the center of radiating element as in (b and c).

was from 2.7 to 22.2 mmol/L. Now, if we compare all these results with our proposed antenna sensor, we find that the maximum frequency shift we obtained is 800 MHz and the sensitivity is 2.4 MHz/mg/dL. This makes the proposed antenna sensor outperforms the others in detecting the changes in glucose concentration levels.

Table 6: Performance comparison of proposed antenna with literature

Reference	Technology	Operating Frequency (GHz)	Frequency Shift	Sensitivity	Measuring Sample
[39]	Non-Invasive Planar resonator	1.8	31.2 MHz	1.34 MHz/mg/dL (Tested sample 98 – 188 mg/dL)	0 – 16000 (mg/dL)
[31]	Non-invasive finger placed on Dielectric Resonator	4.7	2.81 KHz	0.002 MHz/ mg/dL	0 – 16000 (mg/dL) (glucose variation in blood sample)
[40]	Invasive method by extracting fluids	5.41	62.5 KHz	0.1 MHz/mg/dL	0-8000 (mg/dL) (glucose variation in microfluidic sample)
[41]	Non-invasive double split ring resonator	1.4	5 KHz	3.287 kHz per mmol/L	4.4 – 7.6 mmol /L (glucose variation in microfluidic sample)
[42]	Split ring biosensor	2-5	-	82 MHz/mg/mL	Glucose concentration in blood from 2.7 to 22.2 mmol/L within the range from 2.85 to 3.95 GHz
This work	Microstrip antenna sensor	6.1	800 MHz	2.4 MHz/mg/dL (Tested sample 75 – 425 mg/dL)	Glucose concentration in blood from 0-500 mg/dL

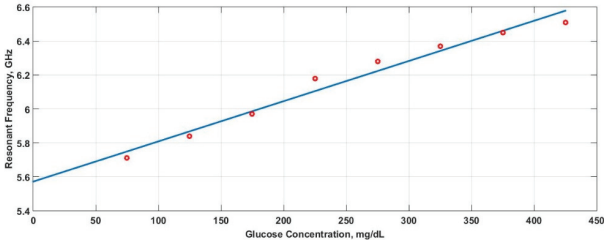

Fig. 20. Resonance frequencies Vs. Blood glucose concentration (Red circles); Fitted curve obtained by Least-square method (Blue line).

IV. CONCLUSION

A planar microstrip patch antenna that operates at 6.1 GHz and exhibits a directional radiation pattern with a peak realized gain of 3.3 dBi is designed to measure the glucose concentration in the blood. A finger phantom model of five layers: skin, fat, muscle, blood, and bone, with different dielectric constants and thicknesses, is constructed using the EM simulation (HFSS) environment. The dielectric constant of the blood is as varied as the sugar in the blood. This phantom model is placed at various locations of the radiating element of the antenna, and the frequency shifts are measured as a result of the phantom position and the variations in the glucose concentration from 0 to 500 mg/dL. The simulated results show that the best frequency shifts are obtained when the finger phantom is placed at the top of the radiating element of the antenna. The experiment was conducted on a real human finger using the designed and fabricated antenna prototype, which also presents a good agreement with the simulation results of the proposed phantom model. This shows that the proposed phantom model resembles the real human finger to a great extent, and the proposed antenna sensor is a good choice for monitoring the glucose concentrations in the blood due to its compactness, good sensitivity, and affordable cost.

ACKNOWLEDGMENT

This work was funded by the Deanship of Scientific Research (DSR) at King Abdulaziz University, Jeddah under grant No. RG-98-135-42.

REFERENCES

[1] F. Maryam, “Diagnosis of neuropathy and risk factors for corneal nerve loss in type 1 and type 2 diabetes: a corneal confocal microscopy study,” *Diabetes Care*, vol. 44, no. 1, pp. 150-156, 2021.

[2] K. E. Hill, J. M. Gleadle, M. Pulvirenti, and D. A. McNaughton, "The social determinants of health for people with type 1 diabetes that progress to end-stage renal disease," *Health Expectations*, vol. 18, no. 6, pp. 2513-2521, 2015.

[3] W. Villena Gonzales, A. Mobashsher, and A. Abbosh, "The progress of glucose monitoring—A review of invasive to minimally and non-invasive techniques, devices and sensors," *Sensors*, vol. 19, no. 4, pp. 800, 2019.

[4] C. G. Juan, E. Bronchalo, B. Potelon, C. Quendo, E. Ávila-Navarro, and J. M. Sabater-Navarro, "Concentration measurement of microliter-volume water–glucose solutions using Q factor of microwave sensors," *IEEE Transactions on Instrumentation and Measurement*, vol. 68, no. 7, pp. 2621-2634, 2019.

[5] M., Esraa, A. Ahmed, and A. Adel B, "A novel approach to non-invasive blood glucose sensing based on a defected ground structure," *15th European Conference on Antennas and Propagation* (EuCAP), pp. 1-5, Düsseldorf, Germany, March 2021.

[6] A. S. N. Shahidah and R. Alias, "A portable non-invasive blood glucose monitoring device with IoT," *Evolution in Electrical and Electronic Engineering*, vol. 2, no. 1, pp. 36-44, 2021.

[7] S. George, "Non-invasive monitoring of glucose level changes utilizing a mm-wave radar system," *International Journal of Mobile Human Computer Interaction (IJMHCI)*, vol. 10, no. 3, pp. 10-29, 2018.

[8] A. N. A. Binti, B. Saad, and W.H. Manap, "The evolution of non-invasive blood glucose monitoring system for personal application," *Journal of Telecommunication, Electronic and Computer Engineering (JTEC)*, vol. 8, no. 1, pp. 59-65, 2016.

[9] J. Yadav, A. Rani, V. Singh, and B. M. Murari, "Prospects and limitations of non-invasive blood glucose monitoring using near-infrared spectroscopy," *Biomedical Signal Processing and Control*, vol. 18, pp. 214-227, 2015.

[10] A. Paredes, V. García, I. Guzmán, J. Negrete, R. Valencia, and G. Silverio, "An IoT-based non-invasive glucose level monitoring system using raspberry pi," *Applied Sciences*, vol. 9, pp. 3046, 2019.

[11] M. S. Mohamed, M. F. O. Hameed, N. F. F. Areed, M. M. El-Okr, and S. S. A. Obayya, "Analysis of highly sensitive photonic crystal biosensor for glucose monitoring," *American Computational Electromagnetics Society (ACES) Journal*, vol. 31, no. 07, pp. 836-842. 2021.

[12] D. Vijay and S. Chorage, "Non-invasive determination of blood glucose level using narrowband microwave sensor," *Journal of Ambient Intelligence and Humanized Computing*, pp. 1-16, 2021.

[13] L. Malena, O. Fiser, P. Stauffer, T. Drizdal, J. Vrba, and D. Vrba, "Feasibility evaluation of metamaterial microwave sensors for non-invasive blood glucose monitoring," *Sensors,* pp. 21-20 2021.

[14] S. Kushal and S. Anand, "Demonstration of microstrip sensor for the feasibility study of non-invasive blood-glucose sensing," *MAPAN*, vol. 36, no. 1, pp. 193-199, 2021.

[15] V. V. Deshmukh and R. B. Ghongade, "Measurement of dielectric properties of aqueous glucose using planar ring resonator," *IEEE International Conference on Microelectronics, Computing and Communications* (MicroCom), pp. 1-5, 23-25, Durgapur, India, 2016.

[16] C. G. Helena, I. Gouzouasis, I. Sotiriou, and S. Saha, "Reflection and transmission measurements using 60 GHz patch antennas in the presence of animal tissue for non-invasive glucose sensing," *2016 10th European Conference on Antennas and Propagation* (EuCAP), pp. 10-15, Davos, Switzerland, 2016.

[17] L. W. Liu, A. Kandwal, Q. Cheng, H. Shi, I. Tobore, and Z. Nie, "Non-invasive blood glucose monitoring using a curved Goubau line," *Electronics*, vol. 8, no. 6, pp. 662, 2019.

[18] T. Karacolak, E. C. Moreland, and E. Topsakal, "Cole–cole model for glucose-dependent dielectric properties of blood plasma for continuous glucose monitoring," *Microwave and Optical Technology Letters*, vol. 55, no. 5 pp. 1160-1164, 2013.

[19] S. S. Gupta, T. H. Kwon, S. Hossain, and K. D. Kim, "Towards non-invasive blood glucose measurement using machine learning: An all-purpose PPG system design," *Biomedical Signal Processing and Control*, vol. 68, 2021.

[20] F. Jiang, S. Li, Y. Yu, Q. S. Cheng, and S. Koziel, "Sensitivity optimization of antenna for non-invasive blood glucose monitoring," *International Applied Computational Electromagnetics Society (ACES) Symposium*, pp. 1-2, 2017.

[21] J. Li, I. Tobore, Y. Liu, and A. Kandwal, "Non-invasive monitoring of three glucose ranges based on ECG by using DBSCAN-CNN," *IEEE Journal of Biomedical and Health Informatics*, vol. 25, no. 9, pp. 3440-3350, 2021.

[22] I. M. Atzeni, S. C. van de Zande, J. Westra, J. Zwerver, A. J. Smit, and D. J. Mulder, "The AGE reader: A non-invasive method to assess long-term

tissue damage," *Methods*, vol. 203, pp. 533-541, 2022.

[23] A. Zainul and P. Agarwal, "Microwave sensing technique-based label-free and real-time planar glucose analyzer fabricated on FR4," *Sensors and Actuators A: Physical*, vol. 279, pp. 132-139, 2018.

[24] M. Alam, S. Saha, P. Saha, F. N. Nur, and N. N. Moon, "D-care: A non-invasive glucose measuring technique for monitoring diabetes patients," *Proceedings of International Joint Conference on Computational Intelligence*, Springer, Singapore, July 2019.

[25] E. Susana, K. Ramli, H. Murfi, and N. H. Apriantoro, "Non-invasive classification of blood glucose level for early detection diabetes based on photoplethysmography signal," *Information*, vol. 13, no. 2, pp. 59, 2022.

[26] J. Vrba, D. Vrba, L. Díaz, and O. Fišer, "Phantoms for development of microwave sensors for noninvasive blood glucose monitoring," *International Journal of Antennas and Propagation*, 2015.

[27] T. Yilmaz, T. Ozturk, and S. Joof, "A comparative study for development of microwave glucose sensors," *Proceedings of the 32nd URSI GASS*, Montreal, QC, Canada, pp. 19-26, 2017.

[28] S. Kim, H. Melikyan, J. Kim, A. Babajanyan, and J. H. Lee, "Noninvasive in vitro measurement of pig-blood d-glucose by using a microwave cavity sensor." *Diabetes Research and Clinical Practice* vol. 96, no. 3, pp. 379-384, 2012.

[29] J. Vrba, D. Vrba, L. Díaz, and O Fišer "Metamaterial sensor for microwave non-invasive blood glucose monitoring," *IFMBE Proceedings*, vol. 68, pp. 789-792, 2019.

[30] A. N. Khan, Y. Cha, H. Giddens, and Y. Hao, "Recent advances in organ specific wireless bioelectronic devices: Perspective on biotelemetry and power transfer using antenna systems," *Engineering*, vol. 11, pp. 27-41, 2022.

[31] M. N. Hasan, S. Tamanna, P. Singh, M. D. Nadeem, and M. Rudramuni, "Cylindrical dielectric resonator antenna sensor for non-invasive glucose sensing application," *6th International Conference on Signal Processing and Integrated Networks (SPIN)*, pp. 961-964, 7-8, Noida, India, March 2019.

[32] D. Bamgboje, I. Christoulakis, I. Smanis, and G Chavan, "Continuous non-invasive glucose monitoring via contact lenses: current approaches and future perspectives," *Biosensors*, vol. 11, no. 6, pp. 189, 2021.

[33] U. Hassan, M. H. Zulfiqar, M. M. Ur Rahman, and K. Riaz, "Low Cost and Flexible Sensor System for Non-Invasive Glucose In-Situ Measurement," *17th International Bhurban Conference on Applied Sciences and Technology (IBCAST)*, pp. 187-190, 14-18, Islamabad, Pakistan, Jan. 2020.

[34] Y. Chen, F. Kaburcuk, R. Lumnitzer, A. Z. Elsherbeni, V. Demir, and A. Shamim, "Human Tissues Parameters and Resolution for Accurate Simulations of Wearable Antennas," *International Applied Computational Electromagnetics Society (ACES) Symposium* , pp. 1-4, 1-5 Aug. 2021.

[35] "An Internet Resource for the Calculation of the Dielectric Properties of Body Tissues in the Frequency Range 10Hz-100GHz," *Italian National Research Council, Institute for Applied Physics*. http://niremf.ifac.cnr.it/tissprop/

[36] F. Kaburcuk, A. Z. Elsherbeni, R. Lumnitzer, and A. Tanner, "Electromagnetic waves interaction with a human head model for frequencies up to 100 GHz," *American Computational Electromagnetics Society (ACES) Journal*, vol. 35, no. 6, pp. 613-621, 2020.

[37] C. Palmer, "Advanced devices ease burden of glucose monitoring for diabetics," *Engineering*, Elsevier, vol. 5, pp. 547-549, 2021.

[38] A. E. Omer, G. Shaker, S. Safavi-Naeini, G. Alquié, F. Deshours, H. Kokabi, and R. M. Shubair, "Noninvasive real-time monitoring of glucose level using novel microwave biosensor based on triple-pole CSRR," *IEEE Transactions on Biomedical Circuits and Systems,* vol. 14, no. 6, pp. 1407-1420, 2020.

[39] A. Ayesha, T. Kalsoom, M. Ur-Rehman, N. Ramzan, S. Karim, and Q. H. Abbasi, "Design and study of a small implantable antenna design for blood glucose monitoring," *Applied Computational Electromagnetics Society (ACES) Journal*, vol. 33, no. 10, pp. 1146-1151, 2018.

[40] M. C. Cebedio, L. A. Rabioglio, I. E. Gelosi, R. A. Ribas, A. J. Uriz, and J. C. Moreira, "Analysis and design of a microwave coplanar sensor for non-invasive blood glucose measurements," *IEEE Sensors Journal*, vol. 20, no. 18, pp. 10572-10581, 2020.

[41] D. Mondal, N. K. Tiwari, and M. J. Akhtar, "Microwave assisted non-invasive microfluidic biosensor for monitoring glucose concentration," *IEEE Sensors*, pp. 1-4, 2018.

[42] H. Choi, J. Naylon, S. Luzio, J. Beutler, J. Birchall, C. Martin, and A. Porch, "Design and in vitro interference test of microwave noninvasive blood glucose monitoring sensor," *IEEE Transactions on Microwave Theory and Techniques*, vol. 63, no. 10, pp. 3016-3025, 2015.

[43] A. Kandwal, T. Igbe, J. Li, Y. Liu, S. Li, L. W. Y. Liu, and Z. Nie, "Highly sensitive closed loop enclosed split ring biosensor with high

field confinement for aqueous and blood-glucose measurements," *Scientific Reports,* vol. 10, no. 1 pp. 1-9, 2020.

Ayman R. Megdad received his B.Sc. degree in Communication Engineering from Prince Sultan University, Saudi Arabia, Riyadh in 2016. He is presently an M.Sc. Student at King Abdul Aziz University, Saudi Arabia, Jeddah. His research interests include passive microwave/millimeter-wave circuit design, antenna design, wireless, and radar.

Rabah W. Aldhaheri received his Ph.D. degree from Michigan State University in 1988 in Electrical and Computer Engineering. He is currently a Full Professor in the Department of Electrical and Computer Engineering, at King Abdulaziz University (KAU), Jeddah, Saudi Arabia. He served as the Head of the Department of Electrical and Computer Engineering at KAU from May 2005 till May 2011. He is currently serving as the Founder and Director of the Microelectronics and RF Circuits Laboratory, FSS and Metamaterial Research Laboratory, and the Head of the Communication Systems and Networks Research Group. Aldhaheri held Visiting Research Scholar positions with Michigan State University from 1994- 1995, and Queensland University of Technology (QUT) in Brisbane, Australia in 2000. His research interests include digital signal processing with application to filter design, biometric recognition, microelectronics devices; and wireless communications, particularly, antenna design for UWB communication, medical imaging, RFID readers, and Frequency Selective Surfaces (FSS).

Nebras M. Sobahi (Member, IEEE) received the B.Sc. and M.Sc. degrees in electrical engineering from King Abdulaziz University, and the second M.Sc. and Ph.D. degrees in electrical engineering from Texas A&M University, USA. He is currently an Assistant Professor at the Department of Electrical and Computer Engineering, King Abdulaziz University, Saudi Arabia. His research interests include nano/microfabrication, MEMS, microfluidics, BioMEMS, and signal and image processing.

Non-Destructive Detection of Pipe Line Cracks Using Ultra Wide Band Antenna with Machine Learning Algorithm

B. Ananda Venkatesan and K. Kalimuthu

Department of Electronics and Communication Engineering
SRM IST, Kattankulathur, Chennai-603203, India
anandavenkatesan@gmail.com, kalimutk@srmist.edu.in

Abstract – In this article, an Ultra-Wide Band (UWB) antenna for the pipeline crack detection process is proposed. A UWB antenna has been designed with the dimension of 32 x 32 mm^2 and it resonates from 3 GHz to 10.8 GHz. The designed antenna produces a peak gain of 4.36 dB. A pair of UWB antennas are employed in various pipeline scenarios and the received pulse from antenna 1 to antenna 2 is used for further processing and detection of pipeline cracks. Through the suitable machine learning data classifier algorithm the dimension of the crack has been detected. The various features such as mean, standard deviation (σ), mean average deviation (mad), skewness, and kurtosis have been extracted from the received pulse. Then the three different machine learning algorithms namely Support Vector Machine (SVM), k-Nearest Neighbor (kNN), and Naïve Bayse (NB) were trained and tested using extracted features, and the dimension of the void has been identified. Out of these three machine learning algorithms, kNN provides better accuracy and precision. It predicts the small cracks with 100% accuracy having a dimension as small as 1 mm width.

Index Terms – crack detection, machine learning, pulse characteristics, UWB antenna.

I. INTRODUCTION

For most infrastructure projects metallic structure plays an important role. Excessive loading and rough environmental conditions may lead to the formation of cracks. Crack sensing is an important process in structural health monitoring that may cause mechanical failure. In the United States, water, petroleum, and natural gas are carried by buried pipelines that run approximately 11 million miles. It is accepted that there is a significant increase in the rate of failure over the 40 years. For the next 25 years, 40 trillion dollars are required to improve the road and water facilities. A report submitted by Battelle Memorial Institute estimates that 4.5 billion dollars are needed for water supply rehabilitation projects with an annual growth rate of 8-10% [1]. Triple band microstrip patch antenna has been proposed for crack detection. The resonant frequency of each band is shifted due to variations in the impedance of the antenna when the crack is present in the ground plane [2].

A compact Antipodal Vivaldi antenna designed to operate at 1 to 3 GHz is used for non-destructive testing and assessment of construction materials such as concrete and dielectric composite materials[3]. In microwave imaging, the target is subjected to an electromagnetic wave and the reflected signal is processed to reconstruct the image of the object. To detect the flaws in construction material, it is necessary to have an antenna with a high depth of penetration and high resolution. High depth of penetration is possible at relatively low frequency (1-3 GHz) and resolution is achieved using larger bandwidth [4].

The circular-shaped RFID antenna is reported for structural health monitoring. The shift in the resonant frequency is used as an important feature to detect and characterize the crack on the metallic surface. In the process of structural health monitoring, early detection of cracks is an important and challenging task. Some of the existing techniques are using of strain gauges, fiber optic sensors, and ultrasonic sensors. The disadvantage of these methods is the need for a data acquisition system, more skilled technicians, high material cost, and difficulty to deploy. These difficulties can be overcome by using sensor-based tag antennas operating in ultrahigh-frequency (UHF) regions. The formation of cracks or deformation in the structure is detected by continuously monitoring the resonant frequency of the antenna sensor [5]. An open-ended waveguide is used for surface crack detection. When the waveguide is probed over the metal surface, it acts as a short circuit in the absence of a crack. If a crack exists then the reflection characteristics of the waveguide are altered which in turn will bring the changes in the standing wave characteristics of the wave that can be probed with the aid of a diode detector. The sensitivity of this technique is relatively low and can be improved by increasing the operating frequency this

Submitted On: August 7, 2022
Accepted On: December 15, 2022

https://doi.org/10.13052/2022.ACES.J.371103

may lead to highly increased complexity and cost of the measuring setup [6].

The cracks in the metal surface are detected with the help of dual characteristics resonator filters in the near field region. It will produce a 50 MHz shift in the resonant Frequency for 200 μm. This method has low resolution and a need to analyze the transmission coefficient (S_{21}) for a wide range of frequencies which increases the difficulty in measurement [7]. A microstrip line excited complementary split ring resonator is used for crack detection in metallic surfaces. This method has relatively high sensitivity and can detect surface cracks as small as 100 μm in length with a shift of approximately 240 MHz [8]. A microwave ring resonator that operates at 2.5 GHz is utilized for the detection of breaches in pipeline coatings. Any defect in the pipeline coating may cause a variation in the resonant frequency and bandwidth of the sensor. Failure in the detection of these defects or breaches in the early stage may lead to the spreading of cracks [9]. High sensitivity complementary split ring resonator-based sensor has been presented. This technique has advantages like spatial resolution, high sensitivity, and scalability. It can able to detect surface cracks of length 10μm with a shift of 200MHz. The behavior of materials to EM waves is based on three parameters conductivity (σ), permittivity ($\varepsilon_{r)}$, and permeability ($\mu_{r)}$. The interaction between EM waves and materials has been investigated for the detection and characterization of cracks [10]. Time domain computation has been proved as a useful tool for characterizing the electrical properties of various materials over a wide range of frequencies [11]. Ultra-wideband technology produces very narrow pulses in the order of nanoseconds [12, 13]. Due to its shorter duration high resolution and precision can be achieved in the crack detection process. This high resolution is possible even through the lossy media such as soil, foliage, wall, and floor of buildings [14].

This method examines the theoretical importance [15] of ultra-wideband signals for surface crack detection as a non-destructive testing (NDT) technique in the frequency domain (FD). The conventional frequency domain analysis of UWB signals involves the investigation of individual frequency components to cover a wide range of frequencies. This makes the NDT technique a complex and time-consuming process. An alternate approach to solve this problem is the Time Domain (TD) method in which field distribution is assumed as a general function of time [16]. The notable advantage of the TD method is its applicability to a wide range of frequencies and the ability to detect the small defects in the specimen by observing the changes in the received signals. UWB non-destructive testing is widely used to estimate the dielectric constant of the material, in the industry to detect the surface crack and to detect abnormalities in the human body in biomedicine. In the NDT technique, the metal surface is exposed to an electromagnetic field and the reflected signal is analyzed with the help of a vector network analyzer. If the crack is present on the surface of the metal, then the scattering behavior of the EM field will change in nature and this property is utilized for surface crack detection [17]. A non-symmetric circular patch antenna operating at 2.45 GHz is used to identify human ethnicity. The extracted features from the return loss are used to find the ethnicity of the human with the aid of a machine learning algorithm [18].

Ultra-Wide Band technology has some unique characteristics such as being capable to generate short pulses having nanoseconds duration, broad frequency range, and high fidelity. This makes UWB antennas a suitable candidate for various real-time applications such as medical diagnosis, ground penetration radar (GPR), detection of unexploded land mines, intrusion/suspicious detection, and identification of cracks in buildings, highway lanes, and bridges [19]. A UWB antenna has been used as the sensor to detect the discharges from the high-voltage machinery. In industries, it is necessary to monitor the partial discharge (PD) from the high voltage equipment for smooth operation. A UWB antenna operates from 1.1 to 4.5 GHz and has been used to detect PD efficiently [20].

This research article is divided into five sections. Section 1 describes Introduction of the work, antenna design is discussed in Section 2, testing procedure is explained in Section 3, detection process is elaborated in Section 4 and conclusion is given in the 5th section.

II. ANTENNA DESIGN

The final design of a UWB antenna has been obtained after three stages of evolution as shown in Fig. 1. In the first stage (Fig. 2 (a)), a planar antenna has been constructed on an FR4 substrate with a rectangular-shaped radiator and partial ground plane. This design does not produce any resonance in the required frequency band. In the next stage (Fig. 2 (b)), two square slits are made on the bottom edges of the rectangular radiator. In this stage, the antenna resonates from 3.2 GHz to 10.7 GHz. In the final stage (Fig. 2 (c)), two triangular portions are etched out from the ground plane and a slit of dimension 1 x1 mm^2 has been introduced in the center of the ground plane, thereby capacitance between the ground plane and radiator has been decreased; the antenna resonates from 3 GHz to 10.8 GHz [21].

The reflection coefficient characteristics for various stages of evolution are depicted in Fig. 3. In stage 3 the antenna reflection coefficient characteristics are less than -10dB for the entire band from 3 to 10.8 GHz.

Figure 4 shows the simulated and measured reflection coefficient characteristics of the proposed UWB

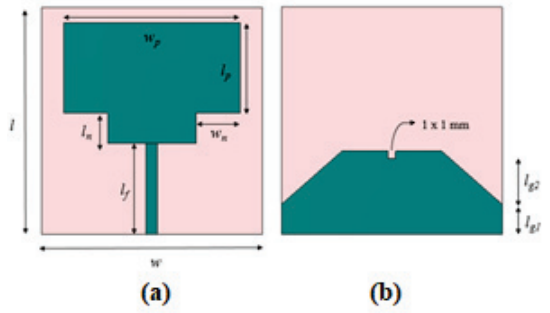

l = 30mm, w= 30mm, l_f =12mm, l_n = 4mm, w_n =6mm, l_p = 14mm, w_p = 24mm, l_{g1} =4mm, l_{g2} = 7mm

Fig. 1. Schematic diagram of UWB antenna. (a) Front view. (b) Rear view.

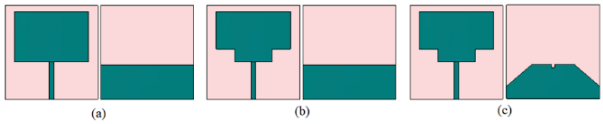

Fig. 2. Evolution stages of UWB Antenna. (a) Stage 1. (b) Stage 2. (c) Stage 3.

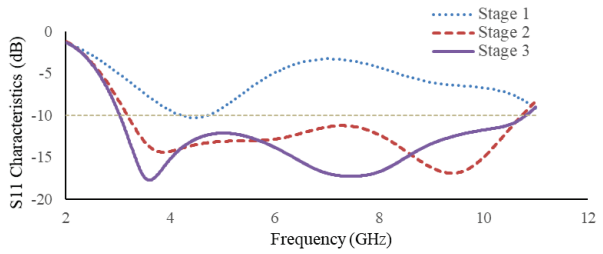

Fig. 3. Reflection coefficient (S_{11}) characteristics of various Stages of evolution.

antenna. From the figure, it is clear that the measured result well agrees with the simulated values.

The real and imaginary impedance characteristics of the antenna are plotted in Fig. 5. In the operating

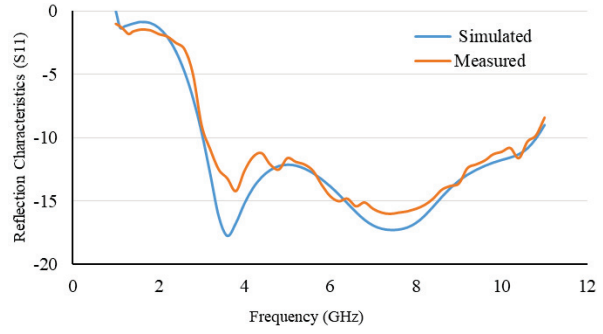

Fig. 4. Simulated and Measured Reflection Coefficient (S_{11}) Characteristics.

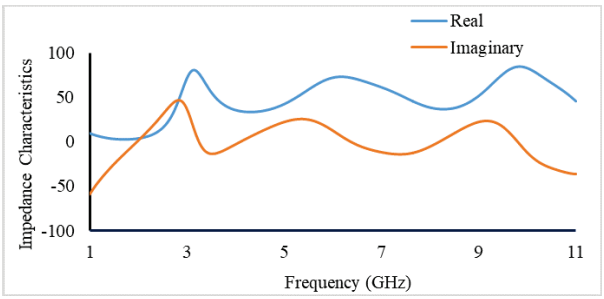

Fig. 5. Real and imaginary impedance characteristics.

frequency band (3-10.8 GHz), the real impedance slightly oscillates around 50 ohms and the imaginary impedance varies around zero ohms.

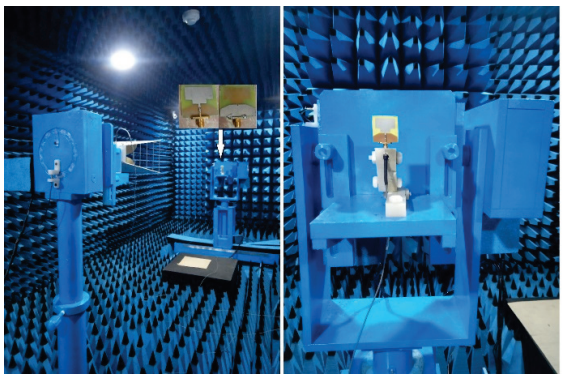

Fig. 6. Radiation pattern measurement in anechoic chamber.

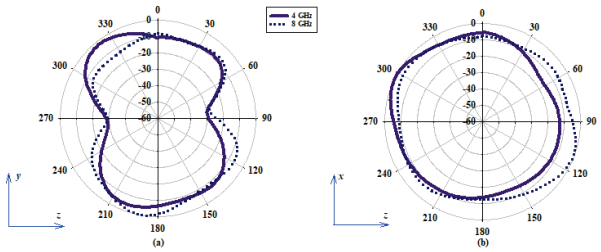

Fig. 7. Measured radiation pattern of the UWB Antenna. (a) E-field pattern, φ = 90°. (b) Ant1 H-field pattern, φ = 0°.

The radiation pattern of the fabricated antenna is measured in an anechoic chamber as shown in Fig. 6. Fig. 7 depicts the E-plane and H-plane, radiation characteristics of an antenna at 4 and 8 GHz.

III. TESTING PROCEUDRE

The pipeline structure has been constructed [22] using a dielectric (Taconic) material which is having permittivity (ε_r=4) almost equal to the permittivity of Poly

Vinyl Chloride (PVC). The pipe has been loaded with distilled water. Then the pair of UWB antennas have been used in a face-to-face configuration for collecting the time domain pulses from antenna 1 to antenna 2. The amplitude variation and distribution of the collected pulses have been utilized for the detection of cracks in the pipe [23]. The various key metrics such as mean, standard deviation, mean average deviation, skewness and kurtosis have been calculated for the obtained pulses for the identification and characterization of the cracks. Then the three different machine learning algorithms, such as the Support Vector Machine (SVM), k-Nearest Neighbours (kNN), and Naïve Bayes (NB) algorithms, have been used as data classification algorithms for detecting the presence of the cracks and predicting the width of the crack.

A. Feature extraction

The various key features such as the mean, standard deviation, mean average deviation, skewness, and kurtosis have been extracted from the short-duration time domain pulses and it has been used for testing and training the machine learning algorithms. These features possess information about the shape and amplitude of the pulse. The amplitude and shape of the pulse are a pure function of the permittivity of the medium through which it propagates. Because the permittivity of the medium only decides the group delay (τ) and amount of signal absorption.

The Mean Absolute Deviation represents the distribution of the data set around the mean value. The lower value of MAD indicates that the data points are close to the mean value. It gives information about the volatility in a dataset:

$$MAD = \frac{\sum |x_i - \overline{x}|}{n}, \tag{1}$$

where $x_i$is the ith data point, $\bar{x}$ is the mean of all data point, and n is the total number of data point.

Skewness is a measure of the symmetry of data distribution. Negative skewness indicates, the data distribution is longer on the left side than on the right:

$$\overline{\mu_3} = \frac{\sum_{i=1}^{n}(x_i - \bar{x})^3}{(N-1)\sigma^3}, \tag{2}$$

where, $\overline{\mu_3}$ is the Skewness, N is the total number of data points in the distribution, $x_i$is the ith data point, and $\bar{x}$ is the mean of all data point.

Kurtosis is a statistical estimation of how data is distributed in the tail of the curve. If the kurtosis value is positive, means that data is distributed heavily on the tail side.

B. Machine learning algorithm

SVM is a supervised data classifier algorithm that can able to solve linear and non-linear data sets, and predicts the class of particular data. Another supervised machine learning algorithm called kNN is a non-parametric and lazy learning algorithm, which predicts the class of data points by looking at the neighboring data points. The Naïve Bayes algorithm is a probabilistic machine learning data classifier that works on the principle of Bayes probability theory. The short-time duration pulses for different pipeline environments have been collected by placing a pair of UWB antennas at certain distances with specific separation between the antennas.

The received pulse characteristics for various pipeline environments have been categorized into two groups. One set of data is used for training the data classifier algorithm and another set of data is used for testing and validation.

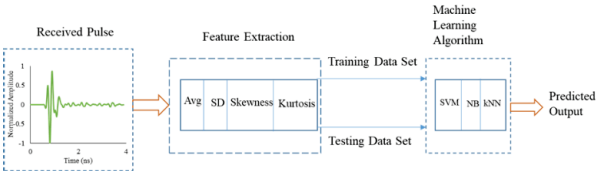

Fig. 8. Proposed pipeline crack detection machine learning system model.

IV. DETECTION PROCESS

The distance between the pipeline and the Antenna is referred to as "d" and the separation between the antennas is referred to as "l" as shown in Fig. 9. The distance (d) is set as 30mm and 60mm, two sets of pulse characteristics are taken. The separation (l) is varied as 40mm, 60mm, and 80mm, and three sets of received pulse characteristics are simulated. So, a total of six sets of readings are taken for one type of configuration (No crack, 1 mm, 2 mm, 5 mm, and 10mm cracks).

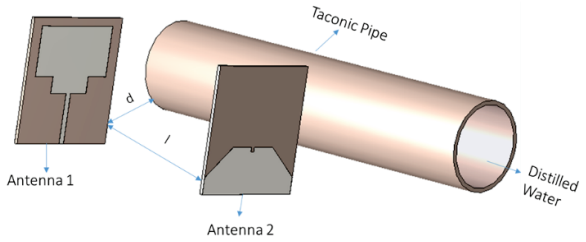

Fig. 9. Face-to-face configuration of UWB antenna in the pipeline environment without crack.

While generating the time domain pulse characteristics the length of the crack is fixed as 10mm and the width is varied as 1mm, 2mm, 5mm, and 10mm as illustrated in Fig. 10. The time domain pulses are generated for different distances (d), separations (l) and various

crack lengths have been classified into two groups of data. One set of data is used for training the classifier (SVM, kNN, Naïve Bayes) and the other set of data is used for testing and validating the correctness of the prediction.

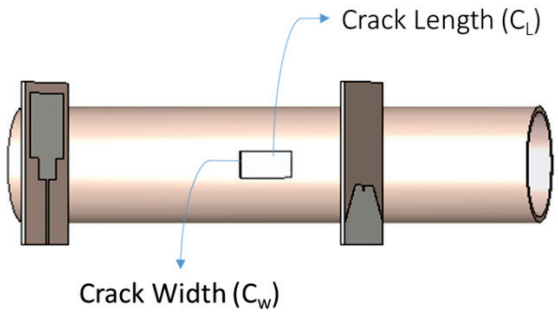

Fig. 10. Face-to-face configuration of UWB antenna in the pipeline environment without crack.

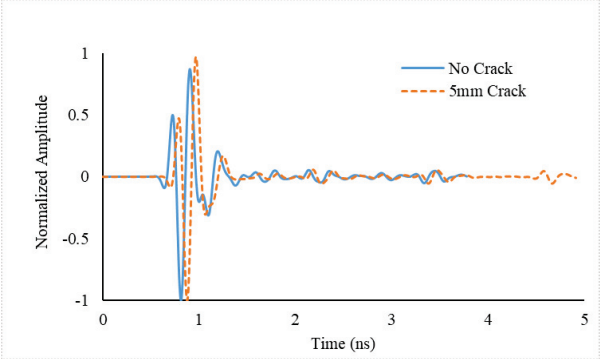

Fig. 11. Received pulse characteristics of a pipeline with no crack and with a 5 mm crack.

The high spatial resolution property of the UWB signal is utilized for identifying the presence of the crack and classification of the crack width. A pair of UWB antennas are operated in various pipeline environments such as pipe without void and pipe with various void dimensions. Two antennas are placed on either side of the crack and the change in the pulse characteristics has been analyzed. The shape and amplitude of the pulse are highly dependent on the permittivity of the medium through which it propagates. If the void is present in the pipeline then the characteristics of the EM wave traveling path change, which in turn influences the shape and amplitude of the UWB pulse. The level of variation in the signal amplitude is a function of the dimension of the void as shown in Fig. 11.

$$\lceil = \frac{Z - Zo}{Z + Zo} = \frac{\sqrt{\left(\frac{\mu r}{\varepsilon r}\right)} - 1}{\sqrt{\left(\frac{\mu r}{\varepsilon r}\right)} + 1}, \tag{3}$$

where Z= exp (-jω $\sqrt{}$ ($\mu_r \varepsilon_r$) d).

The time domain pulse amplitudes are labeled with unique numbers for reference. No crack, 1mm, 2mm, 5mm, and 10mm crack group pulses are labeled as numerical from 1 to 5 respectively. The data classifier algorithms (SVM, kNN, Naïve Bayes) are trained with training data sets for various crack dimensions. Then the trained data classifier algorithms are tested with the help of a separate set of time domain pulse characteristics. The correctness of the prediction for various machine learning algorithms is compared.

Table 1: Comparison between various machine learning algorithms

Crack Width (mm)	Numerical Label	Prediction		
		SVM	k-NN	Naïve Bayse
No Crack	1	1	1	2
1 mm	2	1	2	2
2 mm	3	1	3	2
5 mm	4	4	4	4
10 mm	5	5	5	5

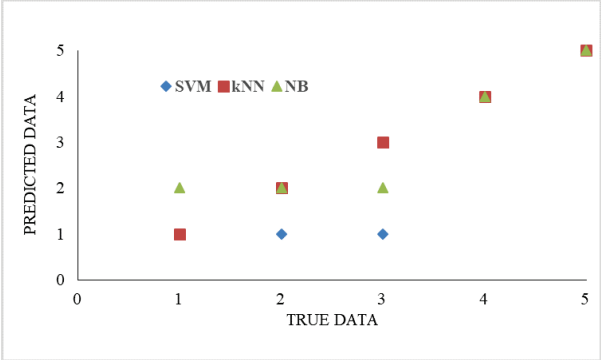

Fig. 12. Received pulse characteristics of a pipeline with no crack and with a 5 mm crack.

The proposed research finding is compared with the already presented works in Table 2 and the key merits of this work are summarized as follows:

- Pair of planar monopole UWB antennae works at 3 to 10.8 GHz and is used for crack detection in pipelines. It has a simple design, easy to fabricate, and low cost.

Table 2: Comparison of the recently reported works with the proposed technique

Ref	Antenna Type	Operating Frequency (GHz)	Dimensions (mm × mm), ($\lambda_0 \times \lambda_0$)	Parameter used for Crack Detection	Sensitivity	Requirement of Additional Processing Unit	Use of Machine Learning Algorithm
[2]	Triple Band Antenna	2.687,4.997, 9.518	40x50, 0.36x0.45	Shift in resonance frequency, Impedance Variation	Low	No	X
[3]	Antipodal Vivaldi Antenna	1to 30	96x100, 0.32x0.33	Image Construction	Moderate	Yes	
[4]	RFID Antenna	1.285	35x35, 0.15x0.15	Shift in resonance frequency	low	No	X
[5]	Wave Guide	24	—	Changes in Standing Wave Pattern	High	Yes	
[6]	Resonator Filter	8.08 to 13.557	25.4x25.4, 0.69x0.69	Shift in resonance frequency	High	No	X
[7]	Complementary Split Ring Resonator	5GHz	3x3, 0.05x0.05	Shift in resonance frequency	High	No	X
[8]	Ring Resonator	2.5	—	Shift in resonance frequency, Change in quality factor	High	No	X
[9]	Complementary Split Ring Resonator	9.8GHz	3x3, 0.1x0.1	Shift in resonance frequency	Very High	No	X
Proposed	UWB Antenna	3-10.8	32x32, 0.32x0.32	Variation in Pulse Receiving Characteristics	Moderate	No	✓

- The crack is detected by investigating the received UWB time domain pulses.
- The various key of the received pulses has been extracted, which has been used to train and test the different machine learning algorithms.
- This method does not require any additional processing unit for analyzing the data.
- The presence of crack has been detected in a non-destructive manner with the hybrid combination of UWB Antenna with a machine learning algorithm.

V. CONCLUSION

An ultra-wideband antenna that operates from 3 to 10.8 GHz has been used for pipeline crack detection. A pair of UWB antennas are used in various pipeline scenarios. One antenna is used as a transmitter and another one is used as a receiver. The time domain pulses received by the receiving antenna have been utilized for the detection and characterization of the cracks in the pipe. The shape and the amplitude of the received pulse will vary depending on the medium (permittivity ε_r) through which it propagates. For the received pulse various features such as mean, standard deviation, skewness, and kurtosis have been calculated. The three

different supervised machine learning algorithms such as SVM, kNN, and NB are used for the prediction of crack dimension. These Machine learning algorithms are trained with one set of pulse features and tested with different data set. All three algorithms can predict and differentiate cracks having a width of 5 mm. However, the kNN algorithm provides better prediction with 100% accuracy and can differentiate small cracks having a width as small as 1 mm.

REFERENCES

[1] A. Jaganathan, E. Allouche, and S. Neven, "Numerical modeling and experimental evaluation of a time domain UWB technique for soil void detection," *Tunnelling and Underground Space Technology*, vol. 25, pp. 652-659, 2010.

[2] H. Andre, P. Emeraldi, R. Fernandez, M. Muharam, Firdaus, and E. P. Waldi, "Triple band circular microstrip antenna for metallic material crack sensing," *International Conference on Applied Science and Technology*, Manado, Indonesia, pp. 373- 374, 2019.

[3] X. R. Wang, X. B. Wang, H. Ren, N. S. Wu, J. W. Wu, W. M. Su, Y. L. Han, and S. Xu "Optically transparent microwave shielding hybrid film composited by metal mesh and graphene," *Progress In Electromagnetics Research*, vol. 170, pp. 187-197, 2021.

[4] M. Moosazadeh, S. Kharkovsky, J. T. Case, and B. Samali, "Miniaturized UWB antipodal vivaldi antenna and its application for detection of void inside concrete specimens," *IEEE Antennas and Wireless Propagation Letters*, vol. 16, pp. 1317-1320, 2016.

[5] C. Wang, C. Wang, G. C. Wan, M. S. Tong, S. Guan, and L. Y. Xie, "RFID antenna sensor for quantitatively monitoring surface crack growth," *IEEE International Conference on Computational Electromagnetics (ICCEM),* Shanghai, China, pp. 1-3, 2019.

[6] C. Y. Yeh and R. Zoughi, "A novel microwave method for detection of long surface cracks in metals," *IEEE Transactions on Instrumentation and Measurement*, vol. 43, no. 5, pp. 719-725, Oct. 1994.

[7] J. Kerouedan, P. Quéffélec, P. Talbot, C. Quendo, S. De Blasi, and A. Le Brun, "Detection of micro-cracks on metal surfaces using near-field microwave dual-behavior resonator filters," *Measurement Science and Technology*, vol. 19, no. 10, 2008.

[8] A. M. Albishi, M. S. Boybay, and O. M. Ramahi, "Complementary split-ring resonator for crack detection in metallic surfaces," *IEEE Microwave and Wireless Components Letters*, vol. 22, no. 6, pp. 330-332, 2012.

[9] M. H. Zarifi, S. Deif, M. Abdolrazzaghi, B. Chen, D. Ramsawak, M. Amyotte, N. Vahabisani, Z. Hashisho, W. Chen, and M. Daneshmand, "A microwave ring resonator sensor for early detection of breaches in pipeline coatings," *IEEE Transactions on Industrial Electronics*, vol. 65, no. 2, pp. 1626-1635, 2018.

[10] A. M. Albishi and O. M. Ramahi, "Surface crack detection in metallic materials using sensitive microwave-based sensors," *IEEE 17th Annual Wireless and Microwave Technology Conference (WAMICON)*, pp. 1-3, 2016.

[11] C. L. Bennett and G. F. Ross, "Time-domain electromagnetics and its applications," *Proceedings of the IEEE*, vol. 66, no. 3, pp. 299-318, 1978, doi: 10.1109/PROC.1978.10902.

[12] S. Mohandoss, S. K. Palaniswamy, R. R. Thipparaju, M. Kanagasabai, B. R. B. Naga, and S. Kumar, "On the bending and time domain analysis of compact wideband flexible monopole antennas," *International Journal of Electronics and Communications*, vol. 101, pp. 168-181, 2019.

[13] S. R. Zahran, M. A. Abdalla, and A. Gaafar, "Time domain analysis for foldable thin UWB monopole antenna," *International Journal of Electronics and Communications*, vol. 83, pp. 253-262, 2018.

[14] Y. Rahayu, T. A. Rahman, R. Ngah, and P. S. Hall, "Ultrawide band technology and its applications," *International Conference on Wireless and Optical Communications Network*, Surbaya, pp. 1-5, 2008.

[15] M. Bozorgi and A. Tavakoli, "Polarimetric scattering from a 3-D rectangular crack in a PEC covered by a dielectric layer," *American Computation Electromagnetics Society (ACES) Journal*, vol. 26, no. 6, pp. 502-511, 2022.

[16] X. Han, H. Li, Y. Zhou, L. Wang, S. Liang, and F. Javaid "An elliptically polarized wave injection technique via TF/SF boundary in subdomain level DGTD method," *Progress in Electromagnetics Research*, vol. 175, pp. 13-27, 2022.

[17] A. Mirala and R. Sarraf Shiraz, "Detection of surface cracks in metals using time domain microwave non-destructive testing," *IET Microwaves, Antennas & Propagation*, vol. 11, pp. 564-569, 2017.

[18] W. Saadat, S. A. Raurale, G. A. Conway, and J. McAllister, "Wearable antennas for human identification at 2.45 GHz," *IEEE Transactions on Antennas and Propagation*, vol. 70, no. 1, pp. 17-26, 2022.

[19] X. He and T. Jiang, "Target identification in foliage environment using UWB radar with

hybrid wavelet-ICA and SVM Method," *Physical Communication*, vol. 1, pp. 197-204, 2014.

[20] J. P. Uwiringiyimana, U. Khayam, Suwarno, and G. C. Montanari, "Design and implementation of ultra-wide band antenna for partial discharge detection in high voltage power equipment," *IEEE Access*, vol. 10, pp. 10983-10994, 2022.

[21] E. Zhou, Y. Cheng, F. Chen, H. Luo, and X. Li, "Low-profile high-gain wideband multi-resonance microstrip-fed slot antenna with anisotropic meta surface," *Progress in Electromagnetics Research*, vol. 175, pp. 91-104, 2022.

[22] F. Jiang, S. Liu, and L. Tao, "Quantitative research on cracks in pipe based on magnetic field response method of eddy current testing," *American Computation Electromagnetics Society (ACES) Journal*, vol. 36, no. 1, pp. 99-107, 2021.

[23] F. Deek and M. E. Shenawee, "Microwave detection of cracks in buried pipes using the complex frequency technique," *American Computation Electromagnetics Society (ACES) Journal*, vol. 25, no. 10, pp. 894-902, 2010.

B. Ananda Venkatesan is currently working towards a Ph.D. degree at SRMIST, Chennai. His research interests include planar antennas, machine learning, and signal processing.

K. Kalimuthu was born in india. He has completed his Ph.D. degree in Cognitive Radio from the ECE Department of SRMIST Chennai. Currently, he is working as an Associate professor in the Department of ECE, SRMIST, Chennai. His research interests include wireless communication, antennas, signal processing, and cognitive radio networks.

Single-band Series Absorptive Common-mode Noise Filter

Ding-Bin Lin[1], Erfansyah Ali[1,2], Tjahjo Adiprabowo[1], and Cheng-Yi Zhuang[1]

[1]Department of Electronic and Computer Engineering
National Taiwan University of Science and Technology, Taipei, Taiwan
dblin@mail.ntust.edu.tw, d10902801@mail.ntust.edu.tw, d10602804@mail.ntust.edu.tw,
d10902010@mail.ntust.edu.tw

[2]Department of Telecommunication Engineering
Telkom University, Bandung, Indonesia
erfansyahali@telkomuniversity.ac.id

Abstract **–** A Single-band Series Absorptive Common Mode Noise Filter (ACMF) is proposed. The ACMF is embedded in a four-layer printed circuit board (PCB) and consists of three parts: a Reflective Common Mode Noise Filter (RCMF), a matching circuit, and an absorber. The RCMF is designed using mushroom-type resonators. The matching circuit is designed using meander lines to reduce the size of the filter dimensions. The absorber of the Common Mode noise (CM) is a series resistor. The designed operating frequency is 2.45 GHz. The simulation results are as follows: the insertion loss of CM (S_{cc21}) is −22.49 dB at the frequency of 2.61 GHz, the return loss of CM (S_{cc11}) is −18.62 dB at the frequency of 2.5 GHz, while the integrity of the Differential Mode signals (DM) can be maintained with a very small insertion loss (S_{dd21}) of −1 dB at the frequency range of 0-8 GHz, and the achieved Absorption Efficiency (AE) is 93% at the frequency of 2.54 GHz. The proposed ACMF dimension is 10.3 x4.6 mm. The fractional bandwidth is 19%. The measurement results of the fabricated ACMF do not deviate significantly the simulation results. They are as follows: S_{cc21} is −17.87 dB at the frequency of 2.31 GHz, Scc11 is −20.87 dB at the frequency of 2.38 GHz, S_{dd21} is −2.8 dB at the frequency range of 0–8 GHz, the Absorption Efficiency is 97% at the frequency of 2.32 GHz, and the fractional bandwidth is 17%. Therefore, the results of the ACMF design carried out by simulation can be implemented into a fabricated ACMF with measurement results similar to the calculation results in the design.

Index Terms **–** absorptive common-mode filter (ACMF), absorption efficiency (AE), common-mode filter (CMF).

I. INTRODUCTION

Today, high-speed data transmission is used in many electronic systems, including Universal Serial Bus (USB) and High Definition Multimedia Interface (HDMI). The signals used are Differential Mode (DM) signals because of their high immunity to noise. However, some of these DM signals can turn into Common Mode (CM) signals as a result of the time skew and asymmetrical circuit structure. The CM signals will degrade the performance of electronic devices surrounding it, as they can cause the problem of radiated Electromagnetic Interference (EMI) noises [1, 2]. Therefore, the CM signals are considered as noise which is commonly referred to as CM noise [3–5]. To overcome this, a Common Mode noise Filter (CMF) is needed which is expected to reduce the CM noise at a certain frequency needed while maintaining the integrity of the DM signals.

In the past, many types of CMFs were proposed to overcome CM noise [6–8]. One of them is the use of a ferrite core with winding lines. This results in a large input impedance for CM noise [9], while the DM signals can still pass without significant attenuation. The disadvantage is that its bandwidth at high frequencies is limited due to decreased permeability. The next type of CMF proposed is the use of mushroom-like resonators in multilayer PCBs [10]. Next, RCMFs are made of Pattern Ground Structure (PGS). This structure provides a resonator in the reference ground plane to block the flow of CM noise [11]. The above-mentioned CMFs can prevent the transmission of CM noise to the next stage, because the CM noise is reflected to the front-end circuit by the filter. As a result, interference by CM noise is still sensed by the front-end and surrounding circuits. To overcome this problem, a filter type that can absorb CM noise energy is proposed.

There are two types of CMFs, namely: Reflective Common Mode Noise Filter (RCMF) and Absorptive Common Mode Noise Filter (ACMF). RCMF reflects CM noise to circuits in the previous stage. ACMF absorbs or dampens CM noise at certain frequencies so

Submitted On: June 28, 2022
Accepted On: December 22, 2022
https://doi.org/10.13052/2022.ACES.J.371104

it does not continue to transmit to the next stages of the circuits and also does not bounce back to the previous stages of the circuits. The reflective CM noise will degrade the performance of the previous stages of the electronic circuits. Therefore, ACMF is better than RCMF. An ACMF can be made by adding absorber circuits in the form of resistive materials to an RCMF to absorb the reflected CM noise [12].

In this paper, a series ACMF is proposed. The ACMF consists of three stages. The first stage is the RCMF, the second stage is the matching circuit, and the third stage is the absorber in the form of a series resistive material. The RCMF type that is designed is a mushroom type. The matching circuit function is to bring a short circuit in the middle of the RCMF to the absorber which is located on the front port. Therefore the length of the matching circuit is half wavelength ($\lambda/2$) of the resonant frequency so that the short circuit condition reaches the absorber. The matching circuit is designed using meander lines to make the filter dimensions as small as possible. The absorber that is used is a Surface Mounted Device (SMD) resistor. The advantage of a series ACMF over another type of filter is its simpler implementation. The other type of ACMF filter is parallel ACMF. A series ACMF is implemented on a four-layer Printed Circuit Board (PCB).

An ACMF is said to be useful only if it is able to absorb as much CM noise as possible. This occurs when the insertion loss of CM (S_{cc21}) is minimum and the return loss of CM (S_{cc11}) is also minimum. This is expressed in terms of Absorption Efficiency (AE) as shown in (1) [13]. Therefore, the larger the AE the better the ACMF.

$$AE(\%) = 100 \times \left(1 - |S_{cc21}|^2 - |s_{cc11}|^2\right). \qquad (1)$$

II. PROPOSED STRUCTURE

The structure of the proposed ACMF is shown in Fig. 1. This series ACMF uses four Layers PCB with detail dimensions and materials can be seen in Fig. 2. Layer 1 is used for differential mode signal traces. Layer 2 is used for the mushroom pad and reference ground of the matching circuit. While Layer 3 is used for local ground. Layer 4 is used for system ground and the location where the serial Surface Mounted Device (SMD) Resistor is attached.

The series ACMF is shown in Fig. 3. The RCMF that we use in stage 1 is a mushroom-type RCMF. Therefore, the mushroom pad acts as an auxiliary ground for DM signals on stage 1. The mushroom pad is connected to the local ground at Layer 3 through a via and meandering path as shown in Fig. 1. This meandering path serves as an inductor that determines the resonant frequency. This is the frequency when transmission zero occurs for CM noise. The resonant frequency that we use is 2.45 GHz. This frequency was deliberately chosen according to the Wi-Fi frequency standard [14], so that our proposed ACMF can be used to secure the Wi-Fi transceiver module from the interference of CM noise.

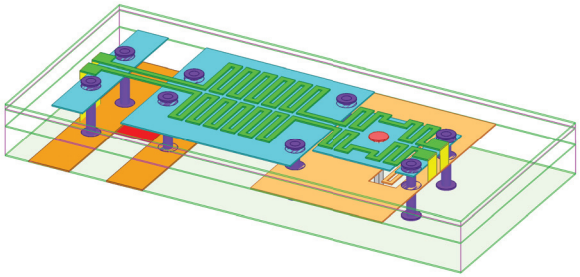

Fig. 1. The structure of proposed ACMF, trimetric view.

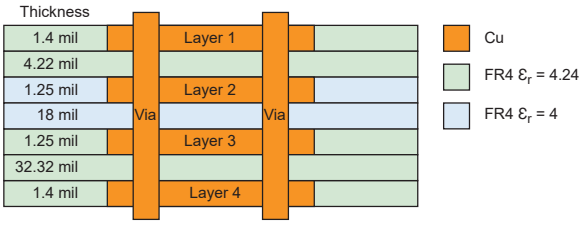

Fig. 2. PCB layers of proposed ACMF.

Transmission Zero or short circuit load occurs in the middle of the mushroom pad. The matching circuit in stage 2 has a function as a short circuit load shifter from the middle of the mushroom pad to the resistor absorber on stage 3. This is achieved by adjusting the length of the matching circuit to $\lambda/2$, where λ is the wavelength of the resonant frequency. To reduce the physical dimensions of the filter, this matching circuit is made in meander form. This results in the proposed ACMF dimensions of 10.3x4.6 mm. Thus, at stage 3, the CM noise will go through a short circuit and an absorbent resistor that is mounted serially towards the ground. This is a new concept of our research, which is to use an absorbent resistor in series rather than parallel. The advantage of this concept is its simplicity in implementation. The absorbent resistor is drawn in red as shown in Fig. 1 and Fig. 3. This is how the CM noise is dissipated into heat by an absorbent resistor that has a resistance of 25 Ω.

A. Reflective common mode noise filter (RCMF)

The first stage of our proposed ACMF is an RCMF. Its structure is shown in Fig. 4. It is a mushroom-type RCMF. Its working frequency is 2.45 GHz. The transmission zero of the mushroom-type RCMF happens in the middle of the structure. The simulation results of the mushroom type RCMF is shown in Fig. 5. The dimension of this RCMF is 3x2.5 mm.

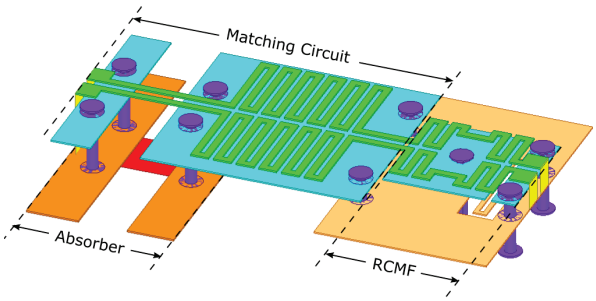

Fig. 3. The structure of proposed ACMF.

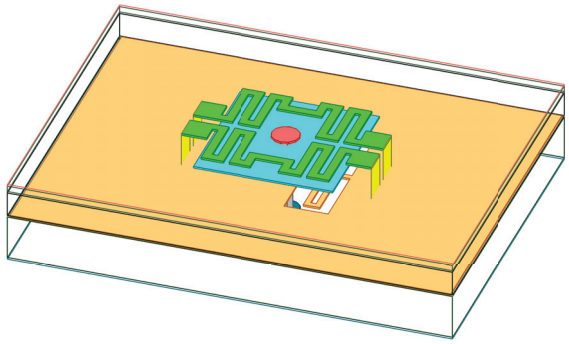

Fig. 4. The structure of proposed RCMF.

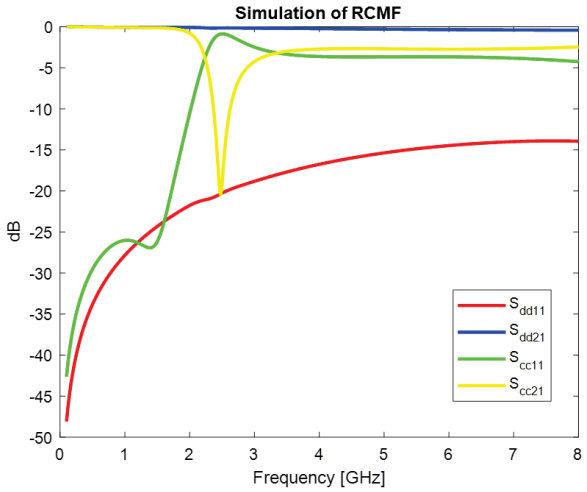

Fig. 5. The simulation results of RCMF.

It is seen in Fig. 5 that S_{dd21} only decreased slightly (less than −1 dB) for the frequency range of 0–8 GHz. This shows that the integrity of the differential signals is well maintained. We also see that the insertion loss of CM S_{cc21} reached its lowest value of around −20 dB at 2.45 GHz. Meanwhile, the return loss of CM S_{cc11} reached its highest value (less than −1 dB) at a frequency of 2.45 GHz. This means that at a frequency of 2.45 GHz the common mode noise is not transmitted to the next device but is reflected back to the previous device. This proves that this filter is an RCMF.

B. Matching circuit

The function of the Matching Circuit is to bring the short circuit impedance from the center of the RCMF to the input port of the series-type absorber. The goal is that as much of the reflected common mode noise energy that occurs in the center of the RCMF is channeled to the absorber to be dissipated into heat so that it does not flow to the device located at the ACMF input. This matching circuit is implemented using a transmission line with a length of $\lambda/2$, where λ is the electromagnetic wavelength with a frequency of 2.45 GHz, which is the ACMF working frequency. To reduce the dimensions, the matching circuit transmission line is made in the form of a meander.

C. Series-type absorber

The absorber is used to absorb the CM noise energy reflected by the RCMF by passing it through a resistor so that the energy turns into heat. By dissipating the CM noise energy into heat, the CM noise energy no longer interferes with RF (Radio Frequency) devices around it. This absorber is implemented using a 0805 SMD resistor and is installed in serial position with the system ground through which common mode energy passes. Technically, we cut the system ground plane immediately after the input port of the ACMF so that there is a gap in the system ground. Into this gap an SMD resistor is serially installed in such a way that the SMD resistor connects the two planes of the cut off system ground. This SMD resistor is safe and suitable for use in ACMF because the maximum power that can be applied to this SMD resistor is 0.5 W and its size is 2.00×1.25×0.50 mm [13]. The resistance used for this SMD resistor is 25 Ω. This absorber resistance is chosen according to the input impedance of the CM noise so that the transfer of CM noise energy to the absorber is maximum.

III. SIMULATED AND FABRICATED ACMF

This section presents measurement results both in simulation and fabricated of designed ACMF. The simulation was made by using HFSS software from Ansys and the real ACMF was made at the factory based on this simulation. We named it the fabricated ACMF and it is shown in Fig. 6 and Fig. 7, which are the fabricated ACMF top view and bottom view, respectively.

The measurement results of the simulated ACMF are shown in Figs. 8-11 in green line, meanwhile the measurement results of the fabricated ACMF are shown in red line. The comparison between them is shown in Table1.

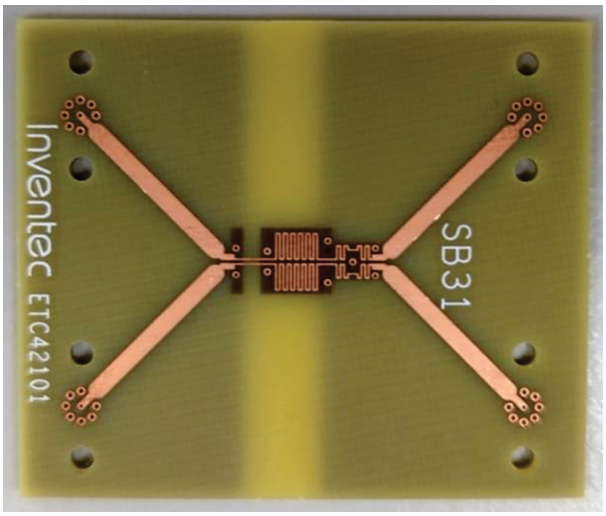

Fig. 6. Fabricated ACMF, top view.

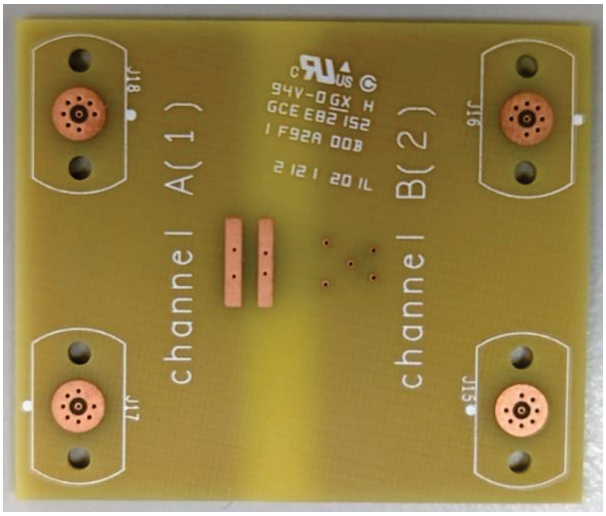

Fig. 7. Fabricated ACMF, bottom view.

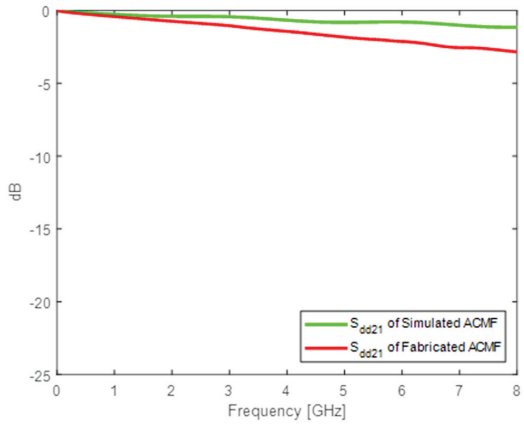

Fig. 8. The comparison between the S_{dd21} of the simulated and fabricated ACMF.

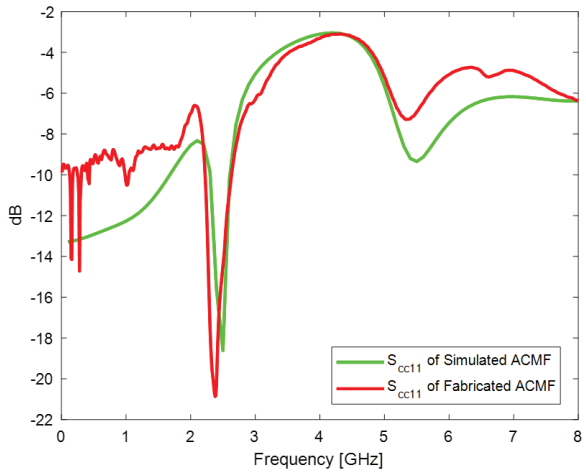

Fig. 9. The comparison between the S_{cc11} of the simulated and fabricated ACMF.

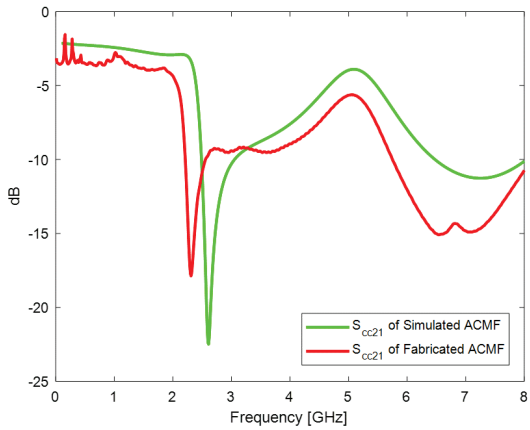

Fig. 10. The comparison between the S_{cc21} of the simulated and fabricated ACMF.

Table 1: Comparison between Simulation and Fabrication

	Simulation		Fabrication	
S_{cc21}	-22.49 dB	2.61 GHz	-17.87 dB	2.31 GHz
S_{cc11}	-18.62 dB	2.5 GHz	-20.87 dB	2.38 GHz
S_{dd21}	<-1 dB	8 GHz	<-2.8 dB	8 GHz
AE	92.8%	2.54 GHz	97%	2.32 GHz
Fract. BW	19%		17%	

IV. DISCUSSIONS

S parameter is used to analyze the characteristics of common mode filters. The ones that are often used are S_{dd21}, S_{cc21}, and S_{cc11} [6, 8,15–17]. S_{dd21} is the insertion loss of DM which is ideally 0 dB. S_{cc21} is the insertion loss of CM which is ideally $-\infty$ dB. S_{cc11} is the return loss of CM which is ideally $-\infty$ dB for ACMF.

Table 2: Comparison between Series and Parallel ACMF

Parameter [Unit]	This Paper	Paper [18]	Paper [19]	Paper [20]
Absorption freq. [GHz]	2.32	2.25	3.55	2.45
Absorption efficiency [%]	97	96	97	97
Dimensions [mm]	10.3 x4.6	8.65x2.5	28.6x13.5	16x3.5

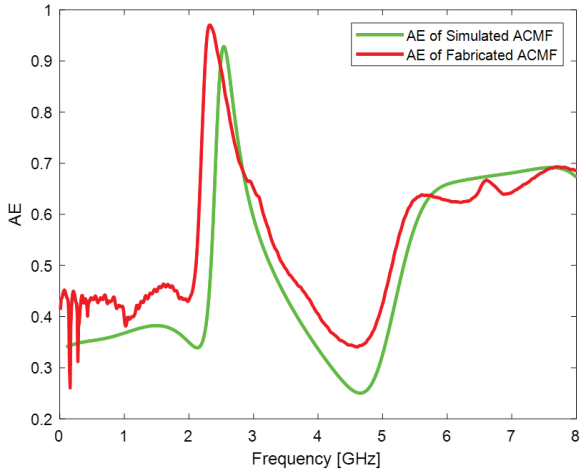

Fig. 11. The comparison between the Absorption Efficiency of the simulated and fabricated ACMF.

From simulation results, Fig. 8 shown that S_{dd21} is −0.4 dB at frequency 2.45 GHz. Therefore, the insertion loss of DM signal in our simulation is very small, i.e. integrity of the DM signal that is passed in the proposed ACMF is well maintained. Figure 9 shown that S_{cc11} for the frequency of 2.45 GHz is about –19 dB. his means that the reflected CM noise in our simulation has been reduced quite significantly. Figure 10 shown that the minimum for S_{cc21} with a level of –23 dB occurs at a frequency slightly above 2.45 GHz. This means that the CM attenuation in our simulation is very large and occurs slightly above the expected frequency. In Figure 11, it can be seen that the maximum absorption efficiency of about 93% occurs at a frequency of around 2.5 GHz. As a result, at a frequency of around 2.5 GHz, our simulation succeeded in reducing and absorbing 93% of the CM noise that passes through it.

The real ACMF was fabricated at the factory based on this simulation as shown in Figs. 6 and 7. The comparison between the measurement results and the simulation results are shown in Figs. 8–11 in which we can clearly see that the S parameter measurements are slightly different from the measurement results in the simulation. These differences are caused by the addition of transmission lines, which are used to connect ACMF ports with measurement terminals as we can see in Fig. 6. However, these differences can be tolerated because they are small and the overall results of these measurements show the same pattern and close similarity.

In addition, the absorption efficiency obtained from fabricated ACMF is also greater than that obtained from simulated ACMF. This AE, which is generated by a series ACMF, is also compared with the AE generated by a parallel ACMF and made by other researchers [18] as shown by Table 2.

Table 2 is a comparison of the data between the ACMF that we made and several ACMFs produced by other researchers as written in the papers [18–20]. Frequency absorption occurs at adjacent frequencies, namely: 2.32 GHz, 2.25 GHz, 3.55 GHz, and 2.45 GHz, so this comparison is valid because the ACMF works at adjacent frequencies. Although our ACMF dimension is larger than the ACMF dimension reported by the paper [18], the Absorption efficiency generated by our ACMF is greater than the ACMF absorption efficiency reported by the paper [18]. Papers [19, 20] reported absorption efficiencies similar to absorption efficiency produced by our ACMF, but our ACMF dimension is smaller than those reported in the same papers.

In addition, the fabricated series ACMF can maintain the integrity of differential signal well. As we can see in Fig. 8, it can be seen that at a frequency of around 2.5 GHz the DM insertion loss value of S_{dd21} is less than −1 dB. Thus, we can conclude that the simulation of the series ACMF that we have designed has been successful and can be implemented on the PCB with good S parameter measurement results.

V. CONCLUSIONS

The motivation of this research is to identify a technique to reduce CM noise at a frequency of 2.45 GHz so as not to interfere with RF devices operating in the vicinity of this frequency, such as Wi-Fi transceiver module. Our experiment solved this problem with the success of our simulated ACMF and fabricated ACMF to reduce CM noise at the frequency of near the 2.45 GHz. We use an SMD resistor in our ACMF to absorb CM noise. The absorption efficiency that we managed to achieve in the simulation was 93%, while our fabricated ACMF managed to achieve an absorption efficiency of 97%. In addition, our simulated ACMF and fabricated ACMF also managed to maintain the integrity of the DM signal that passes through it with a DM insertion loss of less than – 0.5 dB and less than –1 dB respectively at

frequencies of around 2.45 GHz. The next thing, the dimension of our proposed ACMF is also small. For future development, the method used in our experiment can be further developed to achieve better characteristics and smaller dimensions.

ACKNOWLEDGMENT

This work was supported by Ministry of Science and Technology of Taiwan (Grant MOST 110-2221-E-011-052).

REFERENCES

[1] C. Y. Zhuang, T. Adiprabowo, D. B. Lin, Y. H. Chen, Y. H. Zheng, B. H. Tsai, and A. A. Pramudita, "A broadband common-mode filter by using dual band transmission zero," *2021 Asia-Pacific International Symposium on Electromagnetic Compatibility (APEMC)*, pp. 1-3, 2021.

[2] Z. Zhu, W. Yan, Y. Wang, Y. Zhao, T. Zhang, and J. Huang, "Noise analysis method of radiated EMI based on non-linear principal component analysis," *Applied Computational Electromagnetics Society (ACES) Journal*, vol. 35, no. 10, p. 1144–1152, 2020.

[3] Z. Chen and G. Katopis, "A comparison of performance potentials of single ended vs. differential signaling," *Electrical Performance of Electronic Packaging - 2004*, pp. 185–188, 2004.

[4] D. G. Kam, H. Lee, J. Kim, and J. Kim, "A new twisted differential line structure on high-speed printed circuit boards to enhance immunity to crosstalk and external noise," *IEEE Microwave and Wireless Components Letters*, vol. 13, no. 9, pp. 411–413, 2003.

[5] E. Bogatin, *Signal and Power Integrity, Simplified*, Prentice Hall, Upper Saddle. River, NJ 3rd edn., 2018.

[6] W. T. Liu, C. H. Tsai, T. W. Han, and T. L. Wu, "An embedded common-mode suppression filter for GHz differential signals using periodic defected ground plane," *IEEE Microwave and Wireless Components Letters*, vol. 18, no. 4, pp. 248–250, 2008.

[7] F. de Paulis, L. Raimondo, S. Connor, B. Archambeault, and A. Orlandi, "Compact configuration for common mode filter design based on planar electromagnetic bandgap structures," *IEEE Transactions on Electromagnetic Compatibility*, vol. 54, no. 3, pp. 646–654, 2012.

[8] S. J. Wu, C. H. Tsai, T. L. Wu, and T. Itoh, "A novel wideband common-mode suppression filter for gigahertz differential signals using coupled patterned gound structure," *IEEE Transactions on Microwave Theory and Techniques*, vol. 57, no. 4, pp. 848–855, 2009.

[9] K. Yanagisawa, F. Zhang, T. Sato, K. Yamasawa, and Y. Miura, "A new wideband common-mode noise filter consisting of Mn-Zn ferrite core and copper/polyimide tape wound coil," *IEEE Transactions on Magnetics*, vol. 41, no. 10, pp. 3571–3573, 2005.

[10] B. F. Su and T. G. Ma, "Miniaturized common-mode filter using coupled synthesized lines and mushroom resonators for high-speed differential signals," *IEEE Microwave and Wireless Components Letters*, vol. 25, no. 2, pp. 112–114, 2015.

[11] H. W. Liu, C. H. Cheng, P. J. Li, and T. L. Wu, "A novel compact single-stage absorption common-mode filter," *IEEE Transactions on Electromagnetic Compatibility*, vol. 64, no. 1, pp. 111–118, 2022.

[12] H. W. Liu and T. L. Wu, "A wideband single-cell unidirectional absorption common-mode filter with pattern ground structure," *2022 Asia-Pacific International Symposium on Electromagnetic Compatibility (APEMC)*, pp. 13–15, 2022.

[13] T. Adiprabowo, D. B. Lin, Y. H. Zheng, Y. H. Chen, C. Y. Zhuang, and B. H. Tsai, "Dual-band high absorbing and broadband suppressing common-mode noise filter," *IEEE Transactions on Electromagnetic Compatibility*, pp. 1–10, 2021.

[14] "IEEE Standard for Information Technology — Telecommunications and information exchange between systems Local and metropolitan area networks—Specific requirements - Part 11: Wireless LAN Medium Access Control (MAC) and Physical Layer (PHY) Specifications," *IEEE Std 802.11-2016 (Revision of IEEE Std 802.11-2012)*, pp. 1–3534, 2016.

[15] C. H. Wu, C. H. Wang, and C. H. Chen, "Novel balanced coupled-line bandpass filters with common-mode noise suppression," *IEEE Transactions on Microwave Theory and Techniques*, vol. 55, no. 2, pp. 287–295, 2007.

[16] C. H. Tsai and T. L. Wu, "Novel balanced coupled-line bandpass filters with common-mode noise suppression," *IEEE Transactions on Microwave Theory and Techniques*, vol. 58, no. 1, pp. 195–202, 2010.

[17] X. H. Wu and Q. X. Chu, "Compact differential ultra-wideband bandpass filter with common-mode suppression," *IEEE Microwave and Wireless Components Letters*, vol. 22, no. 9, pp. 456–458, 2012.

[18] P. J. Li, Y. C. Tseng, C. H. Cheng, and T. L. Wu, "A novel absorptive common-mode filter for cable radiation reduction," *IEEE Transactions on Components, Packaging and Manufacturing Technology*, vol. 7, no. 4, pp. 511–518, 2017.

[19] S. K. Tseng, C. N. Chiu, Y. C. Tsao, and Y. P. Chiou, "A novel ultrawideband absorptive common-mode filter design using a miniaturized and resistive defected ground structure," *IEEE Transactions on Electromagnetic Compatibility*, vol. 63, no. 1, pp. 66–73, 2021.

[20] P. J. Li, C. H. Cheng, and T. L. Wu, "A resistor-free absorptive common-mode filter using gap-coupled resonator," *IEEE Microwave and Wireless Components Letters*, vol. 28, no. 10, pp. 885–887, 2018.

Ding-Bing Lin (S'89–M'93–SM'14) received M.S. and Ph.D. degrees in Electrical Engineering from National Taiwan University, Taipei, Taiwan, in 1989 and 1993, respectively.

From August 1993 to July 2016, he was a Faculty Member with the Department of Electronic Engineering, National Taipei University of Technology (Taipei Tech), Taipei, Taiwan, where he was an Associate Professor, Professor, and Distinguished Professor in 1993, 2005, and 2014, respectively. Since August 2016, he has been a Professor with the Department of Electronic and Computer Engineering, National Taiwan University of Science and Technology (Taiwan Tech). He is currently directing a human resources cultivation program named the Promotion Center for 5G Antennas and Radio Frequency Techniques Consortium. He has authored or coauthored more than 200 papers in international journals and at international conferences, respectively. His research interests include wireless communication, radio multipath fading channel modeling, mobile antennas, high-speed digital transmission, and microwave engineering.

Dr. Lin was the recipient of the Annual Research Outstanding Award of the College of Electrical Engineering and Computer Science in 2004, 2006, and 2008. After he had received these three awards, the College of Electrical Engineering and Computer Science awarded him the College Research Outstanding Award to highlight his research achievements. He was also the recipient of the Taipei Tech Annual Outstanding Research Award in 2008. He was the Chair of the Taipei Chapter, IEEE Broadcasting Society, from 2010 to 2014, the Technical Program Committee Chair of the 2015 Asia-Pacific International EMC Symposium, and the Chair of the Taipei Chapter, IEEE EMC society from 2015 to 2018. He has been on the Associate Editor of the IEEE Transaction on EMC since 2019 and the Editorial Board of the International Journal of Antennas and Propagation since 2014.

Erfansyah Ali received B.Eng. (2005) and M.Eng. (2012) degrees in Communications from the Electrical Engineering Department, Intitut Teknologi Bandung (ITB). Currently, he is a lecturer at School of Electrical Engineering, Telkom University, and a PhD student at National Taiwan University of Science and Technology (NTUST). His research interests are in Radar Systems, RF device, and Signal Processing.

Tjahjo Adiprabowo received a B. Eng. degree in Telecommunication Engineering from Bandung Institute of Technology, Bandung, Indonesia, in 1987, and a M. Eng. degree in Telecommunication Engineering from Royal Melbourne Institute of Technology, Melbourne, Australia, in 2001. He is now pursuing a Ph.D. degree in Wireless Engineering at the Department of Electronic and Computer Engineering in National Taiwan University of Science and Technology, Taipei, Taiwan. From 1987 to 1991, he worked as a Satellite Ground Station Engineer for PT. Elektrindo Nusantara, in Jakarta, Indonesia. From 1991 to 2000, he worked as a Mainframe System Programmer for PT. Telekomunikasi Indonesia, in Bandung, Indonesia. From 2001 to 2012, he worked as a Network Performance Engineer for PT. Telekomunikasi Indonesia, in Bandung, Indonesia. Since 2012, he has been a Lecturer in School of Electrical Engineering in Telkom University, in Bandung, Indonesia. His research interests include Wireless Engineering, Wireless Sensor Networks, Radar Engineering, and Common-Mode Noise Filters.

Cheng-Yi Zhuang (S'20) was born in Pingtung, Taiwan. He received a B.S. degree in Electronic and Computer Engineering from National Taiwan University of Science and Technology, Taipei, Taiwan, in 2019, where he is currently pursuing a Ph.D. degree.

A Band Stop to Band Pass Filter Transformation Utilizing 3-D Printing Technique for C-band Applications

Wael A. E. Ali[1], Ahmed A. Ibrahim[2], and Ashraf E. Ahmed[3]

[1]Department of Electronics & Communications Engineering, College of Engineering and Technology
Arab Academy for Science, Technology and Maritime Transport (AASTMT), Alexandria, Egypt
wael.ali@aast.edu

[2]Electronic Engineering Department
Minia University, El-Minia, Egypt,
ahmedabdel_monem@mu.edu.eg

[3]Electronics & Comm. Engineering Department
College of Engineering, Higher Institute of Engineering and Technology, King Marriott, Alexandria, Egypt
aeltyib_ahmd@yahoo.com

Abstract – In this paper, a band-pass filter (BPF) based on split-ring resonator (SRR) using a 3-D printing technique for C-band applications is introduced. The proposed filter is designed to operate at a frequency of 3.9 GHz. An innovative technique for printing the substrate with a size of $24 \times 24 \times 1.1$ mm^3 using PLA dielectric material is implemented. The copper sheet with a thickness of 0.1 mm is printed on the upper and lower faces of the substrate. First, the SRR band stop filter (BSF) is introduced then two L-Stubs are inserted to implement an additional band stop region, and this rejoin is adjusted to obtain a band-pass region between the two stopbands. The BPF is operated at a 3-dB bandwidth extended from 3.5 GHz to 4.3 GHz with an S_{21} level of -0.2 dB for the simulated results while it achieves a 3-dB bandwidth within 3.6 GHz to 4.2 GHz (15.3 %) with an S_{21} level of -1.8 dB for the measured results.

Index Terms – 3-D printing, bandpass filter, C-band applications, PLA.

I. INTRODUCTION

Filters play a very important role in many RF microwave applications. They are commonly utilized in transceiver circuits to isolate or merge various frequencies. A band-pass filter allows components to pass in a specific frequency band, known as the passband while blocking other components of frequencies that are higher than or lower than this band [1, 2]. Bandpass filters are commonly used in wireless transmission and reception. The main purpose of the filter is to pass an output signal with a certain range of frequencies allocated for transmission to avoid interference with the neighboring [3, 4]. Several studies are conducted to achieve a bandpass behavior that fulfills modern technological market needs such as compact size, sharp roll-off rate, wide stopband, and low passband insertion loss [5–9]. Various techniques are carried out to achieve the required bandpass behavior as in [10–17]. In [10], the defected ground structure is used to obtain a wide band stop behavior while passing all frequencies in the range of 2.4-14.3 GHz. The stepped impedance resonator (SIR) is one of the most commonly used techniques to provide a bandpass behavior and it succeeded to achieve a triple band (1.85 GHz, 2.575 GHz, and 3.05 GHz) with skew-symmetric (0-degree) tapped-feed structure as in [11]. The open-loop resonator (OLR) technique was carried out in [12] for dual passbands (WLAN and WiMAX). Another technique substrate integrated wave (SIW) was used in [13] to achieve a band-pass response (15.6–32.1 GHz) in the RF and millimetric wave frequency range with an enhanced insertion loss in the passband (> -0.8 dB). To obtain a millimeter band-pass response, a split ring resonator (SRR) was used [14], and the achieved performance was quite enough to make the suggested filter a good candidate for 5G networks.

Nowadays, 3-D printing, or additive manufacturing (AM), is the building block of a three-dimensional object from a digital 3-D model. The entire 3D printing technology can be divided into 3 steps 1st 3D design, 2nd slicing, 3rd 3D printing [15]. 3D printing techniques are used recently in designing microwave components such as filters and antennas. It can be used to construct antenna models for multiband applications as in [16–19]. Additionally, there are various designs of microwave filters based on 3D printing in the RF frequency range

Submitted On: July 26, 2022
Accepted On: December 20, 2022

https://doi.org/10.13052/2022.ACES.J.371105

[20–21], and the implemented BPF in [22] was operated in the E-band (60-90 GHz) of the millimetric wave frequency range, but with inconsistent simulation and experimental results due to fabrication tolerance.

II. SRR BSF

The 2-D structure of the SRR BSF is illustrated in Fig. 1. The BSF has a $\lambda/2$ open-loop transmission line and the SRR is fed by a 50Ω microstrip line connected with SMA connectors. The PLA substrate material with a dielectric constant of 3.1, loss tangent of 0.001, and height of 1.1 mm is utilized. The detailed dimensions of the filter parameter are depicted in Fig. 1 (a) and listed in the figure caption. The simulated (CST & HFSS) outcomes of the BSF are illustrated in Fig. 2. The suggested BSF is operating at 5 GHz with 2.7 GHz 3-dB bandwidth from 3.7 GHz to 6.4 GHz) and the achieved return loss over the entire stopband is approximately 0.2 dB. To verify the achieved results in Fig. 2 the electric field distribution is simulated at different frequencies outside (3 and 7 GHz) and inside the stopband (5 GHz) as shown in Fig. 3. It is clear that at 3 GHz, the electric field is conducted to port 2 through the open-ended loop as shown in Fig. 3 (a) and the same behavior is noticed when the filter is excited at 7 GHz but the major concentration of field was through the aligned arm of the resonator with the two feedlines as shown in Fig. 3 (c). However, at 5 GHz as shown in Fig. 3 (b), the electric field couldn't pass to port 2 and is concentrated on port 1 and the left part of SRR confirming the capability of the suggested filter to behave as a BSF in the desired band. Furthermore, the current distribution of the suggested filter is demonstrated in Fig. 4 and the current distribution is carried out at the same three frequencies which were used in the field distribution confirming the ability of the suggested filter to pass all frequencies except the desired band from 3.7 to 6.4 GHz.

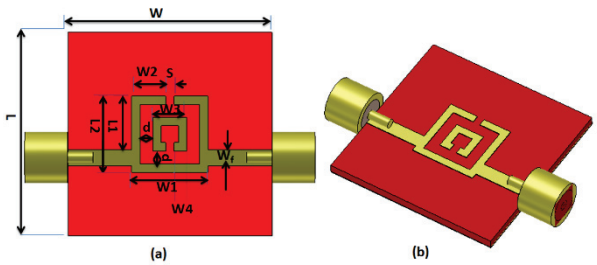

Fig. 1. The configuration of SRR BSF. (a) 2-D configuration with W = L = 24 mm, W1 = 9 mm, W_f = 1.95 mm, d = 1.5 mm, S = 1mm, W2 = 4 mm, L1 = 6.3 mm, L2 = 9 mm, W3 = 4 mm, and W4 = 1.5 mm. (b) 3-D configuration.

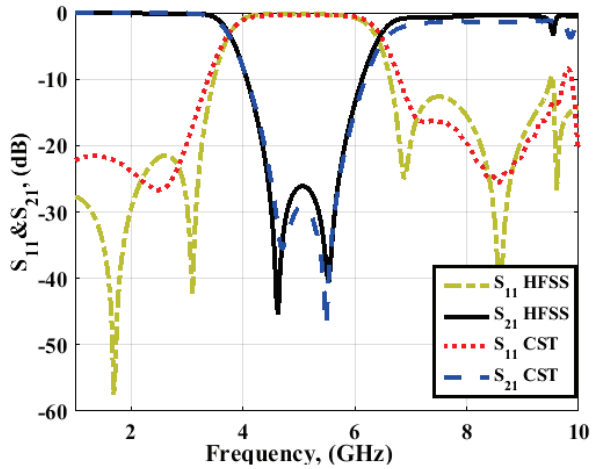

Fig. 2. The simulated SRR BSF S-parameters results.

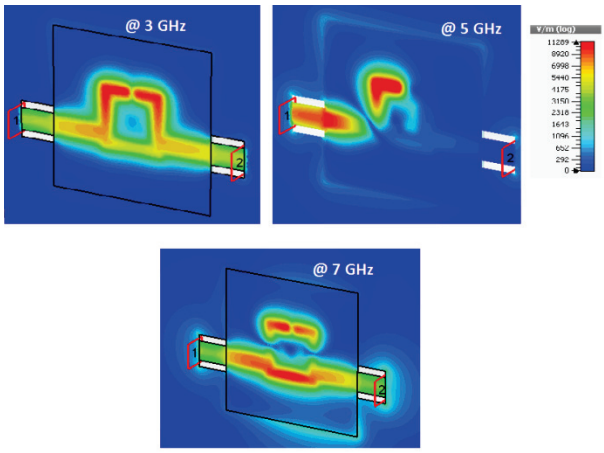

Fig. 3. The simulated distributions of electric field results of SRR BSF at z=0.6 mm (inside substrate).

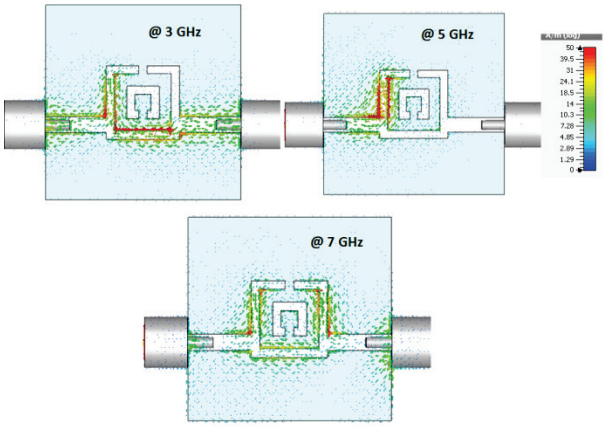

Fig. 4. The current distribution's simulated results of SRR BSF.

III. PROPOSED SRR BPF/BSF

To produce the dual-band operation of the SRR-BSF, an additional resonator is introduced in Fig. 5 with dimensions L_S and W_S. It is worth noting that the dimensions of the additional resonator are larger than the fundamental one, so the achieved rejection band will be in the lower frequency range. Consequently, it is evident from Fig. 6 of the achieved simulated results of insertion and return loss using HFSS and CST programs that the suggested filter has two operating stopbands, the first one covers the range from 2.1 to 3.4 GHz with a deeper insertion loss of 47 dB at 3 GHz, and the second band covers the old frequency range with a reduction of 0.4 GHz (4.4 – 6.4 GHz) and this is due to the coupling with the additional SRR. Furthermore, a new BPF behavior is accomplished in the frequency range (3.5 – 4.3 GHz) with an insertion loss of level 0.2 dB confirming the readability of the suggested BPF to be embedded in different applications that cover the achieved frequency band. There is a discrepancy between HFSS and CST results, especially at the extremely lower and higher frequencies of the achieved rejection bands and this may be due to the different meshing operations of both programs.

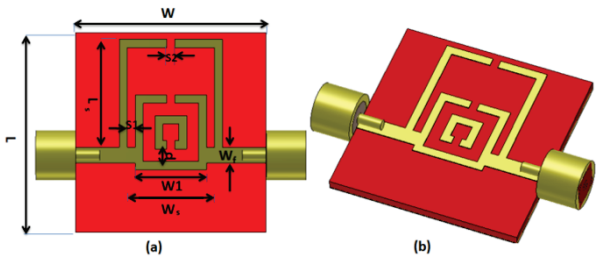

Fig. 5. The configuration of the proposed SRR BPF/BSF (a) 2-D configuration with W= L=24 mm, W1= 9 mm, W_f = 1.95 mm, d= 1.5 mm, S1=1 mm, S2= 1 mm, L_s= 13 mm, W_s = 10 mm (b) 3-D configuration.

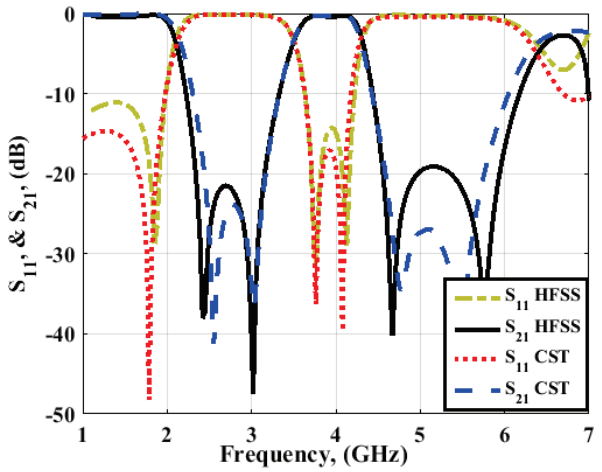

Fig. 6. S-parameters simulated results of SRR BPF/BSF.

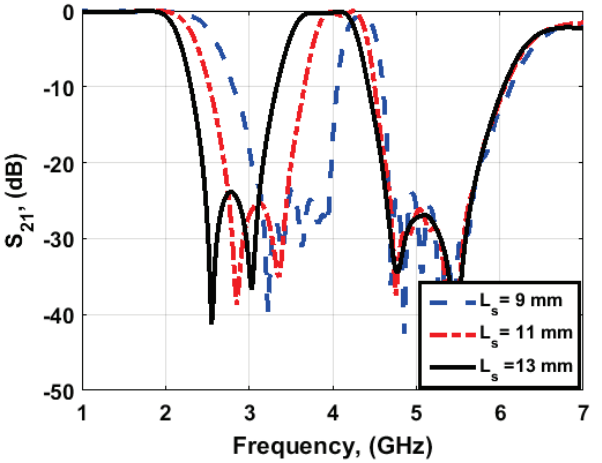

Fig. 7. The S_{21} simulated results of SRR BPF/BSF at different values (Ls).

The parametric study is carried out to illustrate the effect of the SRR length (Ls), its width (W1), and the spacing between inner and outer SRRs (S1) on the filter performance. The effect of changing the length of Ls on the behavior of the proposed filter is presented in Fig. 7 and it is obvious that the length change has a significant effect on the lower band since the operating frequency is translated to the lower range by increasing Ls, also it has a minor effect on the achieved upper-frequency band. Another parameter is changed to investigate its effectiveness which is the width "W1". It can be observed from Fig. 8 that both stopbands are translated to a lower range by increasing W1 and the level of translation in the higher band is greater than that of the lower band since the shift in the upper band is about 0.8 GHz and the lower band 0.4 GHz when increasing W1 to 10 mm. Additionally, when increasing W1 to 11 mm, the upper band is shifted down by 0.6 GHz and the lower band by 0.1 GHz. Consequently, the parameter W1 has a great influence, especially for the upper stopband and it also deteriorates the insertion loss performance when it is increased. It is very obvious in the passband since it is not only decreasing the insertion loss level but also the achieved bandwidth as demonstrated in Fig. 8. The parametric study of the last investigated parameter "S1" is clarified in Fig. 9. The spacing between the SRR and the L-stubs has a significant effect on the lower rejection band since the frequency is shifted down by about 0.2 GHz per increase of 1 mm for S1. Hence, the achieved passband is translated to a lower frequency range with an increased passband bandwidth but with the degraded performance of insertion loss.

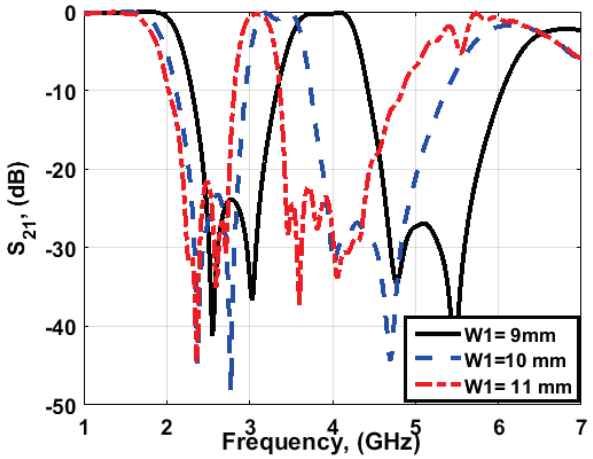

Fig. 8. The S_{21} simulated results of SRR BPF/BSF at different values (W1) of the SRR cell.

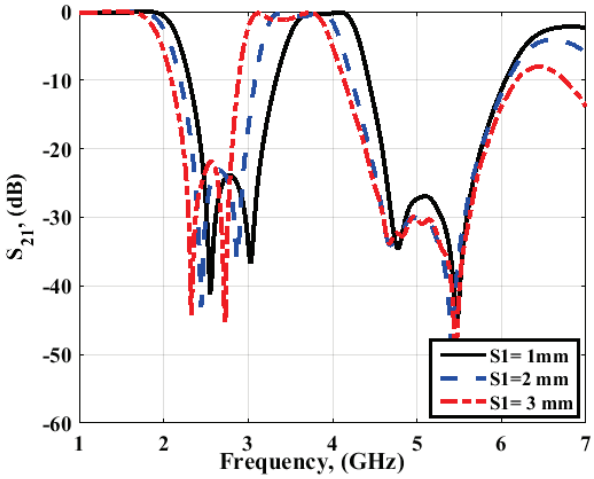

Fig. 9. The S_{21} simulated results of SRR BPF/BSF for different values of S1.

The surface current distribution of the suggested filter is investigated to verify the BPF performance at three resonance frequencies (3, 4, and 5 GHz). As can be observed in Fig. 10, the current is uniformly distributed from port 1 to port 2 at 4 GHz, while it is blocked at the left side of the L-stubs when it is simulated at 3 GHz and the left side of the primary SRR when it is simulated at 5 GHz.

The same performance is achieved when the electric field is investigated as in Fig. 11 confirming the ability of the suggested BPF to transfer all signals in the desired frequency band (3.5-4.3 GHz) only while rejecting all other frequencies.

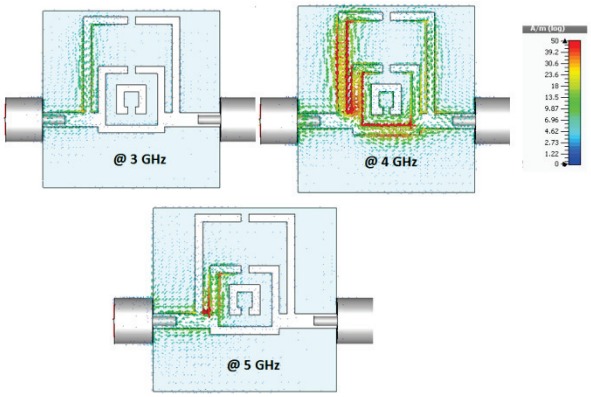

Fig. 10. The current distribution's simulated results of SRR BPF/BSF.

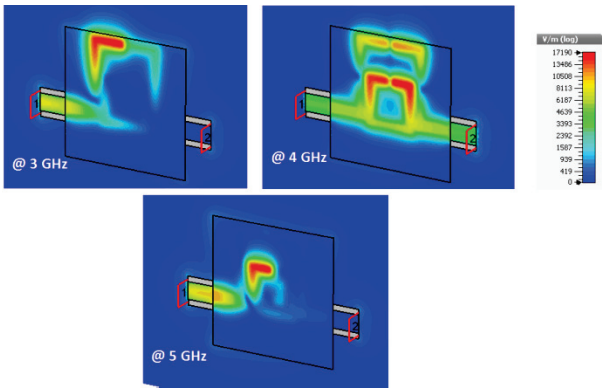

Fig. 11. The electric field distribution's simulated results of SRR BPF/BSF at z=0.6 mm.

IV. EXPERIMENTAL OUTCOMES

The proposed SRR-based BPF/BSF is fabricated using copper tape of the thickness of 0.1 mm and then implemented on a layer of 3-D printed PLA substrate with 3.1 dielectric constant and 2 mm thickness. Two 50-ohm SMA connectors are connected to the suggested filter through 50-ohm transmission lines as depicted in Fig. 12. The proposed filter is tested to verify its behavior using R&S ZVB 20 vector network analyzer (VNA). The simulated and measured results of return and insertion

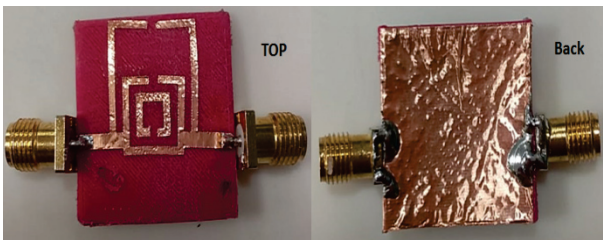

Fig. 12. The fabricated photo of the proposed SRR BPF/BSF.

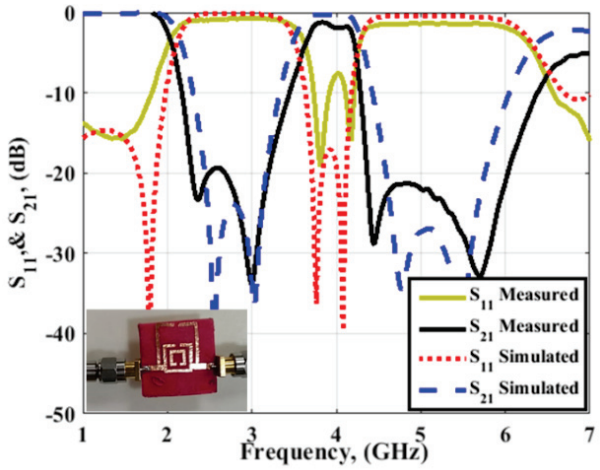

Fig. 13. The S-parameters simulated and measured results of SRR BPF/BSF.

Table 1: Comparison between proposed work and reported filters

Ref.	Response	f_o (GHz) / FBW (%)	S_{21}(dB)	Size (λ_g)	ε_r/h (mm)
[8]	Single-BPF	5.3 / 8.68	1.5	0.58 × 0.65	3.38/0.813
[9]	Triple-BPF	6.5/7.35 /8.15 / 2.31/2.04 /2.45	1.74/1.82 /1.96	2.2 × 0.61	2.2/0.787
[10]	UWB-BPF	8.35 / 143	1.5	1.28 × 0.36	4.4/1.6
[23]	Triple-BPF	2.5/3.4 /4.9 / 12/21/25	-	0.49 × 0.37	2.2/0.787
[24]	Triple-BPF	1.75/2.55 /3.55 / 21.2/4.7 /8.4	0.55/1.36 /1.37	0.32 × 0.12	2.2/1.575
This work	Single-BPF	3.9 / 15.3	1.8	0.55 × 0.55	3.1/1.1

losses are presented in Fig. 13. The BPF is operated at 3-dB bandwidth extended from 3.5 GHz to 4.3 GHz with an S_{21} level of -0.2 dB for the simulated results, while it achieves 3-dB bandwidth within 3.6 GHz to 4.2 GHz (15.3 %) with an S_{21} level of -1.8 dB for the measured results. Good consistency between the simulated and the measured results can be noticed with a slight reduction of the achieved band and this may be due to the non-conformal stacking of the copper tape on the PLA surface and the misalignments of copper tape sections. A comparison with the recently reported work is illustrated in Table 1.

V. CONCLUSION

A compact 3-D printing BPF has been proposed. The filter has been printed on a PLA substrate. The entire size of the final filter substrate was $24 \times 24 \times 1.1$ mm^3. The BPF has been operated at a 3-dB bandwidth extended from 3.4 GHz to 4.3 GHz with an S_{21} level of -0.2 dB for the simulated results while it achieves a 3-dB bandwidth within 3.6 GHz to 4.2 GHz (15.3 %) with an S_{21} level of -1.8 dB for the measured results. These outcomes enable the filter can be used in C-band applications.

REFERENCES

[1] L. Zhou, Y. Z. Yin, W. Hu, and X. Yang, "Compact bandpass filter with sharp out-of-band rejection and its application," *Applied Computational Electromagnetics Society (ACES) Journal*, vol. 32, no. 3, pp. 249-255, 2017.

[2] A. Rajput, K. Patel, and A. Birwal, "Compact microstrip low pass filter design using U-shaped folded high-impedance line," *Microwave and Optical Technology Letters*, vol. 60, no. 7, pp. 1812-1815, 2018.

[3] A. A. Ibrahim, M. A. Abdalla, and W. A. E. Ali, "Small size and wide-band band pass filter with DGS/CRLH structures," *Applied Computational Electromagnetics Society (ACES) Journal*, vol. 34, no. 5, pp. 777-783, 2019.

[4] Z. Zhu, L. Cao, and C. Wei, "Novel compact microstrip dual-mode filters with two controllable transmission zeros," *Applied Computational Electromagnetics Society Journal (ACES)*, vol. 33, no.1, pp. 43-48, 2018.

[5] A. Sami, M. Rahman, H. Ahmad, and S. Bashir, "Design strategy for compact bandpass filters using meander line resonators," *Applied Computational Electromagnetics Society (ACES) Journal*, vol. 35, no. 1, pp. 44-50, 2020.

[6] A. A. Ibrahim, H. A. Mohamed, and W. A. E. Ali, "Tunable dual/triple band-pass filter based on stub-loaded resonators for wireless applications," *Journal of Instrumentation*, vol. 12, pp. 1-12, 2017.

[7] A. A. Ibrahim, W. A. E. Ali, and M. A. Abdelghany, "Design of dual-band dual-mode band-pass filter utilizing 0° feed structure and lumped capacitors for WLAN/WiMAX applications," *Electronics*, vol. 9, no. 10, pp. 1697, 2021.

[8] A. Boutejdar, A. A. Ibrahim, and W. A. E. Ali, "Design of compact size and tunable band pass filter for

WLAN applications," *Electronics Letters*, vol. 52, no. 24, pp. 1996-1997, 2016.

[9] Z. Yang, B. You, and G. Luo. "Dual−/tri-band bandpass filter using multimode rectangular SIW cavity," *Microwave and Optical Technology Letters*, vol. 62, no. 3, pp. 1098-1102, 2020.

[10] K. A. Ansal, D. S. Jose, A. S. Kumar, and T. Shanmugantham, "A band pass coupled line filter with DGS for ultra-wide band application," *Procedia Computer Science*, vol. 171, pp. 561-567, 2020.

[11] J. Chen, J. Zhong, J. Shen, N. Gao, and A. Zhang, "Design of compact tri-band filter based on sir-loaded resonator with 0° tapped-feed structure," *Frequenz*, vol. 69, no. 9-10, pp. 389-392, 2015.

[12] A. A. Ibrahim, M. A. Abdalla, and W. A. E. Ali, "Dual band pass filter with sharp transmission zeros for wireless applications," *Journal of Instrumentation*, vol. 13, no. 6, P06020, 2018.

[13] L. Zhao, Y. Li, Z. M. Chen, X.H. Liang, J. Wang, X. Shen, and Q. Zhang, "A band-pass filter based on half-mode substrate integrated waveguide and spoof surface plasmon polaritons," *Scientific Reports*, vol. 9, no. 1, pp.1-8, 2019.

[14] M. Amzi, S. D. Bennani, J. Zbitou, and A. Belmajdoub, "Design of compact bandpass filter based on SRR and CSRR for 5G applications," *International Conference on Electronic Engineering and Renewable Energy*, Springer, Singapore, pp. 175-181, 2020.

[15] G. Carranza, U. Robles, C. L. Valle, J. J. Gutierrez, and R. C. Rumpf, "Design and hybrid additive manufacturing of 3D/volumetric electrical circuits," *IEEE Trans. on Components, Packaging, and Manufacturing Technology*, vol. 9, no. 6, pp. 1176-1183, 2019.

[16] A. E. Ahmed, W. A. E. Ali, A. Chowdhury, and S. Das, "A 3-D printed trapezoidal antenna for X-band wireless communications applications," *Futuristic Communication and Network Technologies*, Springer, Singapore, pp. 949-956, 2022.

[17] A. E. Ahmed and W. A. E. Ali, "Analysis and design of 3-D printed fractal triangular antenna for wireless communications applications." *International Conference on Electrical, Communication, and Computer Engineering (ICECCE),* pp. 1-5, 2020.

[18] A. E. Ahmed, W. A. E. Ali, and S. Das, "Quintuple band circular monopole antenna with innovative 3-D printed PLA substrate for wireless applications," *Frequenz*, vol. 76, no. 3-4, pp. 199-207, 2022.

[19] A. E. Ahmed, W. A. E. Ali, and S. Das, "A 3D printed 2x2 circular planar antenna array for wireless communications applications," *Journal of Nano-and Electronic Physics,* vol. 13, no. 3, pp. 03028-1-03028-4, 2021.

[20] I. O. Saracho-Pantoja, J. R. Montejo-Garai, J. A. Ruiz-Cruz, and J. M. Rebollar, "Additive manufacturing of 3D printed microwave passive components," *Emerging Microwave Technologies in Industrial, Agricultural, Medical and Food Processing*, p. 93, 2018.

[21] U. Robles, E. Bustamante, P. Darshni, and R. C. Rumpf, "High-frequency filters manufactured using hybrid 3D printing method," *Progress In Electromagnetics Research M*, vol. 84, pp. 147-155, 2019.

[22] B. Zhang and H. Zirath, "3D printed iris bandpass filters for millimetre-wave applications," *Electronics Letters*, vol. 51, no. 22, pp. 1791-1793, 2015.

[23] T. A. Sheikh, J. Borah, and S. Roy. "Design of compact bandpass filter for WiMAX and UWB application using asymmetric SIRs and DGS," *Radioelectronics and Communications Systems*, vol. 59, no. 6, pp. 269-273, 2016.

[24] T. Firmansyah, M. Alaydrus, Y. Wahyu, E. T. Rahardjo, and G. Wibisono, "A highly independent multiband bandpass filter using a multi-coupled line Stub-SIR With folding structure," *IEEE Access*, vol. 8, pp. 83009-83026, 2020.

Wael A. E. Ali was born in 1982. He received his B.Sc. and M.Sc. in Electronics and Communications Engineering from the Arab Academy for Science, Technology and Maritime Transport (AASTMT), Alexandria, Egypt in 2004 & 2007, respectively. He received his Ph.D. in Electronics and Communications Engineering from Alexandria University, Alexandria, Egypt in 2012. He is now a Professor of Electronics and Communications Engineering, as well as the Head of the Quality Assurance unit in the College of Engineering and Technology.

Ahmed A. Ibrahim was born in 1986. He received his B.Sc. degree, M.Sc., and Ph.D. in Electrical Engineering from the Electronic and Communication Engineering Department, Minia University, Elminia, Egypt in 2007, 2011, and 2014 respectively. He is now an Associated Professor at the Electrical Engineering Department in the Faculty of Engineering, Minia University.

Ashraf E. Ahmed is currently a lecturer at the Electronics and Communications Engineering Department, Higher Engineering and Technology, King Marriott Academy (KMA), Alexandria, Egypt. He received his B.Sc. and M.Sc. degrees in Electronics and Communication Engineering from the Faculty of Engineering, Alexandria University, Egypt.

A High-gain, Low-profile Filtering Antenna Based on a Novel Metasurface

Jingci Zhu, Guanmao Zhang*, Zhihang Li, Zonge Che, Juan Yue, Yinhai Feng, Qian Zhang, and Rui Qiu

Institute of Optoelectronics and Electromagnetics Information,
School of Information Science and Engineering, Lanzhou University, Lanzhou 730000, China
*zhanggm@lzu.edu.cn

Abstract **–** In this paper, a filtering antenna based on a metasurface is designed using slot-coupled feeding, and the metasurface unit is a fractal pattern. Replacing the rectangular patch on the metasurface with a fractal patch can introduce a radiation zero point on the upper sideband of the antenna, thereby enhancing the sideband selectivity. In addition, the current is reversed by loading shorting pin, and a radiation zero point is also introduced in the lower sideband. After measurement, the -10 dB impedance bandwidth of the filtering antenna is 23.6% (3.22-4.08 GHz), and the average antenna gain in the passband is 8.1 dBi. The filtering antenna does not involve an additional filter circuit, has a simple structure, and a small size, and ideally eliminates insertion loss. To verify, the real object was made and tested and found that the reflection coefficient, pattern, gain, etc. were in good agreement with the simulation results, it can be applied to the 5G communication frequency band.

Index Terms **–** 5G communication, filtering antenna, fractal structure, low profile, metasurface.

I. INTRODUCTION

In recent years, with the gradual development of portable mobile communication equipment, the miniaturization and integration of radio frequency front-end devices have become a research focus. The high-efficiency integrated design of the filter and the antenna can obtain a filtering antenna with good out-of-band suppression and high gain [1]. It integrates filtering and radiation functions and reduces the in-band loss caused by the mismatch between the filter and the antenna [2]. Therefore, the design of high-performance filtering antennas has very important practical significance for the further development of microwave circuit systems.

For example, in [3], the dual-mode rectangular SIW cavity is used as a high-Q common resonant cavity for the two bands, and then the filtering antenna is designed by using the orthogonally polarized SL cavity as the radiating element. However, this type of method requires multiple resonators to achieve filtering, which will occupy a large area and cause additional loss, thereby reducing antenna efficiency [4–6]. In [7], the transition structure from the micro-strip to the suture is used as the feed network of the antenna, and the planar dipole is used as the radiator. The filtering response is obtained by adding non-radiating elements to the feed network. Although these methods of adding parasitic bands on the feed network and adjusting the shape of the coupling hole to obtain the filtering effect avoid additional circuits, they still bring additional losses to a certain extent [8–11]. In addition, adding appropriate structures (such as etching grooves or adding short pins, parasitic bands, parasitic patches, etc.) to the antenna to insert the edge radiation zeros point can also achieve filtering characteristics [12–15]. Nowadays, metamaterials are widely used in some antenna designs due to their unique electromagnetic properties. Among them, compared with three-dimensional structural materials, metasurface has a smaller volume and lower loss and can be used in the design of high-performance antennas [16–18]. In [19], a series of non-uniform metal patches are used as the upper metasurface of the antenna, and the current misphase on the inner and outer sheets will produce a radiation zero point near the edge of the upper band. In [20], the researchers etched U-shaped gaps on the metasurface of the unit and loaded defective ground structures (DGS) on the ground to generate low-frequency radiation zeros. Therefore, a well-designed metasurface antenna can generate radiation zero points near the sidebands, thereby obtaining a low-profile, wide-band, and high-gain filtering antenna. Fractal geometry is introduced to design compact or multi-band electromagnetic structures due to the interesting features of space-filling and self-similarity [21]. Reasonable use of fractal structure can effectively improve the performance of microwave equipment, such as designing selective and compact antennas [22, 23].

To realize a better filtering response, in this paper, modifications are introduced both in the design of the metasurface and feeding circuit. Replacing the rectangular patch on the metasurface with a fractal patch can introduce a radiation zero point in the upper sideband of

Submitted On: June 16, 2022
Accepted On: January 2, 2023

https://doi.org/10.13052/2022.ACES.J.371106

the antenna. In addition, by loading a short PIN near the center of the ground to reverse the current on the surface of the patch, a radiation zero point can also be introduced in the lower sideband. To make the antenna exhibit good stop-band characteristics near high frequencies, it is also necessary to suppress its high-order modes, which can be achieved by adding stub micro-strip feeders and separation slots.

II. ANTENNA DESIGN AND ANALYSIS

Figure 1 is a schematic diagram of the three-dimensional structure of the designed filtering antenna. The filtering antenna is composed of a fractal metasurface and a feed network. The metasurface is set on the upper surface of the first layer of medium, the upper surface of the second layer of medium is a grounding plate with a rectangular gap, and the lower surface is a micro-strip feeder. Fig. 2 shows the configuration of the proposed filtering antenna. The optimized parameters of the antenna are shown in Table 1. Based on the slot-coupled micro-strip antenna, it adds stubs on the micro-strip feeder and separates the slots to suppress unwanted resonance modes in the antenna, thereby achieving a filtering effect. The simulation and analysis for the proposed filtering antenna are performed using the electromagnetic simulator ANSYS HFSS.

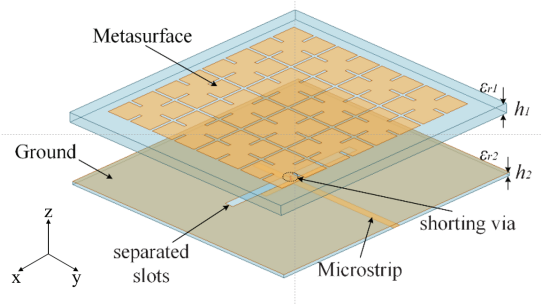

Fig. 1. The three-dimensional structure diagram of the proposed filtering antenna.

Table 1: Design parameters of the filtering antenna

Parameters	L_1	L_2	L_3	r
Values (mm)	18.85	10.7	8.525	0.2
Parameters	W_1	W_2	W_3	d
Values (mm)	2.5	1.95	1.8	0.2
Parameters	a	g	L	S
Values (mm)	6.5	0.8	70	0.8
Parameters	h_1	h_2	ε_{r1}	ε_{r2}
Values (mm)	2.6	0.813	2.2	3.38

To properly display the design concept of this filtering antenna, the following will analyze the mechanism of the antenna filtering response through five antenna structures.

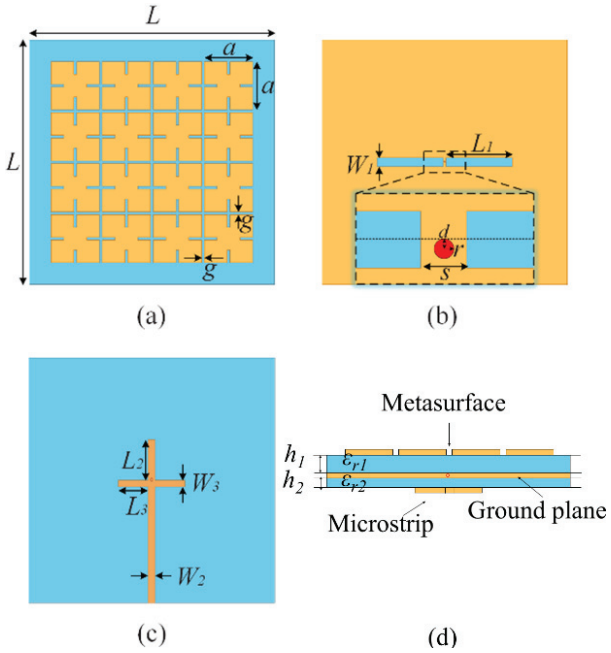

Fig. 2. Configurations of the proposed filtering antenna. (a) Metasurface. (b) Ground plate. (c) Feeder. (d) Side view.

The five structures are as follows: (I) The upper layer is a metasurface of the uniform rectangular patch and adopts linear micro-strip coupling feed. (II) Change the rectangular metasurface patches into fractal patches, and the feed structure remains unchanged. (III) The metasurface is made of fractal patches and two branches are added to the feeder. (IV) Separate the groove in the middle of structure III, and the metasurface structure remains unchanged. (V) A metal via is added in the middle of the groove separated in structure IV, and the other parts remain unchanged. Figure 3 lists several structures such as improved metasurfaces and feed networks. Among them, combining (a) and (b) with (c) respectively can get antennas (I) and (II), and combining (b) with (d), (e) and (f) in turn will get antennas (III), (IV) and (V). Simulate their reflection coefficient and gain curve in the electromagnetic simulation software in turn, and analyze the influence of each structural improvement on the antenna performance step by step.

To investigate the properties of the metasurface unit cell, the calculated reflection and transmission coefficients of the metasurface unit cell are shown in Fig. 4. The reflection coefficient magnitude is less than -10 dB in the whole simulation frequency range. On the other hand, the reflection coefficient phase varies from 0° to 180°, and it is close to stability at the working band

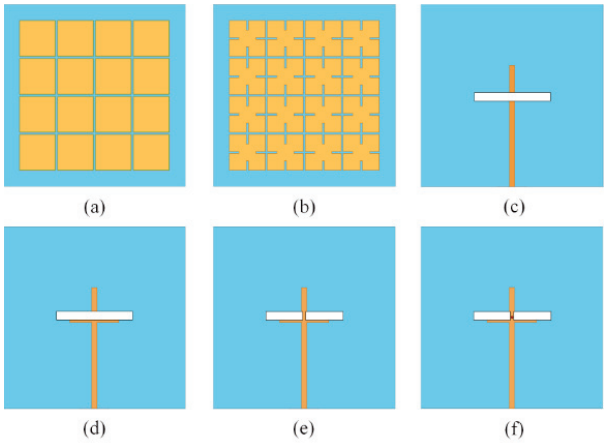

Fig. 3. Several antenna configurations. (a) The rectangular metasurface of Antenna I. (b) Fractal metasurfaces of antennas II, III, IV, and V. (c) Initial feeding circuit of antennas I and II. (d) Two additional arms are added to the linear micro-strip feeder of Antenna III. (e) Antenna IV is fed with two separate slots. (f) Antenna V has an additional shorting via.

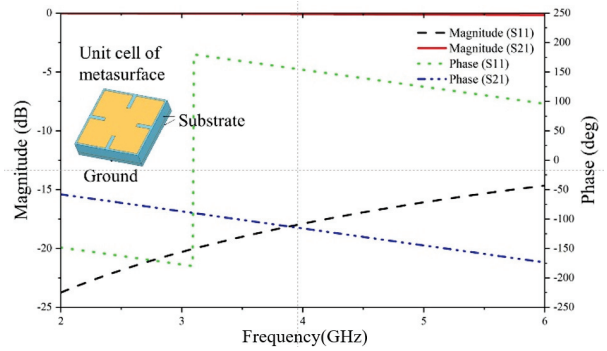

Fig. 4. Simulated reflection and transmission coefficient of the metasurface unit cell.

(3.22-4.08 GHz). It is indicated that the surface wave can propagate along the proposed metasurface.

Figures 5 (a) and (b) are respectively the $|S_{11}|$ and gain simulation curves of the antenna structure I-V. It can be found that with the improvement of the structure, Antenna V finally has a passband between 3.31-4.23 GHz. Compared with Antenna I, Antenna II is only modified from a rectangular metasurface to a fractal structure metasurface; however, the feed structure is the same. Its $|S_{11}|$ curve and gain curve have no change in the low-frequency part, but a weak radiation zero point appears at the frequency of 4.85 GHz. Antenna III has an improved feed structure based on Antenna II. It is found from Fig. 5 (a) that there is only one mode near 4.1 GHz. This shows that adding stubs to the linear feed structure can well suppress the high-frequency resonance mode of the antenna. Next, by adjusting the coupling gap to two separate grooves, the resonance condition of the gap can be destroyed, thereby suppressing the partial resonance near the low-frequency 2 GHz. In the end, the $|S_{11}|$ curve of the Antenna IV becomes smoother at low frequencies, but the sidebands of the curve are not very steep, resulting in poor roll-off characteristics. Try to add a radiation zero point similar to the upper sideband in the lower sideband to enhance its roll-off characteristics to achieve a good filtering effect. Therefore, add a shorting via in the middle of the two slots of Antenna IV to obtain Antenna V. The simulation results showed that it produces three resonance frequency points, and a radiation zero point appears at 3.18 GHz in Fig. 5 (b). Antenna V is the filtering antenna proposed in this paper. The average gain in the passband of the antenna is about 8dBi, there is no other resonance mode outside the band, which meets the design requirements of the filtering antenna.

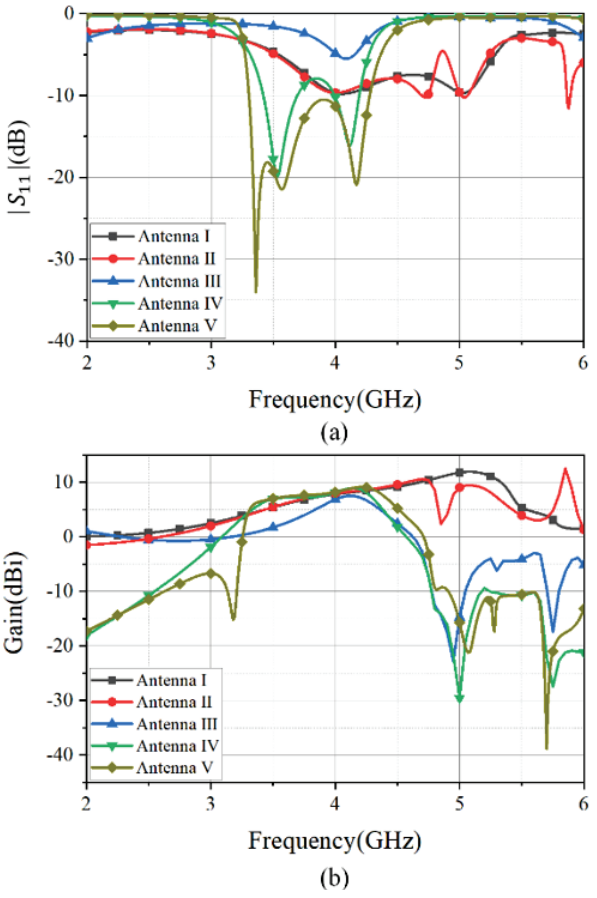

Fig. 5. The reflection coefficient $|S_{11}|$ and gain curves of the proposed five antennas are simulated. (a) $|S_{11}|$. (b) Gain.

To further analyze the generation principle of the antenna filtering response, the current distribution on the metasurface and ground plane of the five antenna

structures is given below. Figures 6 (a) and (b) show the current distribution of the metasurface of Antenna I and Antenna II at 4.85 GHz. Comparing them, the current direction on the rectangular metasurface is approximately the same. The direction of current on the outermost left and right rows of patches on the fractal metasurface is opposite to the direction of current on the two rows of patches in the middle. The radiation of the two can cancel each other, so a radiation zero point will be generated in the upper sideband. Figures 6 (c) and (d) are the current distribution of the ground plate of Antenna II and Antenna III at 4.7 GHz. The current of the Antenna II ground plate is not only concentrated on the micro-strip line but also distributed around the gap. The current of the Antenna III ground plate is only concentrated on the micro-strip line, and there is almost no energy around the gap. Therefore, the analysis shows that after adding the branch, the high-order mode of the antenna is suppressed, so that the rejection of the high-frequency range of the stop band is improved, and a good filtering effect is achieved. Figures 6 (e) and (f) are the current distributions of the metasurfaces of Antenna IV and Antenna V at 3.18 GHz. The current direction at the center of the metasurface of Antenna IV is uniformly downward, and when a shorting via is added at the center position, the current direction of Antenna V at this position is reversed, so a radiation zero point is also generated in the lower sideband.

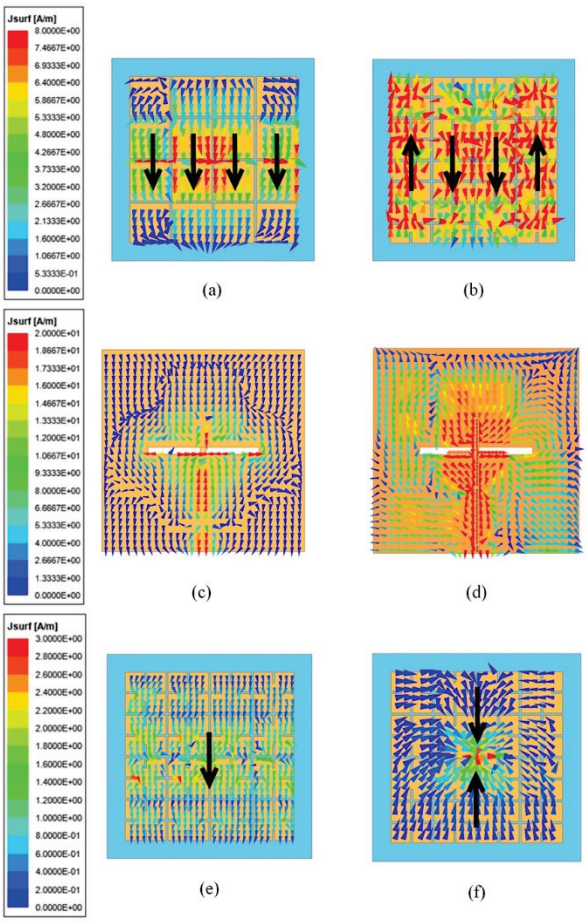

Fig. 6. Surface current distribution of the metasurface /ground plane of the filtering antenna. (a) Metasurface of Antenna I at 4.85 GHz. (b) Metasurface of Antenna II at 4.85 GHz. (c) Ground plane of Antenna II at 4.7 GHz. (d) Ground plane of Antenna III at 4.7 GHz. (e) Metasurface of Antenna IV at 3.18 GHz. (f) Metasurface of Antenna V at 3.18 GHz.

In the above content, the design principle of the filtering antenna is discussed, and then we will analyze the effect of the structural parameters on the performance of the filtering antenna. Figures 7 (a) and (b) show the reflection coefficient and gain of the filtering antenna under different slot lengths. As L_1 increases, the second resonant frequency point of the filtering antenna gradually moves to the low-frequency direction, and finally merges with the first frequency point. With the reduction of the slot length L_1, the out-of-band suppression of the antenna is improved to a certain extent, but the bandwidth is also relatively narrow. Therefore, the length of the gap on the ground plane should be moderate.

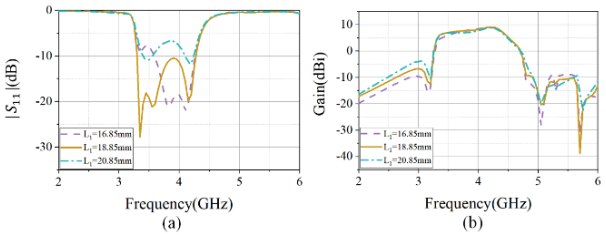

Fig. 7. (a) Simulated reflection coefficient of the filtering antenna for different slot lengths L_1. (b) Simulated gain of the filtering antenna for different slot lengths L_1.

Figures 8 (a) and (b) are simulation curves of the reflection coefficient and gain of the filtering antenna

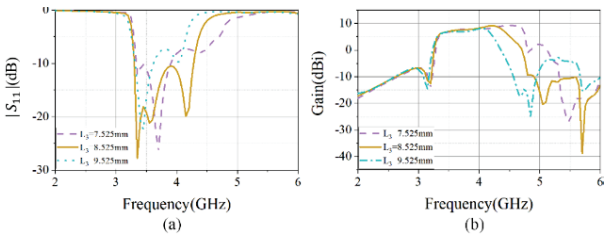

Fig. 8. (a) Simulated reflection coefficient of the filtering antenna for different arm lengths L_3. (b) Simulated gain of the filtering antenna for different slot lengths L_3.

under different arm lengths L_3. When L_3 is smaller, the third resonance mode at the high-frequency shifts to higher frequencies, and when it is larger, the working frequency band of the filtering antenna becomes narrower and partly above -10 dB. Therefore, an appropriate length of the short arm should be selected in the design process to ensure that the high-order mode of the antenna can be suppressed without affecting its bandwidth.

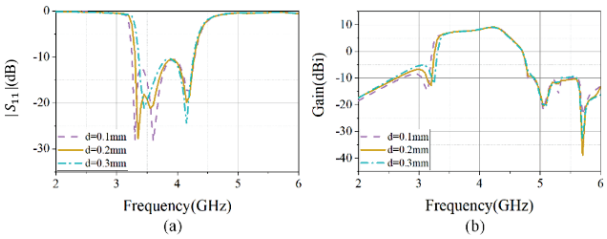

Fig. 9. (a) Simulated reflection coefficient of the filtering antenna for different short via positions. (b) Simulated gain of the filtering antenna for different short via positions.

To introduce a radiation zero point in the lower sideband of the antenna, a short via is set in the middle of the antenna separation slot. The location of the via also has a certain impact on the performance of the filtering antenna. Figures 9 (a) and (b) show the simulation curves of the reflection coefficient and gain of the filtering antenna when the distance d between the short via and the horizontal center line of the substrate changes. As the distance *d* increases, it can be seen that the bandwidth of the antenna and the resonance depth of the mode will slightly change, while the gain curve is almost unchanged. Therefore, to ensure processing accuracy and antenna bandwidth, the distance between the short via and the center line should be carefully selected.

III. MEASUREMENT VERIFICATION

To verify the performance of the designed filtering antenna, it was manufactured and tested. As shown in Fig. 10 , the upper metasurface is fabricated on an F4B dielectric substrate with a dielectric constant of 2.2 and a loss tangent of 0.003 (thickness 2.6 mm), and the lower layer uses Rogers 4003C with a dielectric constant of 3.38 and a loss tangent of 0.0027 as the dielectric substrate (thickness 0.813 mm).

The measurement of the proposed filtering antenna is shown in Fig. 11. The return loss was measured by using an Agilent E5071C vector network analyzer. Figure 12 shows the comparison curve between the measured value of the filtering antenna reflection coefficient and the simulated value. It can be seen that the measured curve is slightly shifted to the low frequency compared to the simulated curve. This may be because there is a gap between the two substrates during the physical processing and cannot fit together ideally. In addition, errors may

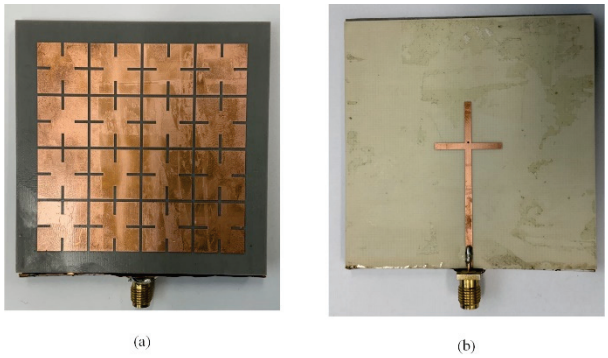

Fig. 10. Photographs of the fabricated filtering antenna. (a) Top view. (b) Bottom view.

Fig. 11. The measurement of the proposed filtering antenna.

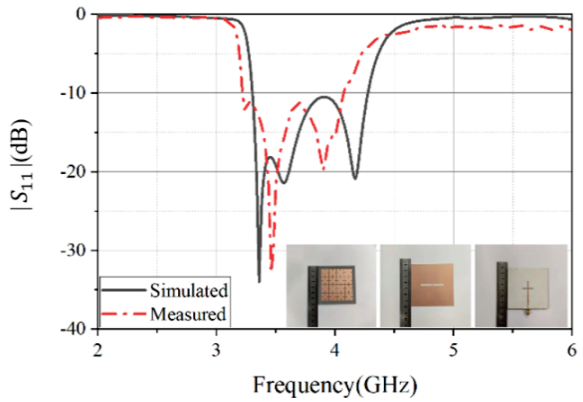

Fig. 12. Simulated and measured reflection coefficients of the filtering antenna.

be introduced during the measurement process, which may also cause deviations between the simulation results and the actual measurement results. The sidebands of the simulated curve and the measured curve are relatively steep, and both show good filtering characteristics. Among them, the measured -10dB impedance bandwidth

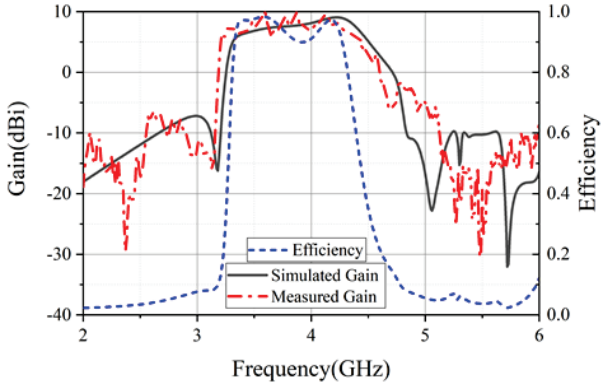

Fig. 13. Simulated and measured the gain of the filtering antenna and efficiency simulation values.

is 23.6% (3.22-4.08 GHz), and the simulated -10 dB impedance bandwidth is 24.4% (3.31-4.23 GHz), and there is not much difference between them. In Fig. 12, the comparison curve between the measured gain value and the simulated value of the proposed filtering antenna and the antenna efficiency is given. It can be seen that although the measured gain curve has a slight jitter compared to the simulated gain curve, the overall consistency is better. In addition, it can be seen that the antenna has a radiation zero point at 3.18 GHz and 5.05 GHz. These two radiation zero points enhance the sideband roll-off of the antenna and bring good edge selectivity. In the range of 3.31-4.23 GHz, the average gain of the filtering antenna reached 8.1 dBi, while the gain dropped rapidly outside the sideband. In the lower stopband range of 2.0-3.18 GHz, the antenna achieves an out-of-band rejection of nearly 17 dB. In the higher stopband range of 5.05-6 GHz, an out-of-band rejection of more than 20 dB is achieved. In addition, the average in-band efficiency of the antenna exceeds 90%, reaching 98.5% at the highest point.

Figure 14 depicts the normalized radiation pattern of the filtering antenna at the three resonance points of 3.35 GHz, 3.60 GHz, and 4.20 GHz. The simulation results are in good agreement with the measured results.

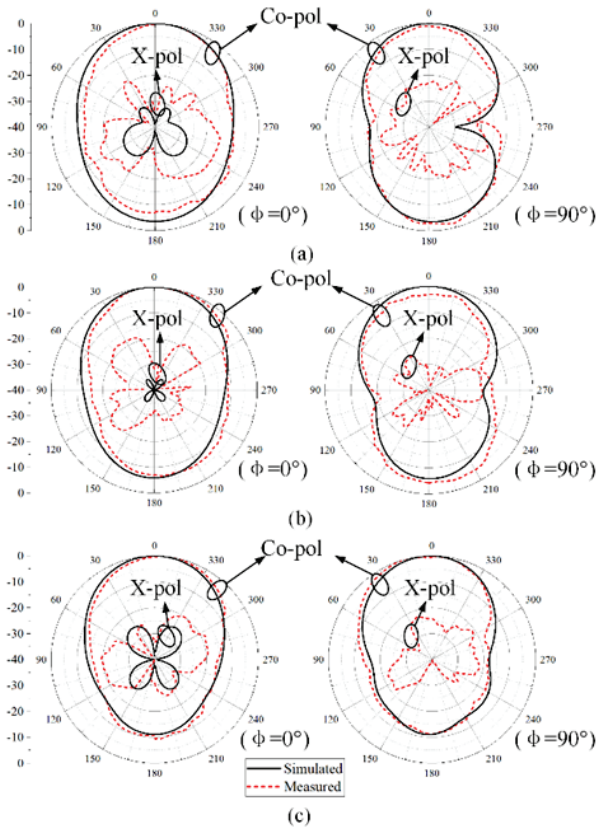

Fig. 14. Simulated and measured normalized radiation patterns of the filtering antenna. (a) The normalized pattern of the filtering antenna at 3.35 GHz. (b) The normalized pattern of the filtering antenna at 3.60 GHz. (c) The normalized pattern of the filtering antenna at 4.20 GHz.

In addition, it can be seen from Fig. 14 that the main polarization of the measured H plane (xz plane) and E plane (yz plane) is approximately 25 dB greater than the cross-polarization. It should be noted that the cross-polarization obtained by simulation is less than -40 dB. The performance comparison between the filtering antenna proposed in this article and other reported filtering antennas is given in Table 2. In contrast, our

Table 2: Comparison between the proposed filtering antenna and some previous works

References	**Center Frequency (GHz)**	**Profile (λ_0)**	**FBW(%)**	**Average Gain (dBi)**	**Suppression Level (dB)**	**Size (λg*λg)**
[8]	4.22	0.078	61.4	8.7	23	0.84*0.84
[12]	4.5	0.098	22.6	7.4	23	0.66*0.66
[15]	2.4	0.032	20.1	9.5	14.5	1.2*1.2
[19]	5	0.06	28.4	8.2	20	1.3*1.3
[20]	7	0.04	17.6	8	17	0.77*0.77
This work	3.35	0.038	23.6	8.1	17	0.78*0.78

proposed filtering antenna based on the fractal metasurface unit achieves a broadband filter response under the condition of low profile ($0.038\lambda_0$). In addition, the antenna has a relatively high gain in the passband and a satisfactory suppression level in the stopband.

IV. CONCLUSION

In this paper, a filtering antenna based on a metasurface is designed by using a slot-coupled feeding mode. The working principle of the antenna is analyzed through the surface current, and the function of each structure of the antenna is explained. The antenna has a good filtering effect. To verify the performance of the filtering antenna, the actual antenna was fabricated and measured. The -10 dB impedance bandwidth measured by the filtering antenna is 23.6% (3.22-4.08 GHz), its structure is compact, and the profile is low. The average gain in the antenna passband is 8.1 dBi and the efficiency exceeds 90%, which can meet the needs of 5G communication. Regardless, future research should be devoted to the development of filtering properties by well-designed fractal metasurface and compacting its structure further.

ACKNOWLEDGMENT

This work was supported by the State Key Program of National Natural Science of China (Grant No. 61631007), the Nation Key R&D Program of China (Grant No. 2019YFA0405403), and the Lanzhou University Innovation and Entrepreneurship Project (Grant No. cxcy202002). In addition, I would also like to thank Prof. Zhonglei Mei and A/Prof. Guoping Gao for their help in measuring instruments during the actual measurement phase.

REFERENCES

[1] Q. Liu, L. Zhu, J. Wang, and W. Wu, "A wideband patch and SIW cavity hybrid antenna with filtering response," *IEEE Antennas and Wireless Propagation Letters*, vol. 19, no. 5, pp. 836-840, 2020.

[2] Y. Li, Z. Zhao, Z. Tang, and Y. Yin, "Differentially fed, dual-band dual-polarized filtering antenna with high selectivity for 5G Sub6 GHz base station applications," *IEEE Trans. Antennas Propagat.*, vol. 68, no. 4, pp. 3231-3236, 2020.

[3] K. Dhwaj, H. Tian, and T. Itoh, "Low-profile dual-band filtering antenna using common planar cavity," *IEEE Antennas and Wireless Propagation Letters*, vol. 17, no. 6, pp. 1081-1084, 2018.

[4] C. X. Mao, S. Gao, Y. Wang, and Z. Cheng, "Filtering antenna with two-octave harmonic suppression," *IEEE Antennas and Wireless Propagation Letters*, vol. 16, pp. 1361-1364, 2017.

[5] L. S. Wu, Y. X. Guo, J. F. Mao, and W. Y. Yin, "Design of a substrate integrated waveguide balun filter based on three-port coupled resonator circuit model," *IEEE Microwave and Wireless Components Letters*, vol. 21, no. 5, pp. 252-254, 2011.

[6] X. J. Lin, Z. M. Xie, P. S. Zhang, and Y. Zhang, "A broadband filtering duplex patch antenna with high isolation," *IEEE Antennas and Wireless Propagation Letters*, vol. 16, pp. 1937-1940, 2017.

[7] Y. Zhang, X. Y. Zhang, and Y. M. Pan, "Low-profile planar filtering dipole antenna with omnidirectional radiation pattern," *IEEE Trans. Antennas Propagat.*, vol. 66, no. 3, pp. 1124-1132, 2018.

[8] P. F. Hu, Y. M. Pan, X. Y. Zhang, and S. Y. Zheng, "Broadband filtering dielectric resonator antenna with wide stopband," *IEEE Trans. Antennas Propagat.*, vol. 65, no. 4, pp. 2079-2084, 2017.

[9] B. J. Xiang, S. Y. Zheng, Y. M. Pan, and Y. X. Li, "Wideband circularly polarized dielectric resonator antenna with bandpass filtering and wide harmonics suppression response," *IEEE Trans. Antennas Propagat.*, vol. 65, no. 4, pp. 2096-2101, 2017.

[10] X. Y. Zhang, Y. Zhang, Y. M. Pan, and W. Duan, "Low-profile dual band filtering patch antenna and its application to LTE MIMO system," *IEEE Trans. Antennas Propagat.*, vol. 65, no. 1, pp. 103-113, 2017.

[11] W. Duan, X. Y. Zhang, Y. M. Pan, J. X. Xu, and Q. Xue, "Dual-polarized filtering antenna with high selectivity and low cross polarization," *IEEE Trans. Antennas Propagat.*, vol. 64, no. 10, pp. 4188-4196, 2016.

[12] W. Yang, Y. Zhang, W. Che, M. Xun, Q. Xue, G. Shen, and W. Feng, "A simple, compact filtering patch antenna based on mode analysis with wide out-of-band suppression," *IEEE Trans. Antennas Propagat.*, vol. 67, no. 10, pp. 6244-6253, 2019.

[13] J. Y. Jin, S. Liao, and Q. Xue, "Design of filtering-radiating patch antennas with tunable radiation nulls for high selectivity," *IEEE Trans. Antennas Propagat.*, vol. 66, no. 4, pp. 2125-2130, 2018.

[14] X. Y. Zhang, W. Duan, and Y. M. Pan, "High-gain filtering patch antenna without extra circuit," *IEEE Trans. Antennas Propagat.*, vol. 63, no. 12, pp. 5883-5888, 2015.

[15] D. Yang, H. Zhai, C. Guo, and H. Li, "A compact single-layer wideband microstrip antenna with filtering performance," *IEEE Antennas and Wireless Propagation Letters*, vol. 19, no. 5, pp. 801-805, 2020.

[16] G. Feng, L. Chen, X. Xue, and X. Shi, "Broadband surface-wave antenna with a novel nonuniform tapered metasurface," *IEEE Antennas and Wireless Propagation Letters*, vol. 16, pp. 2902-2905, 2017.

[17] W. Zhang, Y. Liu, and Y. Jia, "Circularly polarized antenna array with low RCS using metasurface-inspired antenna units," *IEEE Antennas and Wireless Propagation Letters*, vol. 18, no. 7, pp. 1453-1457, 2019.

[18] G. N. Zhou, B. H. Sun, Q. Y. Liang, Y. H. Yang, and J. H. Lan, "Beam Deflection short backfire antenna using phase-modulated metasurface," *IEEE Trans. Antennas Propagat*., vol. 68, no. 1, pp. 546-551, 2020.

[19] Y. M. Pan, P. F. Hu, X. Y. Zhang, and S. Y. Zheng, "A low-profile high-gain and wideband filtering antenna with metasurface," *IEEE Trans. Antennas Propagat*., vol. 64, no. 5, pp. 2010-2016, 2016.

[20] W. Yang, S. Chen, Q. Xue, W. Che, G. Shen, and W. Feng, "Novel filtering method based on metasurface antenna and its application for wideband high-gain filtering antenna with low profile," *IEEE Trans. Antennas Propagat*., vol. 67, no. 3, pp. 1535-1544, 2019.

[21] C. Borja, G. Font, S. Blanch, and J. Romeu, "High directivity fractal boundary microstrip patch antenna," *Electronics Letters*, vol. 36, no. 9, pp. 778-779, 2000.

[22] S. Zheng, Y. Yin, J. Fan, X. Yang, B. Li, and W. Liu, "Analysis of miniature frequency selective surfaces based on fractal antenna–filter–antenna arrays," *IEEE Antennas and Wireless Propagation Letters*, vol. 11, pp. 240-243, 2012.

[23] T. Cai, G. M. Wang, X. F. Zhang, and J. P. Shi, "Low-profile compact circularly-polarized antenna based on fractal metasurface and fractal resonator," *IEEE Antennas and Wireless Propagation Letters*, vol. 14, pp. 1072-1076, 2015.

Jingci Zhu received a B.E. degree in communication engineering from Tianjin University, Tianjin, China, in 2020. He is currently pursuing a master's degree in Information and Communication Engineering at the School of Information Science and Engineering, Lanzhou University. His current research interests are in the area of wireless communications, with a focus on antenna technology, digital pre-distortion linearization (DPD), and spread spectrum system design.

Guanmao Zhang received a B.S. degree from Lanzhou University, Lanzhou, China, in 1995, an M.S. degree in Radio Physics from Lanzhou University in 1998, and the Ph.D. degree in radio physics from Lanzhou University in 2007.

He is currently the director of the Institute of Optoelectronics and Electromagnetic Information, School of Information Science and Engineering, Lanzhou University. His current research interests include surface plasmonics and its communication sensor applications, micro-nano optical device design and application, non-intrusive intelligent photoelectric sensor technology and application, and modern wireless communication technology. At present, he has published more than 40 related academic papers, of which more than 20 are included in SCI/EI.

Zhihang Li received a B.E. degree in communication engineering from Shandong University, Shandong, China, in 2019. He is currently pursuing a master's degree in Electronic and Communication Engineering at the School of Information Science and Engineering, Lanzhou University. His current research interests include frequency selective surfaces, periodic structures, and metamaterial absorbers.

Zonge Che received a B.E. degree in electronic information engineering from Lanzhou Jiaotong University, Lanzhou, China, in 2019. She is currently pursuing a master's degree in Information and Communication Engineering at the School of Information Science and Engineering, Lanzhou University. Her current research interests include terahertz filters, surface plasmonics, metasurface, and metamaterial absorber.

Juan Yue in Communication Engineering from Bohai University, Jinzhou, China, in 2018. She is currently pursuing a master's degree in information and communication engineering at the School of Information Science and Engineering, Lanzhou University. Her current research interests include microstrip filters and metamaterial absorbers.

Yinhai Feng received a B.E. degree in electronic information engineering from Zhengzhou University, Zhengzhou, China, in 2019. He is currently pursuing a master's degree in information and communication engineering at, the School of Information Science and Engineering, Lanzhou University. His current research interests include circularly polarized antennae and multifrequency antennae.

Qian Zhang received a B.E. degree in Electronic Information Engineering from Yantai University, Yantai, China, in 2020. She is currently pursuing a master's degree in Information and Communication Engineering at the School of Information Science and Engineering, Lanzhou University. Her current research interests include surface plasmonics metasurface, periodic structures, and metamaterial absorbers.

Rui Qiu received a B.E. degree in Communication Engineering from Southwest Minzu University, Sichuan, China, in 2021. He is currently pursuing a master degree in electronic and communication engineering, School of Information Science and Engineering, Lanzhou University. His current research interests include Terahertz metalens, vortex beam generator and surface plasmonics metasurface.

Design and Fabrication of Waveguide Slot Antenna Using 3D Printing for 5G Application

Hatem O. Hanoosh[1,2], M. K. A. Rahim[1], N. A. Murad[1], and Yaqdhan M. Hussein[1,3]

[1]Advanced RF & Microwave Research Group (ARFMRG)
School of Electrical Engineering, Faculty of Engineering
Universiti Teknologi Malaysia (UTM), 81310, Malaysia
Hatem.altaee1990@gmail.com, mdkamal@utm.my, noorasniza@utm.my

[2]Department of Computer Techniques Engineering
College of Information Technology, Imam Ja'afar Al-Sadiq University, Samawah, 66001, Al Muthanna, Iraq

[3]Information Technology and Communication (ITC)
Al-Furat Al-Awsat Technical University, Sammawah, Iraq
Yaqthanm79@gmail.com

Abstract – This research constructs a 26 GHz waveguide slot antenna with decent gain. The application of millimeter-wave requires high bandwidth and gain to increase the traffic and users for millimeter-wave and 5G technology. The application of millimeter waves requires a high gain and bandwidth to achieve the requirements of traffic and users increasing for 5G technology and existing millimeter-wave. High-gain and power handling are provided by waveguide slot antennas. Three waveguide structures which are two waveguide antennae and a waveguide horn have been simulated by using CST and fabricated by a 3D printer. The tilt technique has been used with a waveguide to increase the bandwidth and gain of an antenna. A waveguide with broad wall tilt slots has one diction beam while a waveguide with broad and narrow wall tilt slots has two direction beams, each length of the wall enough to distribute six symmetric tilt slots. The gain of 14.3 dB and 1.9 GHz bandwidth are recorded for an antenna with broad wall tilt slots with one beam. While the waveguide with broad and narrow wall tilt slots achieved a gain of 13.9dB and a bandwidth of 1.9 GHz. The proposed antenna is a decent candidate for use with millimeter waves.

Index Terms – 3D printing, add electromagnetic modeling and simulation, multi-beams, slots antenna, waveguide.

I. INTRODUCTION

Millimeter-wave beam-forming networks have become an important part of the Fifth Generation (5G) cellular network, both now and in the future, because they make it easier to pick up signals and can handle more traffic. In this way, a beam-forming network is made up of the beam former, like a common Butler matrix [1], Nolen matrix [2], or Blass matrix [3], and the antenna array that is connected to the beam former [4]. Hence, the antenna is an important device that should provide high gain, wider bandwidth, and high efficiency. In addition, the antenna in a millimeter-wave band requires to provide a low loss, profile, and cost production [5]. Several planar and non-planar antennas have been introduced for millimeter-wave applications to provide high-performance and low profile state of art devices [6–14]. For instance, microstrip antennas for higher frequencies have been presented with different techniques to increase the gain and the bandwidth [6–10]. However, microstrip antennas have the weakness of high losses in terms of merging the antenna module at millimeter-wave frequency. Additionally, the complexity of integration to an antenna array requires a power divider which increases the size and losses accordingly [8]. Hence, researchers shifted to another alternative that can overcome these problems; introducing traditional waveguide antenna structures [10].

The waveguide slot antenna is considered the most common type of waveguide antenna due to, its achieving high gain and low loss properties. At millimeter-wave, waveguide slotted antenna is preferred regarding their size due to the small wavelength at these particular frequencies [11–12]. Commonly, the slots are cut in the broad wall of the waveguide in such a way it affects the electrical fields and the current surface which leads to radiating from the slot cutting [11]. Some studies used

Submitted On: August 8, 2022
Accepted On: January 4, 2023

https://doi.org/10.13052/2022.ACES.J.371107

slot cutting in the narrow wall of the waveguide to operate the antenna. However, a narrow bandwidth resulted [11]. Recently, a slot cutting in both broad and narrow walls with longitude slots distribution is presented in [13, 14]. This technique produces multiple beams with a good gain capability. Nevertheless, the bandwidth obtained is less than 1 GHz, which is not satisfied the millimeter-wave requirements of greater bandwidth than 1 GHz.

Therefore, this paper constructs a high gain and wide bandwidth waveguide slots antenna using tilted slots at both narrow and broad walls of the waveguide structures. The advantage of using a tilted slot is to increase the bandwidth of the antenna. Six slots are selected to be applied on both walls with tilted of 10° to produce dual-beam in the vertical and horizontal direction and increase the impedance bandwidth to more than 1 GHz. The objective of this antenna design is to operate at a center frequency of 26 GHz and provides a high gain $\geq$ 10 dB and bandwidth $\geq$ 1 GHz.

II. WAVEGUIDE SLOT ANTENNA DESIGN

Shunt elements in transmission lines are commonly used to represent slots. Figure 1 shows the circuit for the slot. *G* stands for the slot's conductance, and *B* stands for the slot's susceptance. The waveguide structure's longitude direction is employed to cut the slot used in this study. *L* and *W* are the length and breadth of each slot, respectively. As shown in Fig. 2, d is the distance between two centered slots, and x is the offset from the center line. The d between the slots is calculated to be half the guided wavelength. As a result, the radiating slots would have a 180-degree phase shift [16, 17]. The normalized conductance Gn equations, as shown in Equation (1), are used to calculate the offset x. (1, 2).

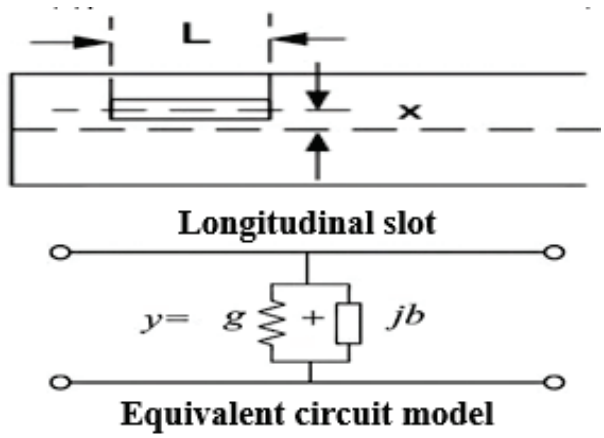

Fig. 1. Slot circuit representations [15].

$$G_n = \sum_{n=1}^{N} \text{gn} = 1, \tag{1}$$

$$g_n = \left[2.09 \frac{\lambda g}{\lambda 0} \cdot \frac{a}{b} \cdot cos^2 \frac{\pi \lambda 0}{2\lambda g}\right] sin^2 \frac{\pi x}{a}. \tag{2}$$

Variables a and b are the inner dimensions of the waveguide (as depicted in Fig. 3), and the free space wavelength is represented by $\lambda 0$ and the guided wavelength is g, while the number of slots is represented by N. The slotted waveguide antenna's physical dimensions, as well as its gain and beamwidth, are determined using the formulae below [17]:

$$\lambda_g = \frac{\lambda 0}{\sqrt{1 - \left(\frac{\lambda 0}{2a}\right)}}, \tag{3}$$

$$Gain = 10 \times log\left(\frac{N.d}{\lambda 0}\right) dB, \tag{4}$$

$$Beamwidth = 50.7 \times \frac{\lambda 0}{\frac{N}{2} \cdot d} degree, \tag{5}$$

$$d = \lambda_g/2, \tag{6}$$

$$L = 0.98\lambda_0/2, \tag{7}$$

$$W = \lambda_g/20. \tag{8}$$

Slot width and length are denoted by W and L, respectively, while the distance between slots is represented by d. Equation (3) shows how to derive the slot parameters from the operating frequency and wavelength of the guided center. Furthermore, two critical parameters, the number of slots and wavelength influence the gain and beam width. These values are also affected by the distance between slots (d). The gain is increased when the number of slots (N) increases [17]. However, as the guided wavelength (λg) is raised, the distance between slots and the waveguide size is also increased [17]. As a result, the chosen slots are utilized on waveguide walls to retain an optimal gain and a reasonable size. The structure of the waveguide is typically broadcast in TE10 mode, with both the H and E field positioned within the waveguide's broad and narrow walls, as shown in Fig. 2. An incision will be created over H-field lines at maximum flow to enable the slot radiation [17]. This will result in one beam being generated at one of the walls. The slots on each wall side of the waveguide are carved to enable numerous beams (two or more). If the slot cutting is done on the waveguide's narrow and broad walls, for example, a dual beam will be formed in the direction of the cutting slots. Figure 3 depicted the distribution of slots concerning the dimensions of the waveguide structure.

Two rectangular waveguides WR34 antennas are selected to distribute slots. As shown in Fig. 4, the slot

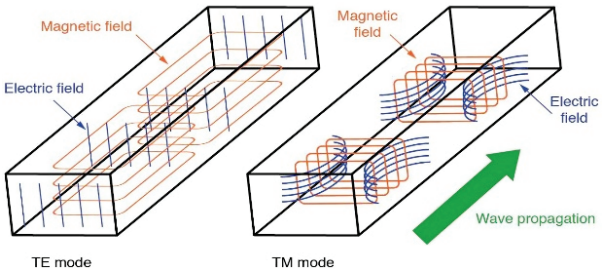

Fig. 2. H and E fields distributed lines in the rectangular hollow waveguide [17].

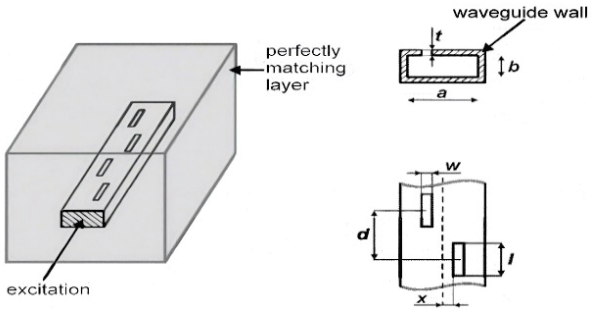

Fig. 3. The standard structure of the waveguide slots antenna [11].

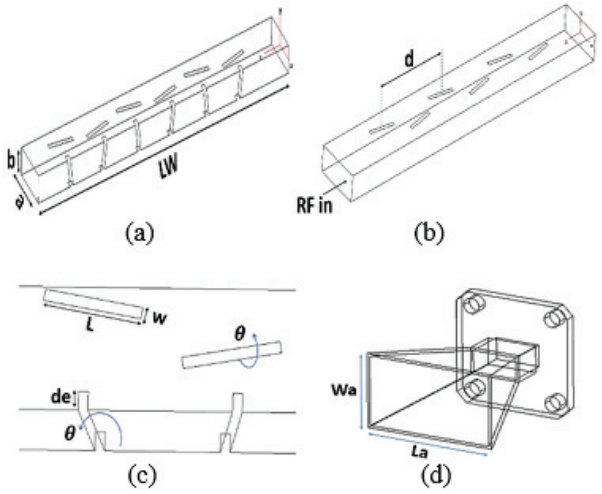

Fig. 4. Proposed waveguide slots tilted antenna. (a) Broad and narrow wall slots. (b) Broad wall slots. (c) Depth and angle. (d) Horn antenna.

is spread on a broad and narrow wall with a tilt angle (θ) that is spun around the slot's center. The slots are cut symmetrically into the broad and narrow walls of the waveguide by the transverse current when the mode is TE10. As seen in Fig. 4, the horn antenna is based on the WR34 waveguide technology standard. As a result, Table 1 summarizes the intended antenna size in lambda.

Table 1: A dimensions of the proposed antenna

Parameters	Describe	Value
a	Broad wall	0.75 λ
b	Narrow wall	0.35 λ
LW	Length of waveguide	5.2 λ
L	Length of slot	0.46 λ
d	distance between slots	0.63 λ
W	Width of slot	0.052 λ
La	Length of aperture	2.17 λ
Wa	Width of aperture	1.52 λ
de	depth	0.086 λ
θ	Angle of slots	$\pm$10 degree

III. DISCUSSION BASED ON PARAMETRIC STUDY

The performance of the reflection coefficient was investigated using the CST program. The design of this proposed antenna used waveguide standard technology which is WR34. The reflection coefficient of the proposed design depended on an angle(θ) and depth of slots, Fig. 5 depicted the responses of the reflection coefficient, it can be determined when the angle (θ) is changing from 0° to 15°, the bandwidth increases and the frequency is adjusted at 26 GHz at the optimum slot angle of 10°. The bandwidth stays the same when the slot depth of the narrow wall alterations from 0 to 1 mm, however, the frequency is increasing and the frequency is shifted as in Fig. 6.

Based on these findings, the ideal scenario for achieving satisfactory outcomes is to employ a slot angle and depth of 10° and 1 mm, respectively.

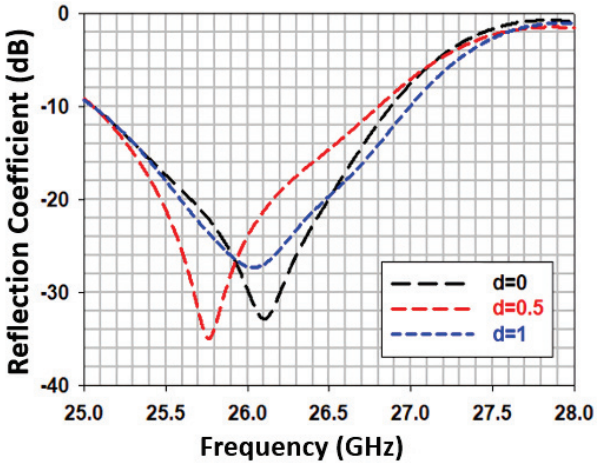

Fig. 5. Titled slot versus reflection coefficient.

In the fabrication process, the designed antenna is metal-produced using 3D printer material. The ALSi9

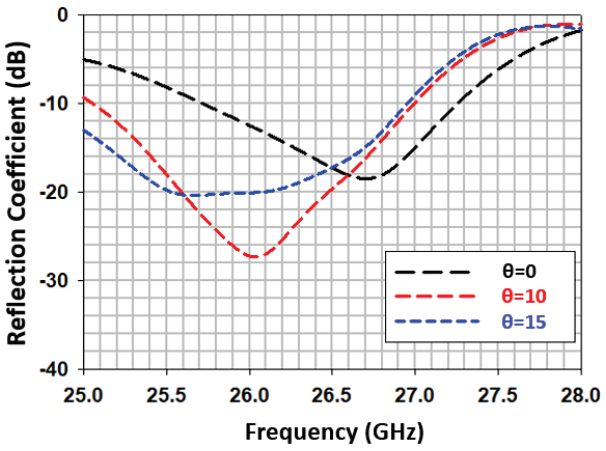

Fig. 6. Slot depth versus reflection coefficient (θ =10 degrees).

material has a high casting ability, is tailored for high electrical conductivity, and has outstanding weather resistance. Figure 7 shows a prototype 3D printed off two waveguide antennas, one with title slots on both the broad and narrow walls, and the other with title slots exclusively on the broad wall, in addition to a horn antenna that was also designed using a 3D printer. Using the R&S®ZNB40 VNA, the performance of the suggested antennas is measured in terms of S-parameters (dB) and radiation pattern. A horn antenna was utilized as a reference in the radiation patterns measurement setup, which was placed in both the E-plane and H-plane directions of the tested antenna.

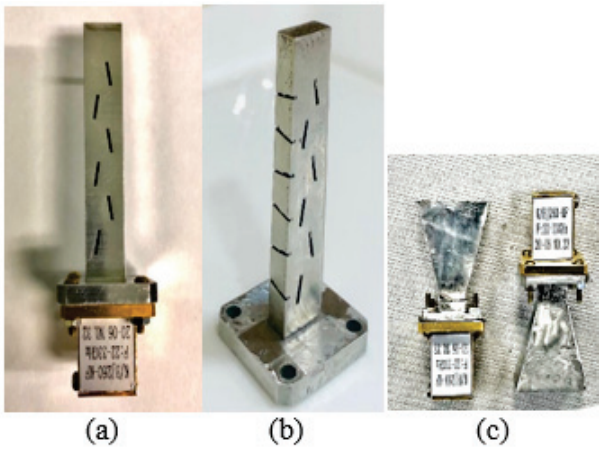

Fig. 7. Fabrication of proposed design. (a) Broad wall slots. (b) Broad and narrow wall slots. (c) Horn antenna.

IV. SIMULATION AND TESTING

Figure 8 shows the comparison results of the reflection coefficient between the simulation and measurement of two waveguide antennas, the measured reflection coefficient of the waveguide antenna with tilt slot on broad is shifted to a higher frequency which is 28.4 GHz while the measured reflection coefficient of waveguide antenna with tilt slot on the broad and narrow wall has Hugh bandwidth started from 22 GHz to 30 GHz which coverage the certain frequency 26 GHz. As can be seen in Fig. 9, the measured reflection coefficient of the waveguide horn antenna is still less than -10 dB with a wider bandwidth.

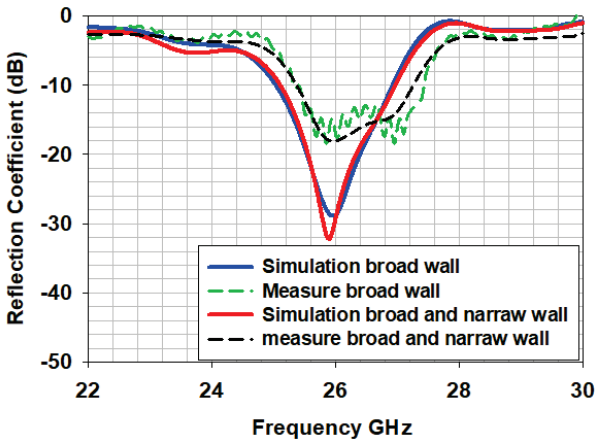

Fig. 8. Comparison reflection coefficient of two waveguide antennae.

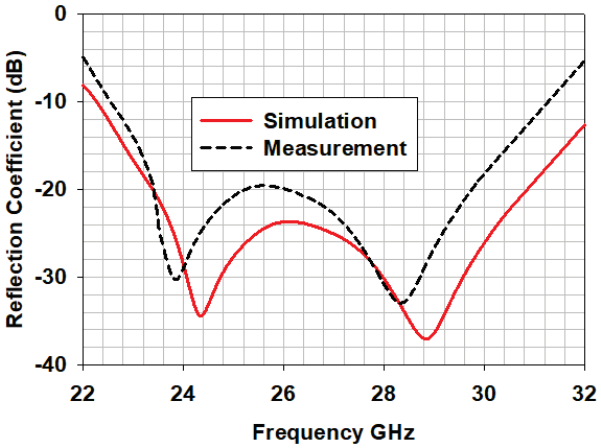

Fig. 9. Comparison reflection coefficient of waveguide horn.

The front-end module's efficiency and gain performance are then shown in Fig. 10. When the line is a curve-fitting result, the measured gains of the front-end module have frequency dependencies ranging from -180 to 180 degrees. Waveguide antennas achieved higher gains of more than 13 dB for each antenna, and the idealization of efficiency for each antenna achieved higher

efficiency of 99 percent at 26 GHz, according to the fitting curve.

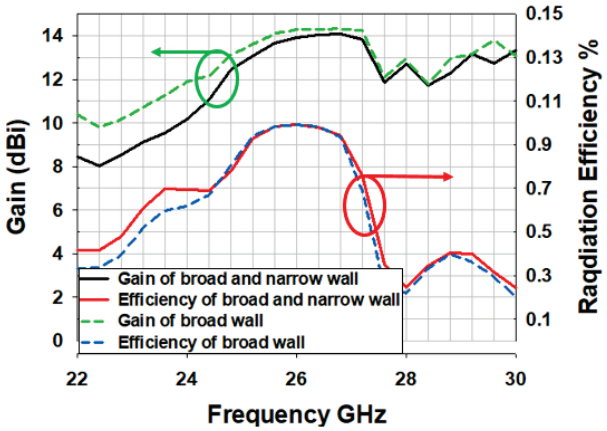

Fig. 10. Gain and efficiency performance.

Figure 11 depicts the designed antenna's radiation pattern in both implemented walls. The comparison of directivity between measurement and simulation at 26GHz in a broad wall at 0° also explains the directivity of a narrow wall as measurement and simulation of design at 26 GHz, this enables the beam to radiate at a 90° angle. The slide lobes levels concerning the back lobe levels are less than -5dB, designed with a broad and narrow wall tilt slot that has dual-beam perpendicular to each other with phase spacing between two beams of 90°. Figure 12 (a) shows the 2D radiation pattern of the antenna with a broad tilt slot only as measurement and simulation radiate at 26 GHz at a 0° angle. Figure 12 (b) shows the 2D radiation pattern of the horn as measurement and simulation has a very directive beam at 26 GHz at a 0° angle. Figure 13 refers to the measurement antenna in the champter room.

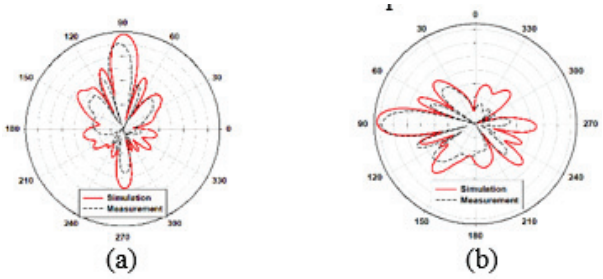

Fig. 11. 2D radiation pattern of an antenna with broad and narrow wall tilt slot, (a) broad wall, (b) narrow wall.

Normally, the antenna's 3D radiation pattern is formed by the edges of the patch, but in the case of waveguides, the majority of the radiation pattern is formed by the slots of the main structure, as shown in

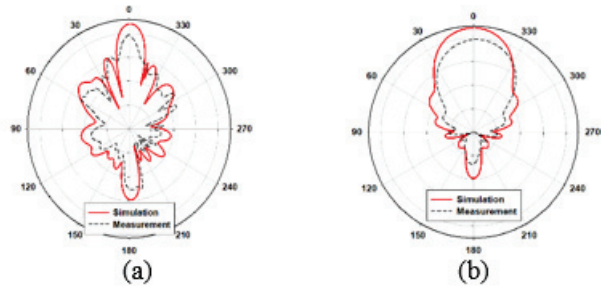

Fig. 12. Depicts the 2D radiation pattern of the antenna concerning the broad wall tilt slot and horn. (a) Broad wall only and horn. (b) Horn.

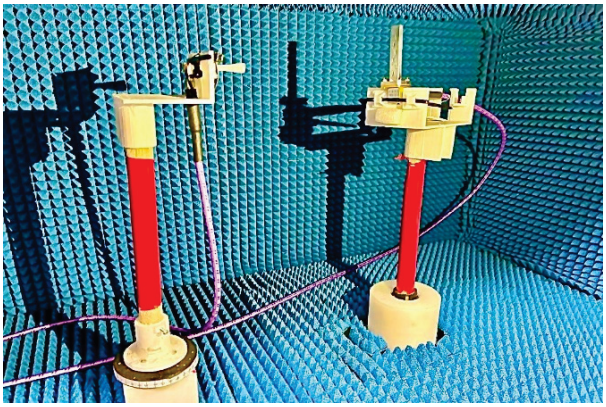

Fig. 13. Measurement antenna in champter room.

the simulated 3D radiation pattern in Fig. 14 below. The 3D radiation pattern of the design with broad and narrow

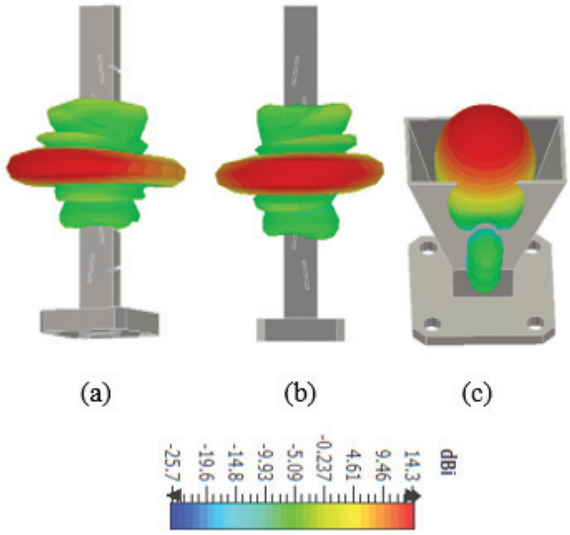

Fig. 14. 3D radiation. (a) Broad and narrow tilt slots. (b) Broad tilt slots. (c) Horn.

wall tilt slots and an antenna with only broad tilt slots in addition to the horn structure.

Figure 15 illustrates the surface current of three designs, it shows clearly the radiation of waveguide antenna with broad and narrow comes from tilt slots on a broad and narrow wall, in addition, the radiation of the second design which is a waveguide with board tilt slots only come from slots, slots consider as a source for radiation. The third design which is horn radiation comes from its aperture. Table 2 shows a comparison of the proposed design with existing work on dual-frequency band millimeter-wave antennas.

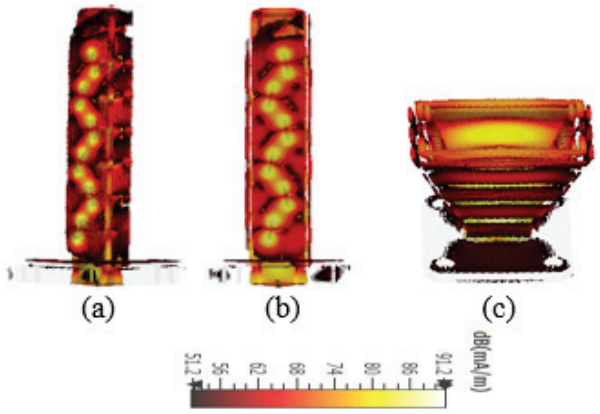

Fig. 15. Surface current, (a) broad and narrow tilt slots, (b) broad tilt slots, (c) horn.

Table 2: Proposed design versus previous works

No. Ref	Freq	No. Beam	BW	Gain	No. Slot
19	30	2	1.5	13.3	8
20	28	2	0.75	14.4	8
This work	26	2	1.9	13.9	6

V. CONCLUSION

This paper presents a wideband and high gain waveguide slotted tilt antenna at 26 GHz. Both narrow and broad walls are tilted by 10° and the depth used with the narrow wall is 1 mm. This constructed model increases the bandwidths' impedance. The length of each structure has six symmetric tilt slots. The reflection coefficient of the waveguide with tilt slots on the broad wall resonates as simulation at 26 GHz of -28 dB and as measurement shifted to 28.3 GHz of -15 dB. The reflection coefficient of the waveguide with tilt slots on broad and narrow walls resonates as simulation at 26 GHz of -38 dB and measurement at 26 GHz of -18 dB and produces dual beams. A waveguide with tilt slots on a broad wall achieved a gain of 14.3 dB and a bandwidth of 1.9 GHz an additional efficiency of 99% while a waveguide with tilt slots on broad and narrow walls achieved a gain of 13.9 dB and a bandwidth of 1.9 GHz with an efficiency of 99%. The proposed antenna is a decent candidate for use with millimeter waves in 5G applications. In the future, we will change the slot to a zigzag slot to increase the gain.

ACKNOWLEDGMENT

The authors would like to thank the Ministry of Higher Education (MOHE), School of Postgraduate Studies (SPS), Research Management Centre, Advanced RF, and Microwave Research Group, School of Electrical Engineering and Universiti Teknologi Malaysia (UTM), Johor Bahru, for the support of the research under Grant 09G19 and FRGS/1/2021/TKO/UTM/01/7 .

REFERENCES

[1] A. Tajik, A. S. Alavijeh, and M. Fakharzadeh, "Asymmetrical 4 × 4 Butler matrix and its application for single layer 8 × 8 Butler matrix," *IEEE Transactions on Antennas and Propagation*, vol. 67, no. 8, pp. 5372-5379, 2019.

[2] H. Ren, H. Zhang, P. Li, Y. Gu, and B. Arigong, "A novel planar Nolen matrix phased array for MIMO applications," *IEEE International Symposium on Phased Array System & Technology (PAST)*, Waltham, MA, USA, 2019.

[3] P. Chen, W. Hong, Z. Kuai, and J. Xu, "A double layer substrate integrated waveguide blass matrix for beamforming applications," *IEEE Microwave and Wireless Components Letters*, vol. 19, no. 6, pp. 374-376, 2009.

[4] R.-S. Chen, G.-L. Huang, S.-W. Wong, M. K. T. Al-Nuaimi, K.-W. Tam, and W.-W. Choi, "Bandwidth-enhanced circularly-polarized slot antenna and array under two pairs of degenerate modes in a single resonant cavity," *IEEE Antennas and Wireless Propagation Letters*, 2022. doi: https://doi.org/10.1109/LAWP.2022.3209494.

[5] H. Park, G. Namgung, C. Lee, J. Kwon, and S. Kahng, "A small real-estate platform for 5G beamforming/beam-steering antennas shared with WBAN UHF-band MIMO antennas," *International Symposium on Antennas and Propagation (ISAP)*, Busan, Korea (South), pp. 1-2, 2018.

[6] Y. M. Hussein, M. K. A. Rahim, and N. A. Murad, "Substrate integrate waveguide and microstrip antennas at 28 GHz," *Bulletin of Electrical Engineering and Informatics*, vol. 9, no. 6, pp. 2462-2468, 2020.

[7] X. Xia, Q. Wu, H. Wang, C. Yu, and W. Hong, "Wideband millimeter-wave microstrip reflectarray using dual-resonance unit cells," *IEEE Antennas and Wireless Propagation Letters*, vol. 16, pp. 4-7, 2017.

[8] Y. M. Hussein, M. K. A. Rahim, N. A. Murad, H. O. Hanoosh, and N. B. M. Nadzir, "Substrate integrated waveguide antenna at millimeter wave for 5G application," *Applied Computational Electromagnetics Society (ACES) Journal*, vol. 37, no. 04, pp. 478-484, 2022.

[9] G. Sun and H. Wong, "A planar millimeter-wave antenna array with a pillbox-distributed network," *IEEE Transactions on Antennas and Propagation*, vol. 68, no. 5, pp. 3664-3672, 2020.

[10] D. J. Bisharat, S. Liao, and Q. Xue, "High gain and low cost differentially fed circularly polarized planar aperture antenna for broadband millimeter-wave applications," *IEEE Transactions on Antennas and Propagation*, vol. 64, no. 1, pp. 33-42, 2016.

[11] H. O. Hanoosh, M. K. A. Rahim, N. A. Murad, and Y. M. Hussein, "Multi-beams waveguide slot antennas at X-band for wireless communications systems," *Applied Computational Electromagnetics Society (ACES) Journal*, vol. 35, no. 7, pp. 797-802, 2020.

[12] R. V. Gatti and R. Rossi, "A dual-polarization slotted waveguide array antenna with polarization-tracking capability and reduced sidelobe level," *IEEE Transactions on Antennas and Propagation*, vol. 64, no. 4, pp. 1567-1572, 2016.

[13] Y. F. Wu and Y. J. Cheng, "Conical conformal shaped-beam substrate-integrated waveguide slot array antenna with conical-to-cylindrical transition," *IEEE Transactions on Antennas and Propagation*, vol. 65, no. 8, pp. 4048-4056, 2017.

[14] H. O. Hanoosh, M. K. A. Rahim, N. A. Murad, and Y. M. Hussein, "High gain waveguide tilted slot antenna for millimeter wave application," *IEEE International Symposium on Antennas and Propagation and USNC-URSI Radio Science Meeting (APS/URSI)*, pp. 125-126, 2021. doi: https://doi.org/10.1109/APS/URSI47566.2021.9703881.

[15] D. S. Ramkiran, B. T. P. Madhav, K. Narasimha Reddy, S. Shabbeer, Pr. Jain, and S. Sowmya, "Coplanar wave guide fed dual band notched MIMO antenna," *International Journal of Electrical and Computer Engineering (IJECE)*, vol. 6, no. 4, p. 1732-1741, 2016.

[16] R.-S. Chen, X.-D. Li, H.-L. Liu, G.-L. Huang, S.-W. Wong, M. K. T. Al-Nuaimi, K.-W. Tam, and W.-W. Choi, "Reconfigurable full-metal circularly-polarized cavity-backed slot antenna and array with frequency and polarization agility," *IEEE Transactions on Circuits and Systems II: Express Briefs*, vol. 70, no. 2, pp. 531-535, Feb. 2023.

[17] R. S. Elliott, *Antenna Theory and Design*, Revised Edition, John Wiley & Sons, New York, USA, pp. 305-315, 2017.

[18] Muataz W. Sabri, Noor A. Murad, and M. K. Rahim, "Bi-directional beams waveguide slotted antenna at millimeter wave," *TELKOMNIKA*, vol. 16, no. 4, pp. 1515-1521, Aug. 2018.

[19] M. W. Sabri, N. A. Murad, M. K. A. Rahim, "Highly directive 3D-printed dual-beam waveguide slotted antennas for millimeter-wave applications," *Microw Opt Technol Lett.*, © 2019 Wiley Periodicals, Inc., pp. 1-8, 2019.

Hatem O. Hanoosh was born in Samawah, Iraq, in 1991. He received the B.S. degree in computer techniques engineering in 2014-2015 from Islamic University College, Najaf City. He received the M.S. degree in electronic engineering (telecommunication system) from University Technical Malaysia Melaka (UTEM), Malaysia, in 2018, respectively, and he is currently working toward the Ph.D. degree in electronic engineering with University Technology Malaysia (UTM), Johor Bahru City. His current research interests include millimeter-wave antennas, base station antennas, waveguide slot antennas and Nolen matrix.

M. K. A. Rahim received the B.Eng. degree in electrical & electronics from the University of Strathclyde, U.K., in 1987. He received the M.Eng. degree in science from the University of New South Wales, Australia, in 1992 and the Ph.D. degree in electrical engineering from University of Birmingham, U.K., in 2003.He is a Professor in RF & Microwave and Antenna at School of Electrical Engineering, Universiti Teknologi Malaysia. His research interest includes the areas of radio frequency, microwave and antennas. He has been awarded with top research publication in 2015, 2017, and 2020. In 2018, he was honored as "Tokoh Penyelidik" at CITRA KARISMA UTM, and in the same year, he was awarded with Top Research Scientist Malaysia (TRSM) award by Academy Science of Malaysia.

N. A. Murad received her first degree, Bachelor of Engineering (Electrical – Telecommunications), in 2001 from Universiti Teknologi Malaysia (UTM). Shortly after graduation, she served UTM as a tutor. She graduated with Master of Engineering (Electrical) in 2003 from the same university and has been appointed as a Lecturer in April 2003. She joined Emerging Device Technology Group, University of Birmingham, U.K., and obtained the Ph.D. degree in 2011 for research on micromachined millimeterwave circuits. She attached to HID GLOBAL Sdn Bhd for one year under Research and Development specifically working on RFID tag design, testing, and development. Her research interests include antenna design for RF and microwave communication systems, millimeter-wave circuits design, RFID, and antenna beamforming. Currently, she is a senior member of IEEE (MIEEE), MBOT Professional Technologist, and an Associate Professor with the School of Electrical Engineering, Universiti Teknologi Malaysia (UTM).

Yaqdhan M. Hussein was born in Samawah, Iraq, in 1991. He received the B.S. degree in computer techniques engineering in 2014-2015 from Islamic University College, Najaf city, and the M.S. degree in electronic engineering (telecommunication system) from Universiti Teknikal Malaysia Melaka (UTeM), Malaysia, in 2018, respectively, and he is currently working toward the Ph.D. degree in electronic engineering with Universiti Teknologi Malaysia (UTM), Johor Bahru city. His current research interests include millimeter-wave antennas, base station antennas, and SIW technology with butler matrix.

Millimeter-wave Wideband High-isolation Antenna Array Based on End-fire Magnetoelectric Dipole Antenna for 5G Applications

Fang-Fang Fan, Qing-Lin Chen, and Kai Qin

The Key Laboratory of Antennas and Microwave Technology
Xidian University, Xi'an 710071, China
fffan@mail.xidian.edu.cn, 929938860@qq.com, qkqinkai@foxmail.com

***Abstract* –** In this paper, a millimeter-wave (mmW) wideband high-isolation wide-angle scanning antenna is presented. The end-fire magnetoelectric (ME) dipole with wideband impedance characteristic and wide beamwidth is selected. Based on the ME dipole, a 1×4 subarray with a stripline feed network is constructed to get higher antenna efficiency. Then, four 1×4 subarrays are adopted to form a 4×4 array to realize the wide-angle scanning performance. Furthermore, to get better isolation between the subarrays, the beam is tilted on the non-scanning plane; in addition, the resonant split rings are added on the background of the subarrays. With these two measures, the isolation between the subarrays can be effectively reduced, with more than 20 dB over the entire bandwidth. Owing to the wide beamwidth of ME dipole and high isolation between the subarrays, the 4×4 array can obtain the wide-angle scanning characteristic. The final antenna covers an operating bandwidth of 19.5% (24.25-29.5 GHz) with return loss more than 10 dB, which can meet the band in the 5G standard. The beam can scan approximately ±55° with a realized gain reduction under 3 dB within the wide operating bandwidth. Also, the simulated radiation efficiency of the array is more than 77% over almost the entire band. The antenna will be a potential candidate to be applied in 5G applications.

***Index Terms* –** fifth generation (5G), high-isolation, magnetoelectric (ME) dipole, wide-angle scanning, wide bandwidth.

I. INTRODUCTION

Nowadays, with the rapid development of wireless communication, millimeter-wave (mmW) antenna systems have played an important role and been widely used in mobile communication, driverless cars technology, internet of things and other fields because of its high data rate, low response time and wide operating bandwidth. Promoting the development of the fifth-generation (5G) wireless communication, mmW wideband, high isolation and wide-angle scanning phased array antennas are urgently required, especially those that work in 5G band.

During the past few years, many kinds of wideband mmW antenna arrays based on different structures have been designed, such as tapered slot antenna [1], meta-surface antenna [3–4, microstrip patch antenna [5], quasi-Yagi antenna [6], and horn antenna [7]. However, few of them have wide-angle scanning characteristic and high isolation between the elements at the same time. The literature [8–12] show the excellent scanning performance, such as transmitarrays [8], reflectarrays [9], dielectric resonators [10], and lenses [11]. However, the size of these antennas is not suitable to integrate with other devices. In literature [13–17], the wide-angle scanning performance can be obtained, while the port isolation between the elements is not so desirable with only more than 15 dB, even some methods have been employed to reduce the mutual coupling. Thus, designing an antenna possessing wideband, high isolation and wide-angle scanning is still a challenging task. As for the element, magnetoelectric (ME) dipoles show great advantages of wide bandwidth, wide beamwidth, and superior radiation performance by combining complementary electric dipole and magnetic dipole in mmW band [18, 19].

II. ANALYSIS OF THE ANTENNA ELEMENT AND ARRAY

A. ME dipole element

The array antenna element is designed based on the ME dipole in [20]. It is an end-fire ME dipole with wide bandwidth and wide beamwidth, which is a good candidate for the wide-scanning array element. However, it is printed on a single-layer dielectric substrate with the thickness of 0.254 mm, which is too thin to hold the larger array. Moreover, the microstrip feed network would suffer higher transmission loss in mmW band. Thus, two dielectric substrates are employed to get a stripline structure as the feeding network can be seen in Fig. 1, which can meet the requirements of hard structure and low loss.

In Fig. 1 (a), the upper part in the red dashed frame is electric dipole, and the lower part in the blue dashed frame is a single loop antenna, playing the role of mag-

Submitted On: September 29, 2022
Accepted On: December 10, 2022
https://doi.org/10.13052/2022.ACES.J.371108

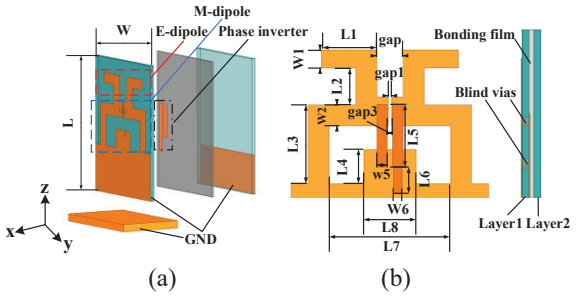

Fig. 1. Configuration of the element. (a) Perspective view. (b) Front view and side view.

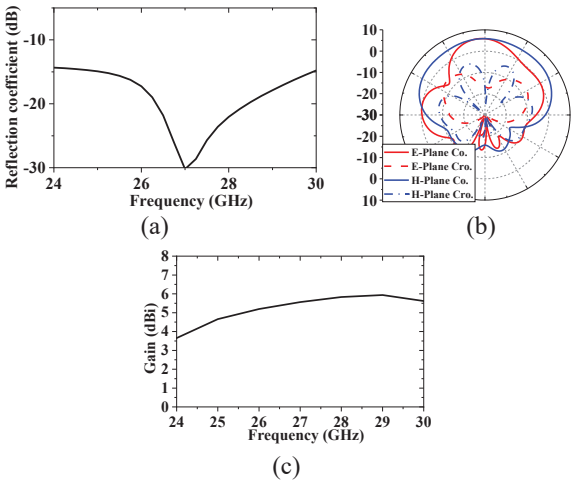

Fig. 2. Simulated results of the proposed antenna element: (a) reflection coefficient, (b) radiation patterns at 27 GHz, (c) radiation gain.

netic dipole. The two antennas are combined together and are excited by a phase inverter, providing 180° phase shift over a broadband range. The electric dipole and magnetic dipole have different resonant frequencies, which broaden the operating frequency of the total antenna. Both of the two substrates used here are Rogers Duroid5880 substrate with thickness of 0.254 mm. On the backside of layer2, a rectangular conductor acts as the stripline's ground. The horizontal copper plate plays the role of reflecting beam and fixing antenna substrate. From the side view of Fig. 1 (b), a bonding film (Rogers 4450F, εr=3.5, tanδ=0.004) with a thickness of 0.2 mm is used to align the two substrates together. All the dimensions of the ME dipole are marked in Fig. 1 (b). After the mass simulation analysis and optimization, the element exhibits outstanding performance as shown in Fig. 2, over the frequency range of 24-30 GHz, the simulated return loss is larger than 15 dB. The realized gain is more than 4 dBi and the maximum realized gain is up to 5.9 dBi over the band 24.25-29.5 GHz. The simulated realized gain radiation pattern at the center frequency 27 GHz in Fig. 2 (b) shows that the cross polarization in the E-plane and H-plane is higher than 25 dB in the broadside direction. The 3 dB beamwidth is 154° at 27 GHz in H-plane, which is advantageous for wide-angle scanning. That is to say, the two layers substrate ME dipole also can be a good element candidate for the phase array application because of the wide impedance bandwidth and wide beamwidth in H-plane. The dimensions of the element are shown in Table 1.

Table 1: The optimum value of the parameter for the double substrates ME dipole (unit: mm)

Parameter	*w1*	*l2*	*w2*	*l3*	*l4*	*l5*
Value	0.7	2.1	0.8	3	1.3	2.4
Parameter	*l8*	*gap*	*gap2*	*gap3*	*W*	*l6*
Value	2	1	0.12	0.2	7.5	1
Parameter	*L*	*l1*	*l7*	*w5*	*w6*	
Value	9.5	2.1	6.2	0.4	0.34	

In Fig. 2, the parametric study of the ME element has been conducted, we can conclude that the parameters *L3* and *gap* affect the reflection coefficient obviously. And *L3* affects the resonating frequency more than *gap*. The current distribution on the patch also has been given in Fig. 4, it can be seen that the current densities on the dipole attain their maximum strength when t=0. After a quarter of a period, the current densities on the loop attain their maximum, which means that

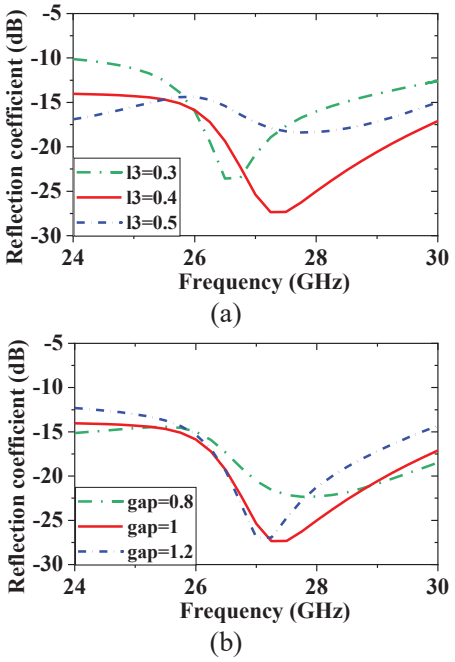

Fig. 3. Simulated reflection coefficient of different (a) l3, (b) gap.

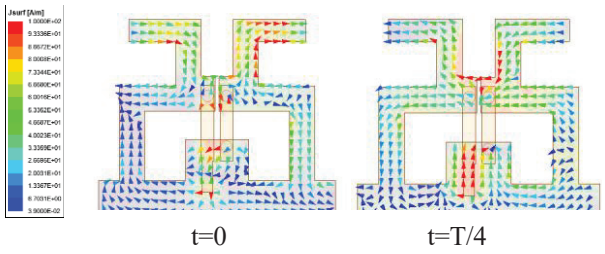

Fig. 4. The current distribution of the antenna element.

the electric dipole and the magnetic dipole are strongly excited.

B. 1×4 array design

Based on the proposed ME dipole, a 1×4 linear array is designed. As shown in Fig. 5, the element distance is set as 7.5mm in E-plane, which is $0.64\lambda_0$ of the center frequency 27 GHz. With this element distance, the mutual coupling between the elements is weak and has little effect on the array performance. In such a compact layout, it is impossible to place the power division network on the ground and feed the antenna through the floor with a probe as the conventional feeding network. Therefore, the power division network and 1×4 linear array are designed on the same dielectric substrate as seen in Fig. 5. The four elements are excited by a 1-to-4 stripline power divider, which has higher efficiency than a microstrip power divider with a single-layer dielectric substrate in the mmW band. In Fig. 6 (a), the impedance bandwidth for |S11|<-20 dB is 24-30 GHz. The highest realized gain is 11 dBi, and the radiation patterns at 27 GHz are given in Fig. 6 (b). We can see that the array exhibits a stable radiation pattern and wide H-plane beamwidth over the operating band.

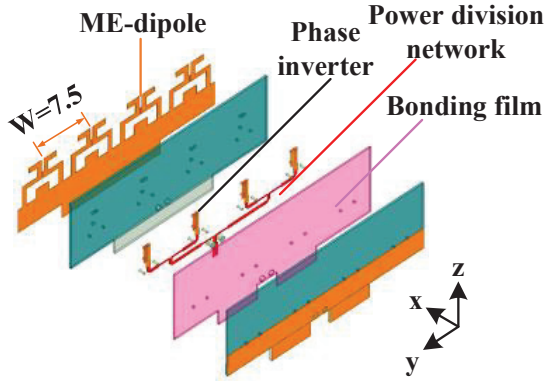

Fig. 5. The geometry of the 1×4 linear array.

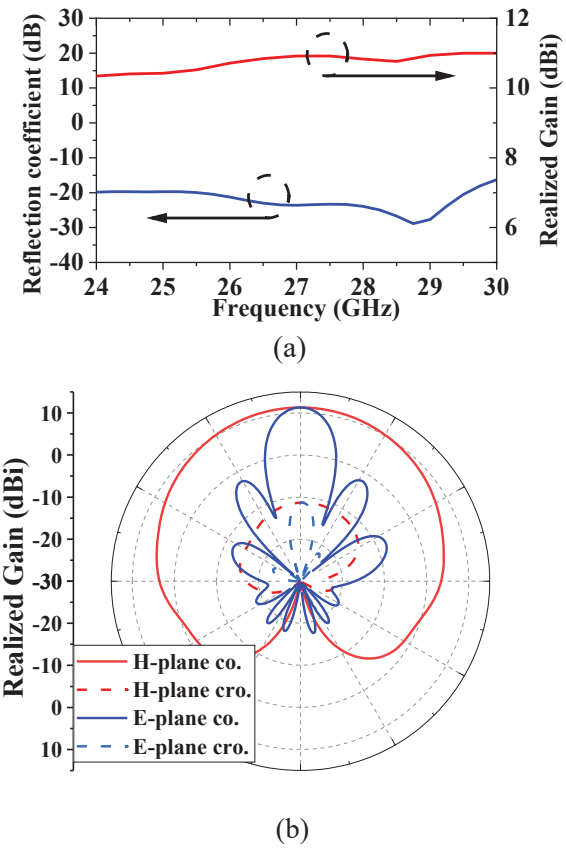

Fig. 6. The simulation results of the 1×4 linear array. (a) reflection coefficient and realized gain, (b) radiation patterns at 27 GHz.

C. 4×4 array with beam-tilt in E-plane

Based on the above 1×4 subarray, four 1×4 subarrays are employed to obtain a 4×4 array. Considering the requirements of isolation and radiation pattern scanning performance, the 4×4 array needs a compact physical structure, so the subarray spacing is 4.8 mm ($0.44\lambda_0$ at 27GHz in the free space) as can be seen in Fig. 7.

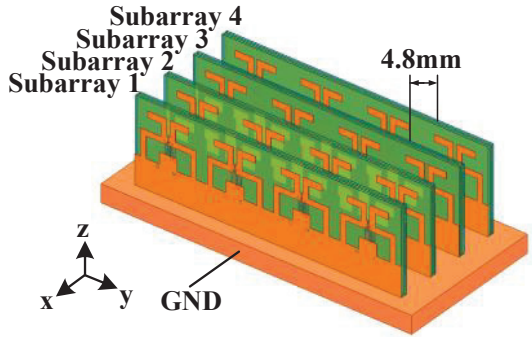

Fig. 7. The structure of the 4×4 array.

As depicted in Fig. 8, the return loss for the four outputs is larger than 12.5 dB over the whole frequency band. However, the isolation between the linear arrays is not so good, especially at lower frequencies. The worst value is about 11 dB, which would deteriorate the scanning performance for the 4×4 array.

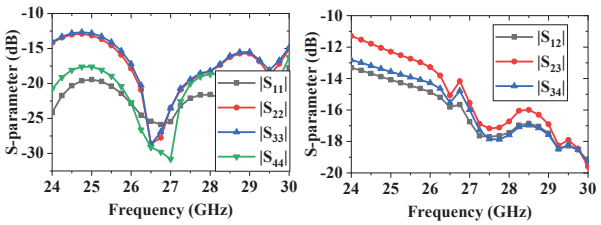

(a) (b)

Fig. 8. The S-parameters of the 4×4 array. (a) Return loss of four outputs. (b) Isolation between the four outputs.

In general, in the wireless communication system, beam tilt is used to expand the covered area and improve the antenna element isolation at the orthogonal plane. Here, this method is adopted to achieve better isolation between the subarrays. The decoupling principle of the beam-tilt design is shown as in Fig. 9, suppose an array composed of 8 elements denoted as A1-A8 can, it can be divided into 2 channels. A1-A4 are the four antennas in channel 1, A5-A8 are the four antennas in channel 2. If the feeding currents on antennas in channel 1 can be denoted as $i_1=e^0$, $i_2=e^{-if}$, $i_3=e^{-i2\varphi}$ and $i_4=e^{-i3\varphi}$, where the amplitude of the current is 1, the phase delay is $-\varphi$ to obtain the scanning characteristic. The phase delay -φ' is caused by the free space coupling path, if other factors can be ignored, then the current at antenna 5 through the coupling from antenna 1 is $e^{-if'}$ the so the received signal at the input port in channel 2 can be obtained as:

$$i_{receive}=e^{-i\varphi'}(1+e^{-i2\varphi}+e^{-i4\varphi}+e^{-i6\varphi}). \quad (1)$$

According to the Euler formula, it can be written as:

$$i_{receive}=e^{-i\varphi'}\begin{matrix}1+\cos2\varphi+\cos4\varphi+\cos6\varphi\\ -i(\sin 2\varphi+\sin4\varphi+\sin6\varphi)\end{matrix}. \quad (2)$$

Then the modulus value is:

$$|i_{receive}|=\sqrt{4+6\cos2\varphi+4\cos4\varphi+2\cos6\varphi}. \quad (3)$$

Set phase difference $\varphi=n\pi$, as long as n is not an integer, the modulus of the received signal in channel 2 is less than 4. If $\varphi=0$, then $i'_{receive}=4e^{-i\varphi'}$, $\left|i'_{receive}\right|=4$. When the beam deflects and φ is not equal to the integral multiple of π, that is $|i_{receive}|<\left|i'_{receive}\right|$, it can reduce the coupling between channels.

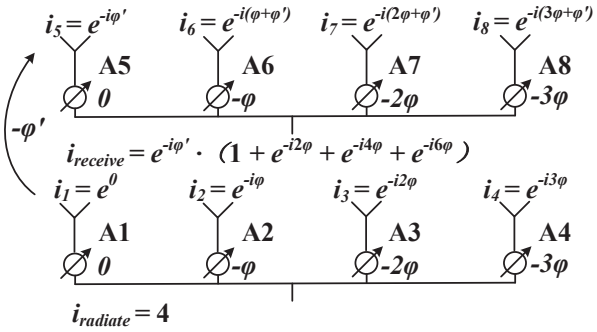

Fig. 9. The decoupling principle of beam-tilt design.

According to the calculation and analysis, the optimum beam down-tile angle should be 8°, which can meet the requirements of the channel isolation in H-plane and the directional gain in E-plane. Therefore, the phase difference between the output ports of the power divider should be 35°.

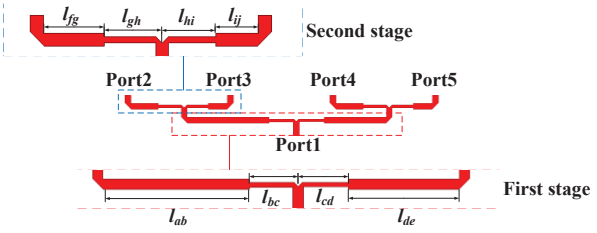

Fig. 10. The diagram of the unequal phase power divider.

The diagram of the unequal phase power divider is shown in Fig. 10. It consists of two stages of power divider. In the first stage, the electrical length of l_{ab} is more than l_{de} by 70° (the physical length is 1.53 mm at 27 GHz) and the electrical length of l_{bc} and l_{cd} is set as a quarter of the wavelength at 27 GHz, the characteristic impedance is 70.7 ohm to determine the width of the strip line. In the second stage, the length of l_{fg} is 0.76 mm longer than l_{ij}, corresponding to a phase difference of 35°. After fine-tuning, the dimensions of the unequal phase power divider are obtained as shown in Table 2.

Table 2: The optimum value for the unequal phase power divider (unit: mm)

Parameter	l_{ab}	l_{bc}	l_{cd}	l_{de}
Value	6.06	2	2	4.52
Parameter	l_{fg}	l_{gh}	l_{hi}	l_{ij}
Value	2	1.9	1.78	1.39

In Fig. 11 (a), the return loss is larger than 20 dB over the whole band. And the transmission coefficients are better than -6.56 dB, which mean the biggest insertion loss is 0.56 dB. The amplitude unbalance is ±0.3dB or so, while the phase unbalance is just ±5°.

With the above unequal phase feeding network, the isolation can be improved obviously. As given in Fig. 2, the coupling between the subarrays has been decreased by 5dB in average. Especially at high frequencies, the isolation even reaches 35dB, compared with Fig. 8 (b).

Additionally, the simulated radiation efficiency has been given in Fig. 13, across the entire band, it is more than 76%.

D. 4×4 array with resonant split rings

For the need of scanning, the 4 × 4 array is placed on a copper ground with a size of 40mm×30mm×2mm.

As shown in Fig. 14, fix the four 1×4 subarrays and connector, the copper ground is slotted. The 1×4 arrays

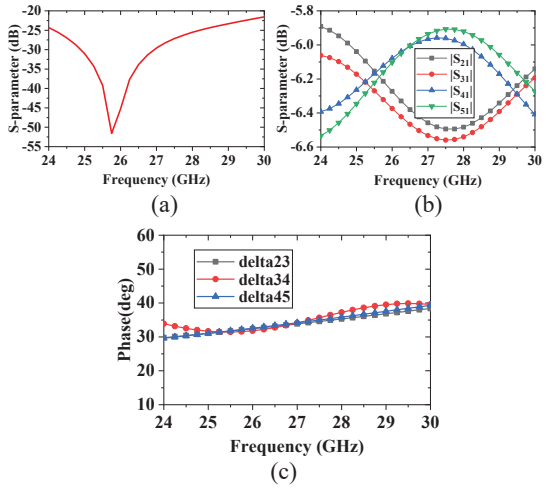

Fig. 11. The simulated results of the unequal phase power divider. (a) Return loss, (b) transmission coefficients, and (c) transmission phase difference.

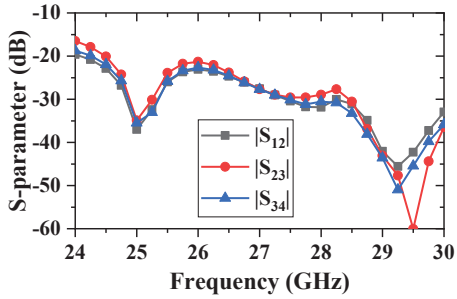

Fig. 12. The isolation between the subarrays with beam-tilt.

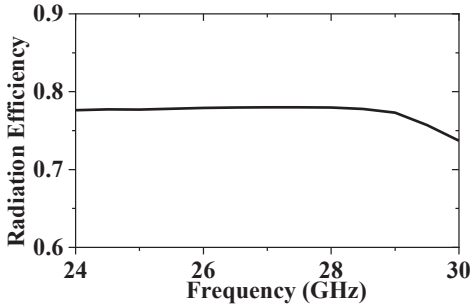

Fig. 13. The simulated radiation efficiency of the array.

are divided into two groups and placed symmetrically for better cross-polarization [21].

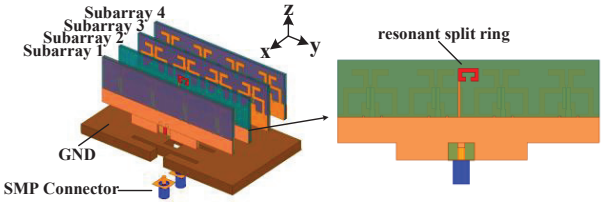

Fig. 14. The final diagram of the 4 × 4 array for fabrication.

The isolation between 2 and 3 channels at approximately 25 GHz is less than 20 dB. To achieve high isolation at lower frequencies, resonant split rings are added to the 4×4 array. Firstly, resonant split rings resonating at 25 GHz are added on the back side of subarray2 and subarray3 to absorb electromagnetic energy. Then the resonant split rings are grounded to transmit energy to the ground through a long thin line. After loading the open resonant ring, the isolation between the subarrays has been improved more than 20dB as given in Fig. 15.

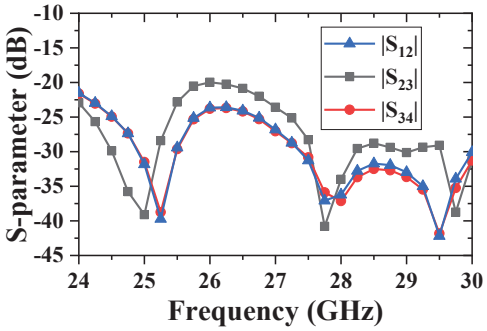

Fig. 15. The isolation between the subarrays with resonant split rings.

E. The wide-angle scanning performance

To verify the beam scanning performance, active simulation cooperated with full-wave solver ANSYS HFSS is implemented. The four 1×4 subarrays are fed by excitations with same amplitudes and different phases. Figures 16 (a)-(b) depicts the simulated active reflection coefficients at the broadside direction and the scan angle of 55°. It can be seen that the active reflection coefficients for four subarrays is less than -10 dB even at the scan angle of 55°, owing to the excellent isolation between the subarrays. The main beam can scan to 55° with scan losses lower than 3.0 dB/2.5 dB and sidelobes lower than -8.5 dB/-4.7 dB at 24.25 GHz/29.5 GHz as shown in Figs. 16 (c)-(d).

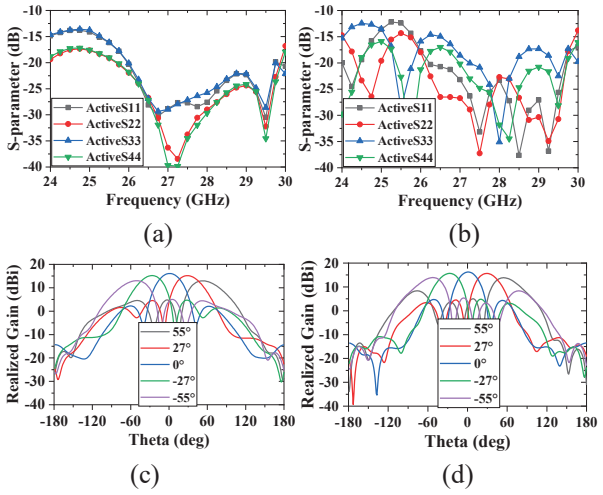

Fig. 16. The Active S-parameters when the beam scan to (a) 0°, (b) 55°, and the wide-angle scanning performance at (c) 24.25 GHz, and (d) 29.5 GHz.

III. MEASURED RESULTS AND DISSCUSION

For verification, a prototype of the 4×4 array loaded with open resonant ring, as shown in Fig. 17, was fabricated and measured. The S-parameters of the array were measured by Agilent E8363B vector network analyzer, and the results are shown in Fig. 18. It can be seen that the return loss is almost higher than 10 dB from 25 GHz to 30 GHz, some points are less than 10 dB owing to the fabrication error, and the isolation between the channels is lower than -20 dB from 24 GHz to 30 GHz.

The radiation pattern of the array is measured by an in-house far-field mmW antenna measurement system, and the gains were measured by comparing with the standard gain horn antenna. Figure 19 gives the measured radiation pattern in H-plane with the one-to-four equal powder divider, we can see the radiation patterns at different frequencies meet with the simulated ones.

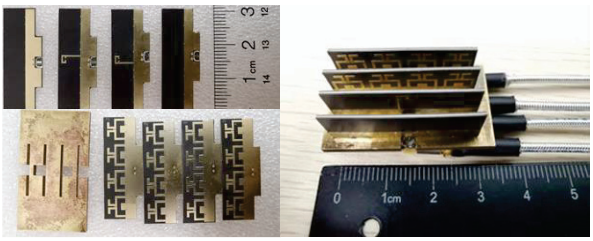

Fig. 17. The photo of the fabricated 4×4 array. (a) the disassembled antenna. (b) the assembled antenna.

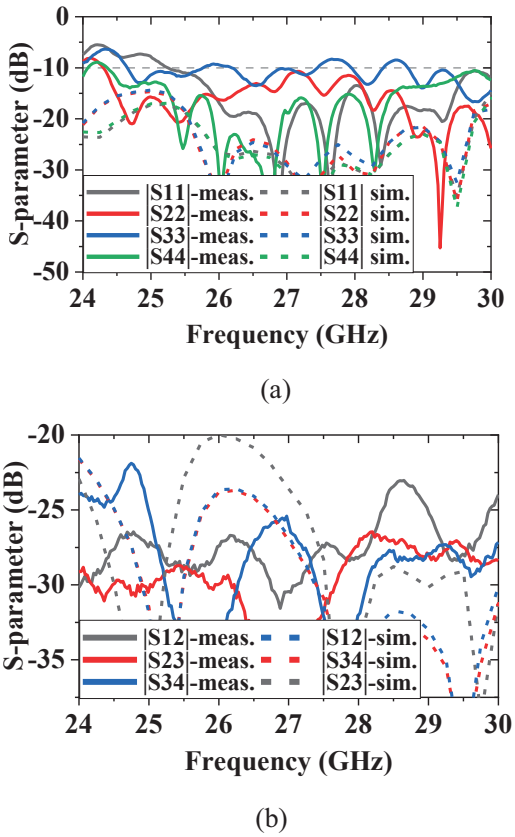

Fig. 18. The simulated and measured S-parameters of the 4×4 array. (a) Return loss. (b) Isolation.

From the E-plane radiation patterns, the beam points to the maximum at about 8°. Unfortunately, there is no suitable beamforming network to verify the scanning performance of the final fabricated array, but it is believed that the scanning performance will be fine as expected, like the above E-plane and H-plane radiation patterns. The simulated and measured gain are compared in Fig. 20, the measured gain is up to 15.0 dBi with a variation of 1.0 dB over the operating band of the array. The deviation between measured and simulated gain results

Table 3: Comparisons with other antenna arrays

Ref	f_0 (GHz)	Bandwidth (%)	Dimension	Isolation (dB)	Scan Range (°)	Size	Gain Loss (dB)
[1]	27	47	1×4	N.A.	±35	1.1 λ_0 × 2 λ_0	3
[14]	27	17.7	1×8	< -15	±62	0.5 λ_0 × 4 λ_0	3
[16]	6.2	11.5	1×4	< -15	±70	0.46 λ_0 × 1.2 λ_0	3
[17]	3.5	28.6	1×8	< -13	±60	0.28 λ_0 × 2.33 λ_0	2.5
This work	27	19.5	4×4	< -20	±55	1.29 λ_0 × 2.5 λ_0	3

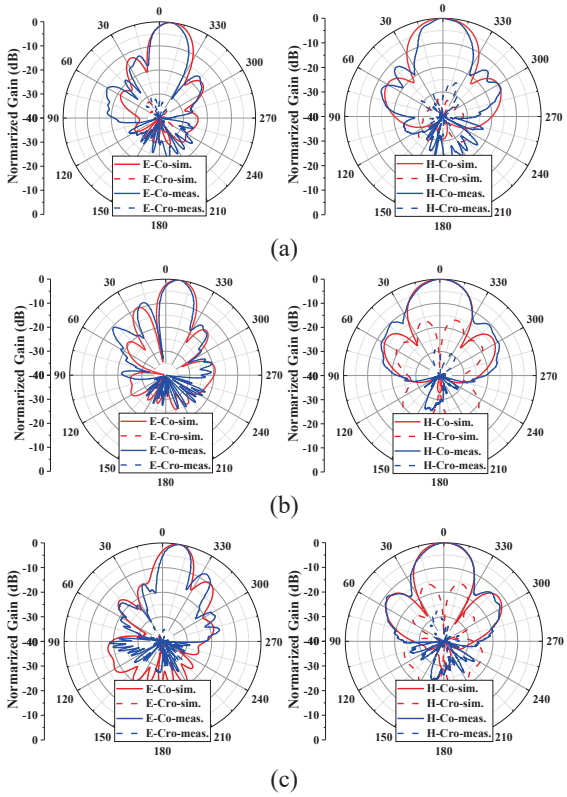

Fig. 19. The measured radiation patterns for the proposed antenna array (Left: E plane Right: H plane) at: (a) 24.25 GHz, (b) 27 GHz, and (c) 29.5 GHz.

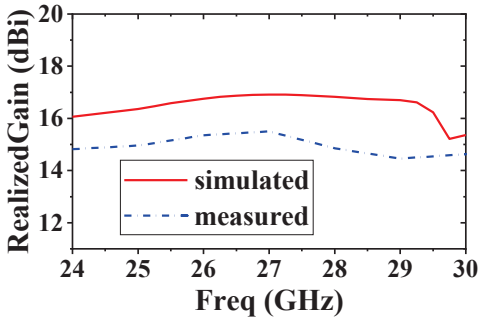

Fig. 20. Measured and simulated peak gain of the proposed antenna array.

is mainly caused by fabrication error and the uncertain influence of the measurement setup close to the antenna under test. The degradation of the impedance matching at the lower band of the frequency range would also affect the measured gain.

In Table 3, the comparison between our work and other antenna arrays is presented. The suggested antenna array has a broader operating bandwidth and higher isolation than the designs in [14] and [16] because of the wide band characteristic of the proposed antenna element and the isolation improvement measures for the array. The bandwidth of antenna in [1] is much wider than the proposed antenna, while our work has better performance in beam scanning. The array in [17] has wide-angle scanning and wideband characteristic; however, the isolation between the subarrays is not as good as our work.

IV. CONCLUSION

A mmW wideband high-isolation wide-angle scanning phased array based on end-fire magnetoelectric (ME) dipole is presented. A 1×4 double dielectric substrate planar ME dipole linear array with a strip line feed network is designed to get higher antenna efficiency. Then, four 1×4 subarrays is used to form a 4×4 array to realize the wide-angle scanning performance. Furthermore, to achieve better isolation, both beam down-tilt and resonant split rings are employed. Owing to the wide beamwidth of ME dipole and high isolation between the subarrays, the 4×4 array can obtain the wide-angle scan characteristic. The final antenna covers an operating bandwidth of 19.5% (24.25-29.5 GHz) with return loss more than 10dB, which can meet the band in the 5G standard. The mutual coupling between the subarrays can be effectively reduced less than -20dB over the

entire bandwidth. The beam can scan of approximately $\pm 55^{\circ}$ with a realized gain reduction under 3 dB in the wide operating bandwidth. Additionally, the simulated radiation efficiency of the array is more than 77% over almost the whole band. The antenna will be a potential candidate to be applied in 5G applications.

REFERENCES

[1] B. Yang, Z. Yu, Y. Dong, J. Zhou, and W. Hong, "Compact tapered slot antenna array for 5G millimeter-wave massive MIMO systems," *IEEE Trans. Antennas Propag.*, vol. 65, no. 12, pp. 6721-6727, 2017.

[2] T. Li and Z. N. Chen, "Wideband sidelobe-level reduced Ka-band metasurface antenna array fed by substrate-integrated gap waveguide using characteristic mode analysis," *IEEE Trans. Antennas Propag.*, vol. 68, no. 3, pp. 1356-1365, 2020.

[3] S. P. Dubazane, P. Kumar, and T. J. O. Afullo, "Metasurface superstrate-based MIMO patch antennas with reduced mutual coupling for 5G communications," *Applied Computational Electromagnetics Society (ACES) Journal*, vol. 37, no. 4, pp. 408-419, 2022.

[4] H. Zhu, Y. Qiu, J. Bai, and G. Wei, "Compact design of non-uniform meta-surface for patch antenna main beam steering," *Applied Computational Electromagnetics Society (ACES) Journal*, vol. 34, no. 9, pp. 1300-1304, 2019.

[5] D. Wang, H. Wong, K. B. Ng, and C. H. Chan, "Wideband shorted higher-order mode millimeter-wave patch antenna," *Proceedings of the 2012 IEEE International Symposium on Antennas and Propagation*, pp. 1-2, 2012.

[6] L. Lu, K. Ma, F. Meng, and K. S. Yeo, "Design of a 60-GHz Quasi-Yagi antenna with novel ladder-like directors for gain and bandwidth enhancements," *IEEE Antennas Wireless Propag. Lett.*, vol. 15, pp. 682-685, 2016.

[7] Y. Li, L. Ge, J. Wang, S. Da, D. Cao, J. Wang, and Y. Liu, "3-D printed high-gain wideband waveguide fed horn antenna arrays for millimeter-wave applications," *IEEE Trans. Antennas Propag.*, vol. 67, no. 5, pp. 2868-2877, May 2019.

[8] P.-Y. Feng, S.-W. Qu, X.-H. Chen, and S. Yang, "Low-profile high-gain and wide-angle beam scanning phased transmitarray antennas," *IEEE Access*, vol. 8, pp. 34276-34285, 2020.

[9] Z.-Y. Yu, Y.-H. Zhang, S.-Y. He, H.-T. Gao, H.-T. Chen, and G.-Q. Zhu, "A wide-angle coverage and low scan loss beam steering circularly polarized folded feflectarray antenna for millimeter-wave applications," *IEEE Trans. Antennas Propag.*, vol. 70, no. 4, pp. 2656-2667, 2022.

[10] Y. Ding, S. Hou, and G. Yang, "Wide-angle scanning dielectric resonator antennas for millimeter-wave applications," *International Symposium on Antennas and Propagation (ISAP)*, pp. 1-2, 2021.

[11] Z. Qu, S. -W. Qu, Z. Zhang, S. Yang, and C. H Chan, "Wide-angle scanning lens fed by small-scale antenna array for 5G in millimeter-wave band," *IEEE Trans. Antennas Propag.*, vol. 68, no. 5, pp. 3635-3643, 2020.

[12] Y. Ye, Z. Y. Huang, Y. Jiang, L.-A. Bian, C. Zhu, J. J. Huang, and N. C. Yuan, "A wideband and wide scanning tightly coupled dipole array with metasurface wide-angle impedance matching," *Applied Computational Electromagnetics Society (ACES) Journal*, vol. 36, no. 7, pp. 872-878, 2021.

[13] Z. Zhao, Y. Zhu, and C. Deng, "Microstrip phased array antenna with small element space for 5G millimeter-wave applications," *IEEE 3rd International Conference on Electronic Information and Communication Technology (ICEICT),* pp. 620-622, 2020.

[14] S. Pan, W. Yang, W. Che, and Q. Xue, "Millimeter-wave wide-angle scanning phased array based on low-profile wide-beam patch antenna element," *IEEE MTT-S International Wireless Symposium (IWS)*, pp. 1-3, 2020.

[15] Z.-F. Yuan and Z.-H. Tu, "Wideband $\pm 45^{\circ}$ dual-polarized millimeter-wave antenna array with wide-angle scanning performance," *International Conference on Microwave and Millimeter Wave Technology (ICMMT)*, pp.1-3, 2021.

[16] M. K. Ishfaq, T. Abd Rahman, M. Himdi, H. T. Chattha, Y. Saleem, B. A. Khawaja, and F. Masud, "Compact four-element phased antenna array for 5G applications," *IEEE Access*, vol. 7, pp. 161103-161111, 2019.

[17] Y. Feng, J.-Y. Li, L.-K. Zhang, X.-J. Yu, Y.-X. Qi, D. Li, and S.-G. Zhou, "A broadband wide-angle scanning linear array antenna with suppressed mutual coupling for 5G sub-6G applications," *IEEE Antennas Wireless Propag. Lett.*, vol. 21, no. 2, pp. 366-370, 2022.

[18] X. Dai, A. Li, and K. M. Luk, "A wideband compact magnetoelectric dipole antenna fed by SICL for millimeter wave applications," *IEEE Trans. Antennas Propag.*, vol. 69, no. 9, pp. 5278-5285, Sep. 2021.

[19] Z. Tang and Y. Dong, "A Ka-band antenna array based on wide-beamwidth magnetoelectric dipole," *IEEE Antennas Wireless Propag. Lett.*, vol. 21, no. 3, pp. 501-505, 2022.

[20] J. Zeng and K. Luk, "Wideband millimeter-wave end-fire magnetoelectric dipole antenna with microstrip-line feed," *IEEE Trans. Anten-*

nas Propag., vol. 68, no. 4, pp. 2658-2665, Apr. 2020.

[21] Z. Zhou, S. Yang, and Z. Nie, "A novel broadband printed dipole antenna with low cross-polarization," *IEEE Trans. Antennas Propag.*, vol. 55, no. 11, pp. 3091-3093, Nov. 2007.

Fang-Fang Fan received a Ph.D. degree in Electromagnetic Field and Microwave Technology from Xidian University in 2011. Currently, she is an associate professor at Xidian University. Her current research interests include antenna arrays, gap waveguide technology and base station antennas for 5G application.

Qing-Lin Chen received bachelor's degree in Electronic Information Engineering from Xidian University, China, in 2020. Since 2020, he has been studying for a master's degree in Electronic and Communication Engineering at Xidian University, China. His research interests include Millimeter wave antenna array for 5G application.

Kai Qin received a master's degree from Xidian University in Xi'an, China, in June 2021. Since September 2021, he has been studying for a Ph.D. degree at City University of Hong Kong, Hong Kong, China. His research interests include antennas used in millimeter-wave and sub-Terahertz bands.

Broadband Circularly-polarized Crossed-dipole Antenna with Good Gain Stability

Xueyan Song, Zhiyuan Wu, Xuping Li, Yunqi Zhang, and Hailong Yang

School of Electronic Engineering
Xi'an University of Posts & Telecommunications, Xi'an, 710121, China
xysong6597@126.com, 1406936884@qq.com, lixuping@163.com, johnny_5@126.com, yanghl68@163.com

Abstract – A broadband Circularly Polarized (CP) cross-dipole antenna with the merit of stable gain is proposed. The designed antenna consists of crossed dipoles, parasitic patches, reflectors, and vertical parasitic plates. By adding parasitic patches and parasitic plates, the circular polarization performance of the antenna is significantly improved. Furthermore, the gain value becomes stable in the entire operating frequency band by modifying the structure of the parasitic plates. The final dimension of the presented antenna is $0.76\lambda_0 \times 0.76\lambda_0 \times 0.28\lambda_0$ (λ_0 is the wavelength at the center frequency point in the circularly polarized working frequency band). The measured results depict that the Impedance Bandwidth (IBW) is 80.8% (2.03GHz∼4.78GHz) and the Axial Ratio Bandwidth(ARBW) is 68.5% (2.35GHz∼4.8GHz). Stable gain values, ranging from 6dBic to 7.5dBic, are obtained in the working frequency band, and the average gain can reach 7dBic.

Index Terms – broadband, circularly polarized, cross-dipole, parasitic patches, stable gain.

I. INTRODUCTION

Because of better reception performance, circularly polarized antennas have been found in many applications in Global Navigation Satellite Positioning Systems (GNSS), satellite communication systems, radio frequency identification, etc.

Microstrip patch antennas have become one of the most popular antennas due to their good characteristics, such as low profile, small size, and easy processing. Common techniques to generate CP performance are to produce a perturbation by cutting corners on the diagonal of a square patch or etching a cross slit in the ground plane. The above methods have been studied theoretically by Sharma [1] as early as 1983. The single-fed circularly polarized antenna with the perturbation method has the advantage of a simple structure. However, the bandwidth is generally narrow. In order to obtain wide circular polarization bandwidth, antennas with complementary structures, in which typically one is the crossed dipole antenna, are adopted to generate CP performance nowadays.

Due to their superior CP performance, crossed dipole antenna is one of the most popular antennas to achieve broadband and CP characteristics. In recent years, various structures of crossed-dipole antennas have been proposed to broaden the CP bandwidth. In [2], Baik proposed a crossed dipole circularly polarized antenna using a single port feed, which achieved a final ARBW of 15.6%. In [3], Baik added square opening rings to increase the ARBW of the antenna to 28.6%. By loading the butterfly-crossed dipole antenna with four parasitic triangular patches, the ARBW of the antenna in [4] can reach 42.3%. By adding circularly polarized patches, the antenna in [5] can obtain an ARBW of 66%. In [6], four grounded metal posts are inserted in the proposed antenna to achieve an ARBW of 78%. In addition, the cavity structure can also be utilized to broaden bandwidth. In [7], a surrounding non-closed cavity is formed by adding four parasitic plates, which brings about an ARBW of 63.4%. By loading a closed cavity all around, the antenna in [8] can obtain an ARBW of 58.6%. In [9], by adding folded cavity to the vertical, the ARBW of the antenna to 52.4%. In [10], in addition to the introduction of the cavity, an annular reflection ring is added between the cavity and the antenna to achieve an ARBW of 85.5%.

Although circularly polarized crossed dipole antennas own broadband property, the fluctuation of their gain values is large. The wider the bandwidth, the worse the gain flatness, as shown in Table 1. The gain flatness of the antenna is the fluctuation of gain curves in a certain band, which is an important indicator to measure the dynamic characteristics of the antenna. And the flatter the gain curve, the better the receiving characteristic of antennas. Therefore, an important parameter $\Delta G = Gain_{max} - Gain_{min}$ [12] is defined to describe the variation of gain values. To achieve stable gain, an ultra-wideband CP crossed-dipole antenna was designed in [13].

To obtain wider bandwidth and better gain flatness simultaneously, a broadband stable-gain

Submitted On: July 28, 2022
Accepted On: November 29, 2022
https://doi.org/10.13052/2022.ACES.J.371109

Table 1: Comparison of the proposed CP antenna and references

References	Overall Size (λ_0)	IBW	ARBW	Variety range of Gain (dBic)	ΔG (dB)
[5]	1.04* 1.04* 0.26	77.6% (1.11GHz -2.52 GHz)	66% (1.25GHz-2.48GHz)	7-2	5
[6]	1.17* 1.17* 0.29	95.0% (1.16GHz-3.26GHz)	85.5% (1.24GHz-3.09GHz)	1.12-6.67	5.55
[7]	0.46* 0.46* 0.1	78.3% (0.91GHz-2.08GHz)	63.4% (0.97GHz-1.87GHz)	4.5-2.5	2
[8]	0.79* 0.79* 0.27	68.9% (1.9GHz-3.9GHz)	58.6% (2.05GHz-3.75GHz)	7.4-9.4	2
[9]	0.79* 0.79* 0.27	63.2% (1.04GHz-2GHz)	52.4% (1.1GHz-1.88GHz)	2-4	2
[10]	1.1* 1.1* 0.37	98.2% (1.73GHz-5.07GHz)	85.5% (1.94GHz-4.84GHz)	6.4-10	3.6
[11]	0.6* 0.6* 0.25	44% (1.95GHz-3.05GHz)	31% (2.2GHz-3GHz)	5.8-6.5	0.7
Proposed	**0.76* 0.76* 0.28**	**80.8% (2.03GHz-4.78GHz)**	**68.5% (2.35GHz-4.8GHz)**	**6-7.5**	**1.5**

circularly polarized cross-dipole antenna is proposed in this paper. Compared with reference [13], a modified cavity is utilized in this design. The measured results show that the IBW of the proposed antenna is 80.8%(2.03GHz∼4.78GHz) and the ARBW is 68.5% (2.35GHz∼4.8GHz). And the gain flatness can keep well in the range from 6dBic to 7.5dBic.

II. ANTENNA DESIGN AND ANALYSIS

A. Antenna configuration

The physical structure of the proposed antenna is illustrated in Fig. 1. As seen from the figure, the proposed antenna is composed of three layers. In the top layer, dipole arms are printed on both sides of the F4B (ε_r=2.65, tanδ=0.001) dielectric substrate with a thickness of h, 0.8mm. Furthermore, by adding parasitic rectangular patches on both sides of the dipole arms, broad bandwidth performance can be obtained. The rectangular dipole arms are connected by a phase delay loop to achieve a 90° phase difference. The delay rings on both sides of the dielectric substrate are connected by the outer and inner conductors of a 50-ohm coaxial

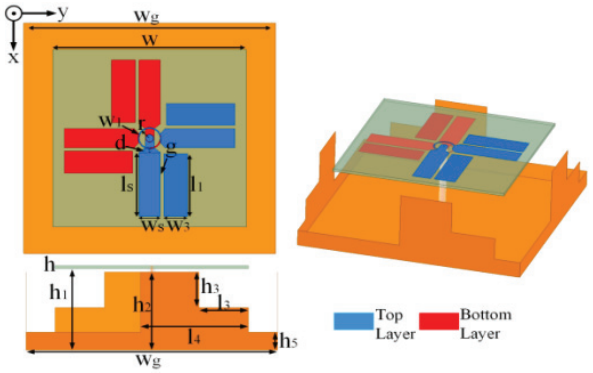

Fig. 1. The configuration of the proposed antenna.

cable. The bottom layer is mainly a metal reflector, which can further increase the gain of the antenna. Between the bottom and top layers, stepped-shaped metal walls on the vertical space are used to further broaden the bandwidth. Finally, the metal wall is modified to make the gain values stable in the entire operating band. The detailed parameter dimensions of the antenna are as follows: wg=65mm, w=50mm, r=3.2mm, w1=0.3mm, w2=2.2mm, d=1mm, ls=18mm, ws=5.4mm, g=1mm, w3=6mm, l1=17.5mm, h=0.8mm, h1=23mm, h2=22mm, h3=10mm, l3=12.8mm, l4=27.8mm, h5=5mm.

B. Design process

The proposed antenna is a crossed dipole antenna that can achieve circular polarization. The principle of the circularly polarized crossed dipole is demonstrated as follows. According to transmission line theory: $\theta = 2\pi L/\lambda$, the length of λ/4 phase delay loop is introduced in a dipole antenna. To broaden the bandwidth, parasites are added in the proposed antenna, which can produce new equivalent capacitance or inductance, thus generating different resonance points according to the resonant formula: $f = 1/(2\pi\sqrt{LC})$.

To illustrate the design process of the proposed antenna clearly, the design procedures of the proposed antenna are shown in Fig. 2. A simple crossed dipole circularly polarized antenna is designed as Ant. 1, which is evolved from the most basic crossed dipole antenna, and the bandwidth is increased by widening the dipole arm.

By adding a parasitic rectangular patch on Ant. 1, Ant. 2 is obtained, and the bandwidth is further widened caused by the generation of new resonance. Ant. 3 was generated by loading four metal walls on the vertical space between the metal plate and Ant. 2, which can bring better bandwidth performance. The vertical parasitic plate is coupled with the dipole arm, which introduces an equivalence capacitor in the low-frequency band. According to the resonance formula, the operation

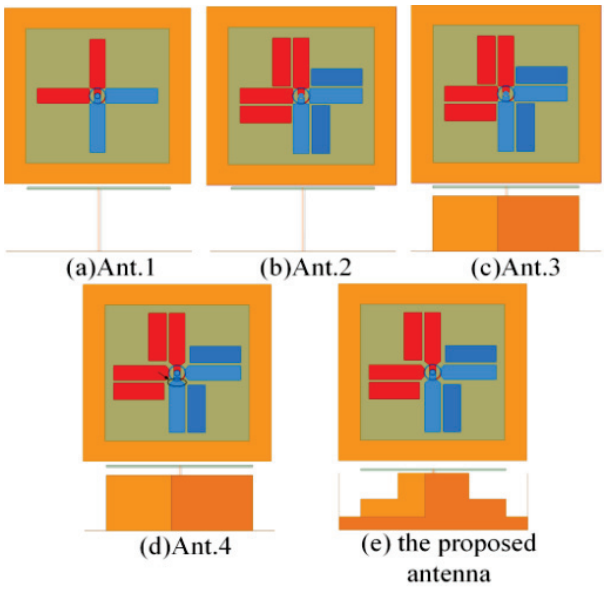

Fig. 2. Antenna evolution (a) Ant. 1, (b) Ant. 2, (c) Ant. 3, (d) Ant. 4, and (e) the proposed antenna.

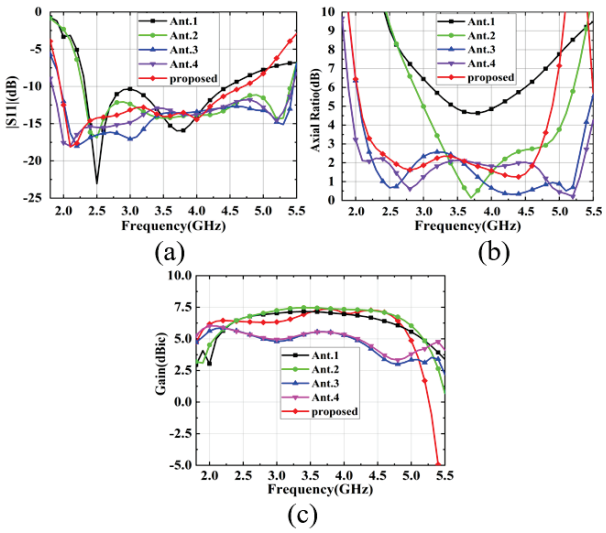

Fig. 3. Simulated results of the five antennas: (a) |S11|, (b) AR, (c) gain.

band will be expanded in low-frequency band. To further increase the bandwidth, a triangular tapering process is used between dipole arms and the phase delay loop in Ant. 3, which is present in Ant. 4. By digging rectangular notches out on the cavity structure of Ant. 4, the Ant. 5 (the proposed antenna) is obtained, the gain variation of which is slight.

C. Working mechanism

This section will illustrate the principles of wide bandwidth and gain flatness, and demonstrate the current distribution of the proposed antenna.

The simulated |S11|, AR and gain results of the above antennas are shown in Fig. 3. It can be seen from Fig. 3 that, compared with Ant. 1, Ant. 2 (loading by parasitic patches on Ant. 1) has a wider IBW of 38.6% (3.26GHz∼4.82GHz), and a wider ARBW of 81% (2.29GHz∼5.41GHz) which is because the application of the parasitic patch generates multiple resonant points. As shown in Figs. 3 (a) and (b), Ant. 2 generates a resonance point at the high frequency, and the bandwidth of |S11| and AR are widened. Then, it can also be demonstrated that the axial ratio bandwidth of Ant. 3 is broadened in both low and high-frequency band. And the ARBW can reach 81% (2.29GHz∼5.41GHz), which is because the coupling between vertical parasitic plates and dipole arms extends the current path and improves the AR in the middle and high frequencies. From Figs. 3 (a) and (b), it can be seen that the IBW of Ant. 4 is 99.3% (1.83GHz∼5.44GHz) and the ARBW of Ant. 4 is 91.4%(2.02GHz∼5.42GHz). The bandwidth is further broadened due to the improved matching by the tapering structure. Finally, in compromise of the bandwidth and gain flatness, the cavity of Ant. 5 (the proposed antenna) is designed as a stepped shape by digging out the rectangular block from the side cavity formed by the rectangular patches. Although the IBW and ARBW become narrow, the gain curves become more smooth compared with Ant. 3 and Ant. 4 as shown in Fig. 3(c). The proposed antenna exhibits an ARBW of up to 70.9% (2.26GHz∼4.71GHz) and an IBW of 82.7%. And the gain values range from 6dBic to 7.5dBic.

To clarify the cause of flatness of gain, it can be seen from the evolution from Ant. 2 to Ant. 3. Ant. 3 is constructed by adding vertical metal plates on Ant. 2, which broadens the bandwidth largely. The addition of a vertical metal plate to extend the current path by adding coupling, which moves the operation frequency band of the proposed antenna to a lower frequency band and thus broadens the bandwidth, as shown in simulation results of Ant. 2 and Ant. 3 in Fig. 3 (b) in the paper. Furthermore, the addition of a vertical metal plate mainly affects the bandwidth of antennas in the low-frequency band. While the introduction of a vertical metal plate generates coupling which makes the energy transfer to the metal plate, causing a decrease in the gain of the antenna in the high band, as can be seen from Fig. 3 (c). Additionally, the higher the frequency band, the more significant the decrease in gain. Therefore, the lower coupling is required in the high-frequency band by changing the structure of the vertical metal plate.

When the vertical metal plates are modified to stepped shapes, the coupling between the antenna and the vertical metal plate in the high-frequency band can be

decreased, which decreases the energy consumption in the high-frequency band. Therefore, the gain value in the high-frequency band becomes close to that in the low-frequency band, generating a more smooth curve of gain values.

The simulated vector surface current distribution of the proposed antenna at 2.5 GHz, 3.5 GHz, and 4.5 GHz (corresponding to the low to mid-high frequencies of the CP band) is shown in Fig. 4. It can be obtained that external parasitic components can cause resonance in the low-frequency band. As can be seen in Fig. 4 (a), the current directions at 0° and 90° are orthogonal. Therefore, the CP wave is generated. From Fig. 4 (c), the crossed-dipoles generate high-frequency resonances . As shown in Fig. 4 (b), although all antenna elements excite currents in different directions simultaneously, the overall current directions are determined in 0° and 90° directions in an orthogonal way, which brings in CP wave in the mid-frequency. Moreover, Fig. 4 also shows that the radiation at 2.5 GHz, 3.5 GHz, and 4.5 GHz is right-hand circularly polarized wave (RHCP) because the surface current flows in a counterclockwise direction at two phases.

D. Parametric analysis

Among all the parameters, the width of the vertical metal plate gap (l3) and the height of the vertical metal plate (h2) have an important effect on the performance of the presented antenna. And Fig. 5 depicts the Simulated Axial Ratio and Gain Effect of the proposed antenna with different values of l_3 and h_2. The parameter l_3 mainly affects the gain values in the high-frequency band. When l_3 increases, the coupling between the dipole arm and the metal plate reduces, which thus increases the gain values in the high-frequency band, as can be seen in Fig. 5 (a). The parameter h_2 mainly affects the AR values in the low-frequency band. When h_2 increases, the current path is extended, which generates a new resonance point and broadens the AR bandwidth in the low-frequency band, as can be seen in Fig. 5 (b).

III. SIMULATED AND MEASURED RESULTS

As shown in Fig. 6, the physical object of the proposed antenna is fabricated and measured, and Fig. 6 (c) depicts the test environment.

Shown in Fig. 7 (a) is the simulated and measured |S11| and the simulated efficiency of the proposed antenna. It can be seen that, the simulated and measured IBW (S11<-10dB) is 82.7% (1.95GHz~4.7GHz) and 80.8% (2.03GHz~4.78GHz), respectively, between which there is a deviation of 3.2% due to machining errors and losses. In addition, the measured |S11| results show a relatively large fluctuation, which is because the processing precision is insufficient, the surrounding cavity is consist of hand-folded copper pieces, and the coaxial welding is uneven. It can also be seen from Fig. 7 (a) that the efficiency of the antenna is 94% on average (the gray area in the simulated figure expresses the frequency band that the proposed antenna operates in circular polarization). Also, the efficiency of the antenna

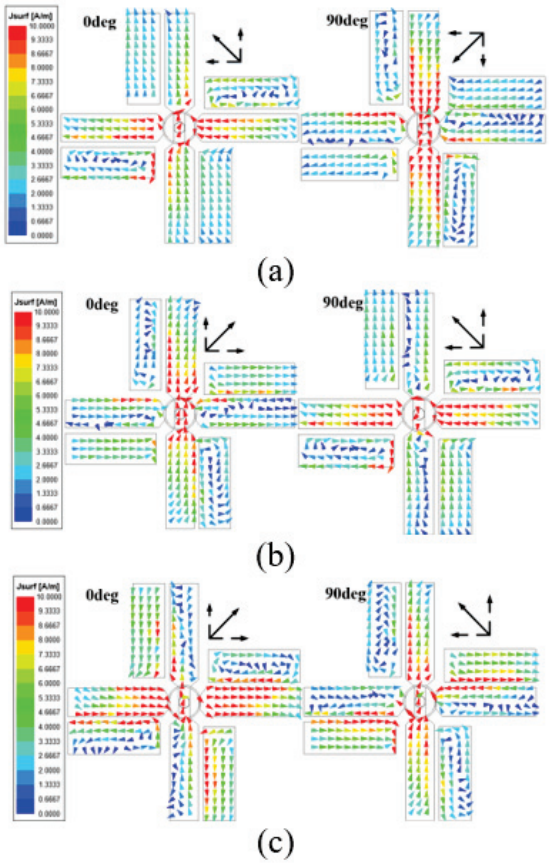

Fig. 4. The simulated surface current distribution of the proposed antenna: (a) 2.5 GHz, (b) 3.5 GHz, and (c) 4.5 GHz.

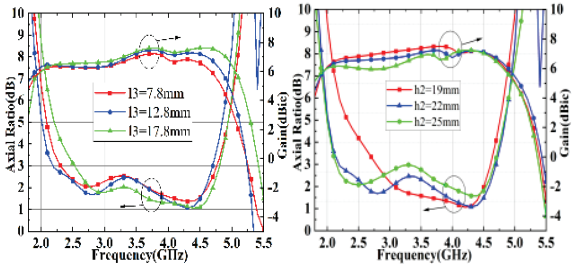

(a) (b)

Fig. 5. Simulated Axial Ratio and Gain Effect of the proposed antenna with different values of the main parameters including (a) l_3 and (b) h_2.

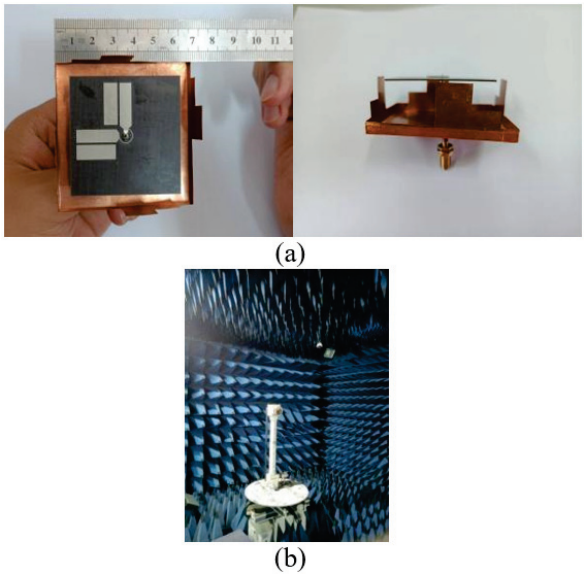

Fig. 6. (a) Photograph of the antenna. (b) The test environment.

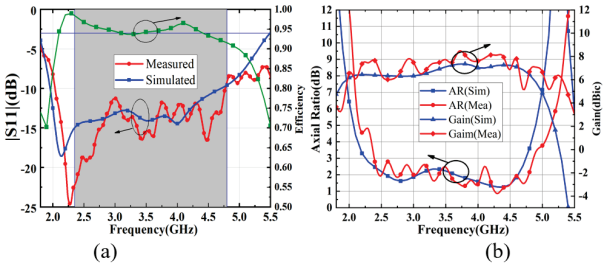

Fig. 7. Simulated and measured of (a) |S11| and efficiency (b) AR and gain.

is higher than 92% across the entire operating frequency band.

In Fig. 7 (b), the AR and gain results of the proposed antenna are depicted. The simulated and measured ARBW is 70.9% (2.26GHz∼4.71GHz) and 68.5% (2.35GHz∼4.8GHz), respectively. The simulated gain results range from 6 to 7.45dBic, and the measured gain results range from 6dBic to 8dBic, which can be seen that the average gain reaches 7dBic in the entire operating band and the gain values changes in a very small range.

The normalized radiation patterns of the proposed antenna at 2.5GHz, 3.5GHz, and 4.5 GHz (φ=0° and φ=90°) are shown in Fig. 8, from which it can be obtained that the measured radiation patterns agree well with the simulation ones, and the antenna exhibits RHCP performance in the entire CP operating band. And the measured results show that the cross-polarization of the proposed antenna is less than −15.2 dB, and the front-to-back ratio is more than 19.8 dB.

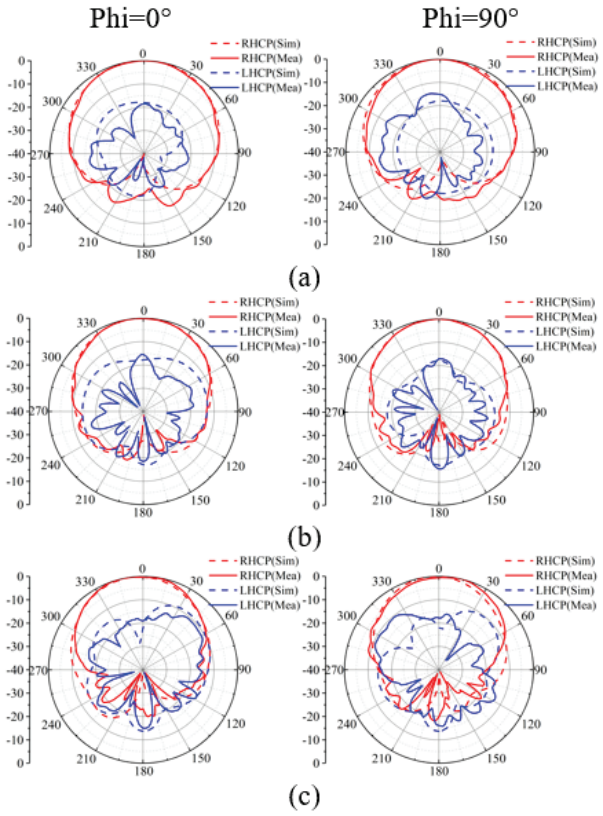

Fig. 8. Simulated and measured radiation patterns at (a) 2.5GHz, (b) 3.5GHz, and (c) 4.5 GHz.

Finally, the proposed antenna is compared with other broadband CP crossed dipole antennas in Table 1 (λ_0 is the center wavelength at the CP operating frequency in free space). Compared with antennas in [5, 7-9], the IBW and ARBW of the proposed antenna of are wider, and the gain values of the proposed antenna change slightly as seen from the minimum ΔG value of the proposed antenna. Although the IBW and ARBW of the antenna in [6] are wider than those of the proposed antenna, its overall size is larger and the variation of gain is very significant as seen from the maximum ΔG. Both the IBW and ARBW of the antenna [10] are wider than those of the proposed antenna. However, the dimension of the antenna in [10] is larger and the structure is further complicated by the addition of a circular structure between the antenna and the reflector plate, and the gain flatness is worse than that in the proposed paper. Compared with [11], the bandwidth of the proposed antenna is wider. In summary, the proposed antenna can obtain wide bandwidth and good gain flatness simultaneously.

IV. CONCLUSION

In this paper, a broadband CP crossed-dipole antenna with stable gain values is proposed. The measured results show that IBW is 80.8% (2.03GHz∼4.78GHz),

and ARBW is 68.5% (2.35GHz∼4.8GHz). By adding four improved parasitic plates, a flat gain curve of the proposed antenna is achieved in the whole frequency band, and the average gain is 7dBic. Due to the wide bandwidth and little fluctuant gain performances, the designed antenna is valuable in wireless communication systems such as indoor antennas in the frequency band of 2.4G WiFi, which requires excellent receiving characteristics. Moreover, the operation band of the proposed antenna covers parts of the 4G and 5G communication bands, which can make the designed antenna be also utilized in indoor base station communication.

ACKNOWLEDGMENT

This work is supported by the Natural Science Basic Research Program of Shaanxi (Program No. 2022JQ-699, 2022JQ-633, and 2021JQ-710) and the Key Research and Development Program of Shaanxi (Program No. 2021GY-049).

REFERENCES

[1] P. Sharma and K. Gupta, "Analysis and optimized design of single feed circularly polarized microstrip antennas," *IEEE Transactions on Antennas and Propagation*, vol. 31, no. 6, pp. 949-955, 1983.

[2] J. W. Baik, K. J. Lee, W. S. Yoon, T. H. Lee, and Y. S. Kim, "Circularly polarised printed crossed dipole antennas with broadband axial ratio," *Electronics Letters*, vol. 44, no. 13, pp. 785-786, 2008.

[3] J. W. Baik, T. H. Lee, S. Pyo, S. M. Han, J. Jeong, and Y. S. Kim, "Broadband Circularly Polarized Crossed Dipole With Parasitic Loop Resonators and Its Arrays," *IEEE Trans Antennas Propag*, vol. 59, no. 1, pp. 80-88, 2011.

[4] H. H. Tran and I. Park, "Wideband circularly polarized 2×2 antenna array with multibeam steerable capability," *IEEE Antennas and Wireless Propagation Letters*, vol. 16, pp. 345-348, 2017.

[5] L. Wang, W. X. Fang, Y. F. En, Y. Huang, W. H. Shao, and B. Yao, "Wideband circularly polarized cross-dipole antenna with parasitic elements," *IEEE Access*, vol. 7, pp. 35097-35102, 2019.

[6] Z. Zhao, Y. Li, L. Wang, Z. Tang, and Y. Yin, "Design of broadband circularly polarized antenna via loading coupled rotated dipoles," *Microwave and Optical Technology Letters*, vol. 61, pp. 425-430, 2018.

[7] W. J. Yang, Y. M. Pan, and S. Y. Zheng, "A low-profile wideband circularly polarized crossed-dipole antenna with wide axial-ratio and gain beamwidths," *IEEE Transactions on Antennas and Propagation*, vol. 66, no. 7, pp. 3346-3353, 2018.

[8] H. H. Tran, I. Park, and T. K. Nguyen, "Circularly polarized bandwidth-enhanced crossed dipole antenna with a simple single parasitic element," *IEEE Antennas and Wireless Propagation Letters*, vol. 16, pp. 1776-1779, 2017.

[9] H. Zhang, Y. Guo, and G. Wang, "A design of wideband circularly polarized antenna with stable phase center over the whole GNSS bands," *IEEE Antennas and Wireless Propagation Letters*, vol. 18, no. 12, pp. 2746-2750, 2019.

[10] Y. Feng, J. Li, B. Cao, J. Liu, G. Yang, and D. Wei, "Cavity-backed broadband circularly polarized cross-dipole antenna," *IEEE Antennas and Wireless Propagation Letters*, vol. 18, no. 12, pp. 2681-2685, 2019.

[11] M. Sefid, C. Ghobadi, and J. Nourinia, "Broadband circularly polarized crossed-dipole antenna and its array for long-term evolution communication systems," *International Journal of RF and Microwave Computer-Aided Engineering*, vol. 31, no. 12, e22896, 2021.

[12] Y. Chen, S. Wang, S. Shi, M. Jiang, J. Ding, J. Gao, and G. Zhai, "Landstorfer Printed Log-Periodic Dipole Array Antenna With Enhanced Stable High Gain for 5G Communication," *IEEE Transactions on Antennas and Propagation*, vol. 69, no. 12, pp. 8407-8414, 2021.

[13] Z. Wu, X. Li, and X. Song, "An improved ultra-wideband circularly polarized cross-dipole antenna," *13th International Symposium on Antennas, Propagation and EM Theory (ISAPE)*, pp. 1-3, 2021.

Xueyan Song was born in Henan Province, China, in 1989. She received her B.E. degree in electronic and information engineering from Xidian University, Xi'an, China, in 2012. She received a Ph.D. degree in Electromagnetic Fields and Microwave Technology from Xidian University, Xi'an, China, in 2018.

She joined the School of Electronic Engineering, Xi'an University of Posts and Telecommunications in 2018. Her research interests include artificial magnetic conductors, low RCS antennas, low-profile antennas, frequency-selective surfaces, and reflector antennas.

Zhiyuan Wu was born in Hubei Province, China, in 1995. He is currently pursuing a Master of Engineering degree in the School of Electronic Engineering, Xi'an University of Posts and Telecommunications. His current research interests include circularly polarized antennas, metamaterials, and array antennas.

Xuping Li was born in Xi'an, Shanxi, China in 1981. He received a Ph.D. degree in electromagnetic fields and microwave technology from Xidian University, Xi'an, China, in 2015. His research interests are antenna theory and engineering.

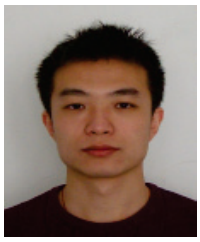

Yunqi Zhang was born in BaoTou, Inner Mongolia, China. He received a Ph.D. degree from Xidian University, Xi'an, China in 2015. He is currently working at the Xi'an University of Posts & Telecommunications. In 2017 he joined the School of Physics and Optoelectronic Engineering at Xidian University, as a postdoctoral candidate. His research interests include GPS antenna, CP antenna, omnidirectional antenna, and antenna array designs.

Hailong Yang received a B.S. in Communication Engineering from Heze University, Heze, China, in 2012. He earned M.S. and Ph.D. degrees in Communication Engineering from Xi'an University of Technology, Xi'an, China, in 2015 and 2019, respectively. He joined the faculty of the Electronic Engineering Department, Xi'an University of Posts and Telecommunications, in 2019. His research interests include wave propagation and antenna design.